Molecular Simulation of Diffusive Mass Transport in Porous Materials

Hendrik Frentrup

A thesis submitted in partial fulfilment
for the degree of
Doctor of Philosophy of Imperial College London

Department of Chemical Engineering
Imperial College London
United Kingdom

12th December 2014

Declaration of Originality

I, Hendrik Frentrup, hereby declare that the work in this thesis is my own and that work from others has been referenced appropriately.

Copyright Information

Acknowledgments

On 21 December 2009, I sent an email to "e.muller@imperial.ac.uk" hoping to hear back in January about the possibility to embark on a research project in London. I received my answer on 23 December 2009 and merely a month later, my application to Imperial College had been sent in and I had been assigned the six digits that identify me as a member of this institution until today. For the amazing journey that followed, I sincerely thank my supervisor Erich Müller. I am only beginning to understand the significance of his support and what the doors he opened for me mean for what is to come.

More important than opening doors, I am truly grateful for making me cross paths with many great individuals. I am no exception to be very lucky for having worked with and learned a great amount from Carlos Avendaño. I recall that a whole generation of students at Imperial know what a great mentor and friend Carlos is. Out of pure irony, we've named a demon after him (see Section 6.1). My most heartfelt thanks also go to Kyle Hart. A lucky coincidence made us bump into each other in Belfast at the very beginning and this turned into a wonderful collaboration.

I've been lucky to draw on the kind support and advice of Coray Colina, Amparo Galindo, Claire Adjiman and George Jackson. For their camaraderie and kindness, I would like to thank the members of the Department of Chemical Engineering and, in particular, the Molecular Systems Engineering group: Jeong Kim, Carmelo Herdes, Roochi Solanki, Nina Ramrattan, Olga Lobanova, Martin Horsch, Lara Yaroson, Carlos Braga and many others that I failed to mention here. Likewise, I'd like to thank my good friends at Imperial and in London, Kees, Steffen, and Julian.

Most importantly, I am enormously thankful to my families, to my parents, to my brothers and sister, and to Izabela.

Abstract

Ever increasing control over the shape and form of a material's nanoscale features provokes the pursuit of a detailed understanding for the main factors influencing fluid transport. It is sought to facilitate the intelligent design of novel materials used in membrane separation processes. In addition to a strong dependence on molecular mobility, mass transport is heavily influenced by thermodynamic effects. Isolating thermodynamic and mobility effects is useful to understand the significant driving forces for mass transport through porous materials and their selective characteristics. However, experimental techniques are limited in probing this behaviour at the nanometre scale. In response to experimental challenges, the present study makes extensive use of the ability of molecular simulations to reflect the molecular character of nanoscale diffusion and identify equilibrium and transport properties individually.

First, this work investigates diffusive mass transport inside a planar slit pore focusing on the influence of solid-fluid interactions, pore width, and fluid density. The influence of solid-fluid interactions, in particular, have often been neglected in studies of mass transport in porous solids. The vast variety of functionalised nano-materials is virtually endless and has spurred interest in this area. Equilibrium simulations were employed to determine self- and collective diffusivities and Grand Canonical insertions were used for the determination of thermodynamic factors. In addition, this work showcases the implementation of a highly efficient Non-Equilibrium Molecular Dynamics (NEMD) method through which effective transport was studied. The method was used to determine effective diffusivities which incorporate thermodynamic effects, the dominating contribution to transport for dense fluids. It is well suited to observe effective fluid transport in confined spaces as opposed to measuring self-diffusion, a measure for single-particle mobility only.

The method is effective in studying mass transport in model systems as well as more realistic, complex geometries. As a second exemplary case, gas permeation through an atomistically detailed model of a high free-volume polymer was simulated explicitly with the NEMD approach. In addition to determining permeability and solubility directly from NEMD simulations, the results also shed light on the permeation mechanism of the penetrant gases, suggesting a departure from the expected pore-hopping mechanism due to the considerable accessibility of permeation paths.

CONTENTS

1 Introduction **10**

2 Diffusion, in theory and experiment **13**

2.1 Diffusion experiments 13

2.2 Mass transfer in theory 15

2.2.1 Transfer models for bulk fluids 17

2.2.2 Transfer models for fluids in porous solids 19

2.3 Single-component mass transfer of a confined fluid 25

3 The Molecular Simulation "Toolbox" **28**

3.1 The thermodynamic roots of Molecular Simulations 29

3.1.1 Molecular interactions 31

3.1.2 Stochastic and deterministic simulation methods 37

3.2 Transport properties from Molecular Simulations 41

3.2.1 Self-diffusivity 42

3.2.2 Collective diffusivity 44

3.2.3 Non-equilibrium Molecular Dynamics 45

3.3 Boundary-driven non-equilibrium MD 48

4 Modelling of diffusive mass transport in planar slit pores **58**

4.1 Introduction 58

4.1.1 Model potentials for a planar slit pore systems 64

4.1.2 System setup of this work 67

4.2 Adsorption Isotherms 67

4.2.1 Grand Canonical insertions 68

4.2.2 Thermodynamic factor 69

4.3 Diffusion and particle mobility 75
4.3.1 Self-diffusion 75
4.3.2 Collective diffusion 79
4.3.3 Transport diffusion from NEMD 84
4.4 Comparison of transport models 86
4.5 Conclusions 91

5 Modelling of gas permeation through PIM-1 **94**
5.1 Introduction 94
5.1.1 Molecular modelling 97
5.1.2 Model characterisation 99
5.1.3 NEMD simulations 100
5.2 Results and Discussion 103
5.3 Conclusions 108

6 Concluding remarks and outlook **110**
6.1 Avendaño's demon and the self-diffusion coefficient 111
6.2 Rejection Modelling 115

Bibliography **118**

A Appendix **137**
A.1 Translation of epigraphs 137
A.2 Additional data on the slit pore system 139

LIST OF FIGURES

2.1 Schematic of the time lag permeation technique 16
2.2 Qualitative classification of mass transfer models 17
2.3 Drawing of the Hagen-Poiseuille and slip flow model 22

3.1 Various mean square displacement curves of the bulk LJ fluid 43
3.2 Velocity Correlation functions 46
3.3 Diagram of the model slit pore 49
3.4 Density profiles along the pore length 53
3.5 Influence of external field 53
3.6 Velocity profiles along the pore length 54
3.7 Temperature profiles 55
3.8 Effective diffusivities for the narrow and wide pore. 56

4.1 Literature data for the slit pore model 61
4.2 Literature data for a cylindrical zeolite pore 62
4.3 Interaction potential of slit pores 66
4.4 Pressure-density-chemical potential relationships 70
4.5 Thermodynamic factor of the bulk fluid 71
4.6 Adsorption isotherm of the narrow pore 73
4.7 Adsorption isotherm of the wide pore 73
4.8 Density distribution profiles 74
4.9 Thermodynamic factor of the narrow pore 75
4.10 Thermodynamic factor of the wide pore 76
4.11 Self-diffusion coefficient of the bulk 78
4.12 Self-diffusion coefficients for the narrow pore 80
4.13 Self-diffusion coefficients for the wide pore 81

4.14 Collective diffusion coefficients for the narrow pore 83
4.15 Collective diffusion coefficients for the wide pore 84
4.16 Effective diffusion coefficients for the narrow pore 85
4.17 Effective diffusion coefficients for the wide pore 86
4.18 Velocity profiles 89
4.19 Comparison of transport coefficients for the narrow pore 92
4.20 Comparison of transport coefficients for the wide pore 93

5.1 Visualisation of the thin-slice PIM-1 sample 97
5.2 Pore size distribution of 2D thin-slice compared to 3D periodic sample . 100
5.3 Simulation snapshot and density and velocity profiles 102
5.4 Permeation and solubility results in comparison to experiments 104
5.5 Visualisation of gas permeation paths 106
5.6 Density maps inside the polymer 107

6.1 Avendaño's demon density profiles 112
6.2 Schematic drawing of the rejection curve of a common membrane 115
6.3 Schematic of the pore, solute and solvent geometries 116
6.4 Results for rejection for steady state simulations 117
6.5 Schematic drawing of the influence of pore length on hydrodynamics . . 119

A.1 Pressure isotherm of the bulk 139
A.2 Chemical potential isotherm of the bulk (density dependent) 140
A.3 Chemical potential isotherm of the bulk (pressure dependent) 140
A.4 Thermodynamic factor of the narrow pore 141
A.5 Thermodynamic factor of the wide pore 142
A.6 Self-diffusion in the narrow pore 146
A.7 Collective diffusion in the narrow pore 146
A.8 Self-diffusion in the wide pore 147
A.9 Collective diffusion in the wide pore 147
A.10 Effective diffusion coefficients for the narrow pore 149
A.11 Effective diffusion coefficients for the wide pore 149

LIST OF TABLES

3.1 Setup of system to validate the boundary-driven NEMD approach . . . 51

4.1 This table shows the fitted parameters of the modified Tóth equation (Eq. (4.6)) for the six isotherms that were determined from GCMD simulations. 72
4.2 This table shows the fitted parameters of the self-diffusion correlation of the bulk LJ fluid. 78
4.3 Coefficients of the viscosity correlation for the LJ fluid (Galliéro et al., 2005). 89

5.1 Porosity of the PIM-1 simulated samples 98

6.1 Avendaño's demon results for the small realisations of the narrow and wide pore. The number in the parentheses denotes the uncertainty in the last digit. 114

A.1 Simulation results of EMD simulations for the narrow pore. 144
A.2 Simulation results of EMD simulations for the wide pore. 145
A.3 Simulation results of boundary-driven NEMD simulations for the narrow pore. 150
A.4 Simulation results of boundary-driven NEMD simulations for the wide pore. 151
A.5 Simulation results of boundary-driven NEMD simulations for the wide pore (continued). 152

CHAPTER

ONE

INTRODUCTION

A significant number of chemical engineering processes are targeted at the separation of different species in a mixture. The understanding and predictability of vapour-liquid equilibria has provided a reliable route to large-scale separation processes via selective distillation of gases and liquids. However, the energy expense of performing a separation through a phase change is considerable. It has been a long-standing goal to reduce the energy expense of industrial separations by forcing the components of a mixture through a porous material that exhibits selectivity towards some of the constituents. A prominent example of topical interest is the desalination of sea water, for which reverse osmosis membrane materials have been developed since the late 1960s (Sourirajan and Agrawal, 1969). Desalination requires a high level of selectivity towards the solved ions, which are only slightly bigger than the water molecules in which they are solvated. Permeabilities are fairly low and large pressure differences are required to both overcome the osmotic pressure of sea water and drive the desalination process. Over the last decade, the remarkable mass transport properties of carbon nanotubes (CNTs) have been noted in molecular simulation studies (Hummer et al., 2001). These findings inspired the use of CNTs in selective layer materials for separation purposes. Studies have shown that CNT-enhanced membrane materials allow higher fluxes than state-of-the-art materials (Holt et al., 2006; Karan et al., 2012). It is said that the narrow and smooth confinement of CNTs forces water molecules to line up in a single file, while the smooth walls exert minimal momentum transfer from the fluid to the pore walls. In more general terms, water confined in a non-polar environment builds tightly hydrogen-bonded wires or clusters (Rasaiah et al., 2008). This peculiar behaviour was impressively demonstrated in a recent study, in which a mem-

brane proved to be impermeable to helium while allowing a seemingly unhindered pervaporation of water (Nair et al., 2012). The active layer of the membrane was composed of stacks of graphene oxide (GO) sheets, spaced less than a nanometre apart, which allowed water to form a mono-layer between the GO sheets.

The search for a material that can provide high selectivity and permeability is still the "holy grail" in this area. Desalination, however, is just one example of an industrial separation process for which selective nanoscale materials are expected to provide disruptive potential. In the area of purifying active pharmaceutical ingredients, the filtration of solvents as well as the separation of gases, microporous materials with specifically tailored properties are sought to deliver more efficient separation processes.

The general search for discovery and design principles of promising advanced selective materials is fuelled by an ever increasing control over engineered nanoscale materials for specific purposes. Hybrid membranes made of ceramics or polymers and encapsulating nanosized particles, such as metal-organic frameworks (MOFs), are a new frontier in membrane science. MOFs, in particular, exhibit extremely large surface areas per unit volume. Their adsorption and mass transport properties are an active area of research (Keskin and Sholl, 2009; Getman et al., 2012). From an engineering point of view, it is important to understand the underlying mechanisms of mass transport in these novel nanoscale structures in order to have methods at hand for predicting their transport properties in technical applications. In parallel to structured molecular materials such as zeolites, mesoporous silicas, and MOFs, the development of microporous amorphous polymers and nanostructured carbons have garnered increased interest as a suitable material for efficient gas separations, which is not only highly selective for certain gas mixtures but also seen to ensure ease of fabrication on a large scale (Bernardo et al., 2009; Aroon et al., 2010; Li et al., 2009).

Given the dominant nanoscale character of these materials, the applicability of existing mass transport theories, which originally apply to systems that need not be treated in molecular resolution, can be investigated with molecular simulations. It is the purpose of this work to apply molecular simulations to investigate mass transfer phenomena in porous materials that exhibit confining pores as small as a few nanometers. Therefore, the pores are merely a few times larger than the fluid molecules flowing through them.

To this end, the first chapter of this thesis will review established theories dealing with diffusion in bulk fluids and mass transfer in porous materials. Subsequently, the specific molecular modelling and simulation methods used in this work are presen-

ted, with a detailed discussion of a non-equilibrium Molecular Dynamics approach employed throughout this work. Chapter 4 presents the application of molecular simulations to study mass transport in a familiar model system, namely the planar slit pore, and highlights the effects of fluid density and solid-fluid interactions on the predictions of mass transport in porous materials. Chapter 5 shows a practical application of the non-equilibrium simulation method by presenting the simulation of gas permeation through a microporous polymer. It also highlights the possible insights into the dynamics of mass transport that can be obtained from molecular simulations. Finally, apart from a short review of the investigation's findings, the concluding chapter will present further areas in which non-equilibrium techniques can be applied to obtain dynamic properties of molecular systems.

CHAPTER

TWO

DIFFUSION, IN THEORY AND EXPERIMENT

Vielleicht ist der Grund dieser spärlichen Bearbeitung zum Theil in der grossen Schwierigkeit zu suchen auf diesem Felde genaue quantitative Versuche anzustellen. Und in der That ist diese so gross, dass es mir trotz andauernder Bemühungen noch nicht hat gelingen wollen, den Streit der Theorien zu einem definitiven Abschluss zu bringen.

Adolf Fick,
Über Diffusion in Annalen der Physik (1855)

2.1 Diffusion experiments

The prevalence and significance of diffusion processes in nature and science was acknowledged early through the observation of osmotic processes in the mid 18th century (Nollet, 1748, 1995) and the discovery of Brownian motion observed in the early 19th century (Brown, 1828). The exact quantitative determination of diffusion coefficients is far more difficult than the qualitative observation of diffusion processes, however. An informed assessment of rates of diffusion is a modern achievement and routine measurements are rare to this date. The first quantitative observations of diffusion phenomena were limited to gaseous diffusion (Graham, 1829) and diffusion in dilute solutions (Fick, 1855a). The observations of Graham and Fick revealed that gas diffusion and liquid diffusion occur on different times scales as gas diffusion often happens a thousand times faster than liquid diffusion. The equipment thus required to measure differences in concentration, pressure and molar flux depends on whether

transport occurs in liquid or gaseous states and needs to be chosen specifically for a particular system of interest. The time-dependent, multi-component character of diffusion processes adds to the experimental complexity, but also allows for a wide range in experimental approaches to be applied for the quantitative measurement of diffusion coefficients. These span from straightforward techniques, where concentration differences in stirred bulk liquids are determined after diffusion through a highly porous cell occurred for a specific amount of time (Cussler, 2009), to very elaborate nuclear magnetic resonance experiments, in which no actual concentration differences are required to determine diffusion coefficients. Instead, the decay of a pulse is observed (Kärger et al., 2012).

While experimental analysis of bulk liquid diffusion coefficients is highly complex and involves sophisticated experiments, such as Taylor dispersion, dynamic light scattering, or interferometry (Cussler, 2009), experiments of mass transfer in porous materials present a particular challenge as confinement in pores can influence the fluid transport significantly. For practical purposes, the determination of gas diffusion through porous polymers is performed in connection with permeation experiments, which are of central importance in the characterisation of gas separation materials. The diffusion coefficient of gases in a solid membrane can be determined from the time-lag of steady-state gas flux through a membrane of specific thickness located between a feed volume and an evacuated volume (Rutherford and Do, 1997) (see Fig. 2.1). The same approach is often employed to determine gas solubility from a single permeation and diffusion experiment. More details on penetrant gas diffusion in porous polymers are covered in Chapter 5.

Porous materials often exhibit pores that are in the nanometre range and hence the confining length scales of the pore are strikingly different to those commonly found in macroscopic studies of diffusion processes. Nevertheless, it is here that the modern challenges in the field lie, to be able to image and characterise flow and fluid displacement with nanometre precision. The most advanced diffusion experiments observe diffusion processes with a molecular resolution. Among these experimental approaches on the nanoscale are pulse-field gradient nuclear magnetic resonance (PFG-NMR) (Kärger et al., 2012) and quasi-elastic neutron scattering (QENS). The former uses the alignment of the magnetic moments of the atomic nuclei to monitor the mean square displacement of molecules. The latter is based on changes in frequency and wave vector of a neutron beam directed onto the experimental sample. The exchange of energy between the incident neutron beam and the scattering centres leads to a

Doppler shift of the scattered beam. Although both PFG-NMR and QENS require very extensive laboratory infrastructure for experiments to be carried out, an increasing number of investigations in this field is recently being undertaken. For example, to study the diffusion of adsorbates in microporous zeolites and carbonaceous membranes (Snurr and Kärger, 1997; Mueller et al., 2012) or the surface diffusion of water on nanoparticles (Chu et al., 2011). In addition, electron microscopy, atomic force microscopy and X-Ray diffraction techniques are commonly employed to characterise the porous materials under scrutiny. The considerable cost of acquisition and operation as well as the level of expertise required to undertake these experiments pose a limitation on how extensively fluid transport properties in nanoporous materials can be investigated. Understandably, molecular simulations provide an alternative and accessible route towards studying mass transfer on the nanoscale. Molecular simulation studies are often performed alongside experiments in order to support and improve the analysis and interpretation of experimental data and complement the applicability of theoretical frameworks. It has been pointed out that PFG-NMR and QENS observe the mean square displacement of a diffusing species, analogous to most molecular simulation studies, and thus measure self-diffusion, also often referred to as *tracer* diffusion, rather than transport diffusion (Cussler, 2009). In this regard, molecular simulations have played an important role in shedding light onto the differences between diffusion coefficients determined from experiment (Maginn and Elliott, 2010). Self-diffusivities, transport diffusivities, and corrected diffusivities can all have different dependencies on concentration, temperature, and system parameters (Sholl, 2006). A clear definition and an exact calculation of these properties from molecular simulations has helped to clarify much of the controversy among experimentalists.

2.2 Mass transfer in theory

A detailed mathematical model for diffusive mass transfer was pioneered by Adolf Fick in the mid 19th century by studying the mass fluxes in dilute mixtures (Fick, 1855b,a). The seminal publication was recently reprinted (Fick, 1995) in the Jounal of Membrane Science due to its long-lasting impact and relevance. Fick established an analogy of diffusion, a process driven by "molecular forces" (Fick, 1855b), to the conductance of heat or the spreading of electricity in a material and therefore the constitutive relations he established resemble Fourier's law for heat conductance and Ohm's law for electrical currents. The mathematical form of his descriptions of dif-

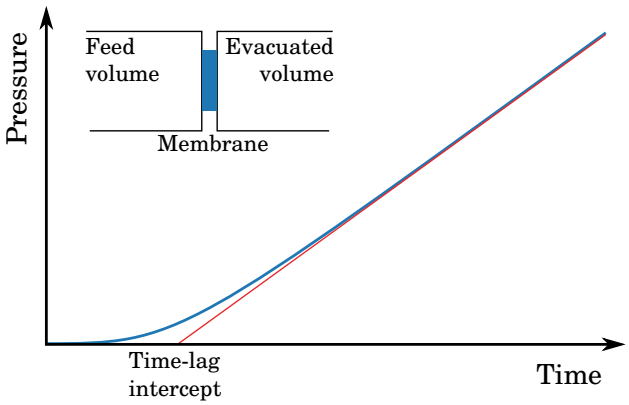

Figure 2.1: Schematic of the time lag permeation technique described in (Rutherford and Do, 1997), which is commonly used to characterise gas separation membranes.

fusion in bulk are under certain assumptions still regarded as accurate today and find wide-spread use. Nonetheless, the theoretical treatment of mass transfer evolved from Fick's phenomenological descriptions of macroscopic observations, which generally regards the systems of interest as a continuum, to an approach that explicitly incorporates the molecular nature of materials. By the end of the 19th century, the triumph of the molecular hypothesis and kinetic theory (Maxwell, 1867; Smoluchowski, 1906) and the significant breakthroughs in thermodynamics (Gibbs, 1875; Einstein, 1905) rendered a molecular theory for diffusion possible and helped clarify much of the discrepancies of Fick's laws. Shortly afterwards, the behaviour of fluids confined in porous structures garnered considerable interest and Martin Knudsen pioneered the prediction of mass transfer for low density gases in narrow tubes based on molecular collision arguments (Knudsen, 1909).

From a modern perspective, it is remarkable how relevant these elaborate and sophisticated theoretical models are to this date, despite the bold assumptions their originators had to make. Most of them are still very useful and find applicability in terms of a qualitative, and to a large extent quantitative, treatment of diffusion phenomena today. The limits of mass transfer models prevailing today are in fact very similar to those that limited the field's pioneers. Among them is the mathematical difficulty in describing collision dynamics of complex and dense fluids, strong solid-fluid interactions and a transferable treatment for complex agents of separation (e.g. tubes with a very smooth surfaces in contrast to membranes of intrinsic porosity). A general overview of different mass transfer theories and their classification among the level of confinement as well as the molecular detail of these theories is given in Figure 2.2.

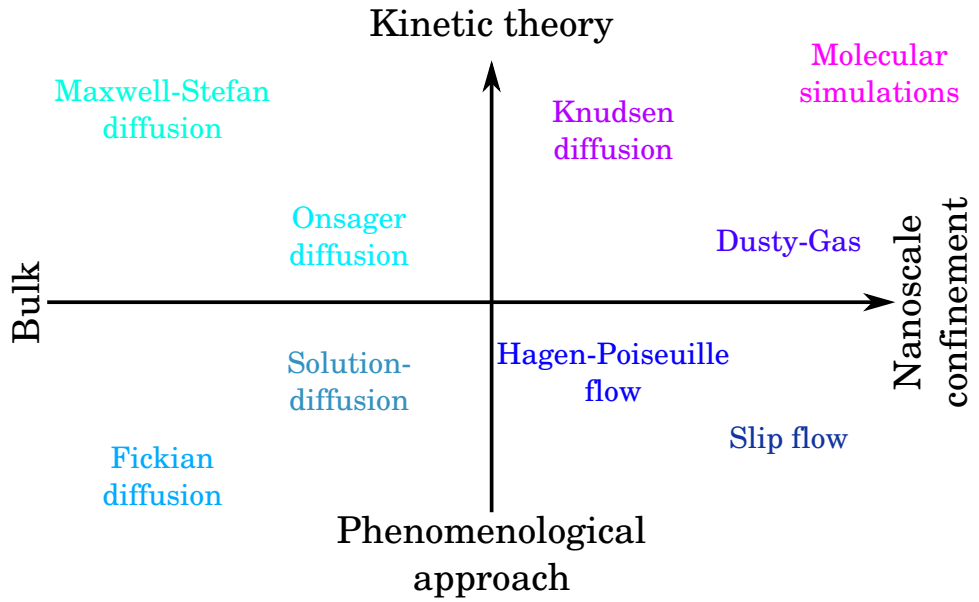

Figure 2.2: A broad, qualitative classification of mass transfer models in terms of the theoretical detail focusing on molecular and confinement effects. From Fick's description, a purely phenomenological approach for bulk mass transfer, to the Knudsen approach and molecular simulations which account for a high degree of molecular detail in fluid medium and confining solid. The following section gives insight into the different theories presented here.

In the following, the most prevailing mass transfer models, in particular those mentioned in Figure 2.2, including their limitations to treat nanoscale phenomena, will be reviewed.

2.2.1 Transfer models for bulk fluids

Bulk diffusion is most commonly described by *Fickian diffusion*, often called transport diffusion, which describes a net mass flux, $\mathbf{J}$, driven by a gradient in concentration. The magnitude of the diffusive flux is related to the gradient by a phenomenological transport coefficient, the Fickian diffusion coefficient. In the presence of concentration gradients in a two component system, the diffusive flux in the continuous system is commonly described by Fick's first law (Bird et al., 2002):

$$\mathbf{J}_i^{\mathrm{D}} = -D_{\mathrm{t}}(\rho)\boldsymbol{\nabla}\rho_i \ , \tag{2.1}$$

where $\rho_i(\mathbf{r}, t)$ is the local density of species i and D_{t} is the coefficient of transport diffusion (also called Fickian diffusivity). While the concept was conceived for two mobile

species, it is important to note that mass transport in porous media deals with the porous material being stationary and a net flux occurs only for the fluid. Therefore, when dealing with a pure fluid in confinement, the transport equations simplify significantly. Due to its simple formulation, the Fickian approach finds wide-spread use in engineering and is appropriate for many applications, such as diffusion in dilute solutions. However, the approach breaks down for non-ideal scenarios. For instance, at the interface of two separate phases in equilibrium, a considerable gradient in concentration will not induce a net flux. In response, the notion of a gradient in chemical potential being the fundamental driving force of mass transport was conceived:

$$\mathbf{J}_i^{\mathrm{D}} = -\sum_j^m L_{ij}(\rho)\boldsymbol{\nabla}\mu_j \ , \tag{2.2}$$

where μ_j denotes the chemical potential of species j in a system made up of m different species. L_{ij} are called the phenomenological linear transport coefficients, or *Onsager diffusion* coefficients (de Groot and Mazur, 1962). The Onsager approach showcases that diffusion processes are traditionally dealing with multi-component mixtures.

The *Maxwell-Stefan diffusion* model similarly considers the chemical potential gradient as the driving force behind diffusion (Taylor and Krishna, 1993). It is derived from arguments based on the kinetic theory of gases and thus incorporates a more detailed molecular character in describing diffusion phenomena. For bulk diffusion in a two component system, the Maxwell-Stefan description of diffusive mass transport can be expressed as:

$$x_2(\mathbf{u}_1 - \mathbf{u}_2) = -\frac{D_{12}^{\mathrm{MS}}}{k_{\mathrm{B}}T}\boldsymbol{\nabla}\mu_1 \ , \tag{2.3}$$

where D_{12}^{MS} denotes the Maxwell-Stefan diffusivity, T is the temperature, k_{B} is Boltzmann's constant, and $\mathbf{u}_i$ (i=1,2) are the average molecular velocities of the two species. The resistance to mix is influenced by the composition of the mixture and a frictional drag, expressed by the drag coefficient $k_{\mathrm{B}}T/D_{12}^{\mathrm{MS}}$. The connection between mass transfer according to Fick, Onsager, and Maxwell-Stefan has been formerly established based on arguments derived from kinetic theory (Chapman and Cowling, 1939) and on irreversible thermodynamics (Hirschfelder et al., 1954).

Under the assumption that component 1 is the confined fluid and component 2 is the porous medium behaving as a bulk component in a homogeneous mixture, the definition of x_2 and $\mathbf{u}_2$ is difficult due to the porous material being stationary. In the limiting case of low pressure gas diffusion, x_2 tends to zero and $\mathbf{u}_2 = 0$. Geometrical

factors such as tortuosity and porosity or any potential influence of composition is then accounted for in the drag coefficient $D_{1,\mathrm{p}}^{\mathrm{MS}}$:

$$\mathbf{u}_1 = -\frac{D_{1,\mathrm{p}}^{\mathrm{MS}}}{k_{\mathrm{B}}T}\boldsymbol{\nabla}\mu_1 \ , \tag{2.4}$$

Therefore, extending to an expression of one-dimensional mass transport, the expression is similar to eq. (2.1) and eq. (2.2):

$$\mathbf{J}_1 = \rho\mathbf{u}_1 = -\frac{\rho}{k_{\mathrm{B}}T}\, D_{1,\mathrm{p}}^{\mathrm{MS}}\boldsymbol{\nabla}\mu_1 \ . \tag{2.5}$$

A notable difference to the Fickian and Onsager expressions is that the flux described in eq. (2.5) is the total mass flux and not only a diffusive component. This subtlety is important as it is common to distinguish between diffusive and convective flow and treat the two components separately:

$$\mathbf{J} = \mathbf{J}^{\mathrm{D}} + \mathbf{J}^{\mathrm{C}} \ . \tag{2.6}$$

The distinction is often comprehensive since convective flux, $\mathbf{J}^{\mathrm{C}}$, stems from inertial effects on the macroscopic level while diffusive flux, $\mathbf{J}^{\mathrm{D}}$, arises from the molecular scale and occurs due to the random thermal motion of molecules. Notwithstanding, the distinction depends on the chosen frame of reference (Keffer et al., 2005).

As a further complication, in contrast to the above mentioned transport diffusion coefficients, self-diffusivities are measured at equilibrium and relate to transport diffusion only in the limiting case of infinite dilution. In essence, self-diffusion is the diffusion of a single particle surrounded only by equivalent particles, such as the diffusion of a specific isotope in otherwise identical molecules. This isotope is often referred to as the tracer, thus the term “tracer diffusion”.

2.2.2 Transfer models for fluids in porous solids

A straightforward model of mass transfer through porous materials is based on *continuum hydrodynamic flow* in a solid of well-defined and simple geometry. It is mathematically based on the Navier-Stokes equations, which in turn are derived from the momentum balances based on the principle of conservation of momentum. A Newtonian fluid exchanges momentum on the macroscale via convective processes. Internal friction as a result of microscopic momentum transport is accounted for by the viscosity of the fluid. In the simplest case, a pressure difference drives the flow through pores of a stationary material, e.g. a tubular capillary. Transport only happens in the

open pores and therefore only the open voids in a porous material contribute to transport. In classical fluid dynamics, it is common to assume no slip between the fluid and the solid wall at the interface. Following these assumptions, the magnitude of fluid flow in a tube is described by the *Hagen-Poiseuille* equation for a cylindrical pore as follows:

$$J_x = -\frac{d^2}{32\eta}\frac{\mathrm{d}P}{\mathrm{d}x} \ , \tag{2.7}$$

where P denotes the pressure, d denotes the width of the cylindrical pore and η is the dynamic viscosity of the fluid. This approach to pressure-driven mass transport is equivalent to one of the earliest mass transfer models, Darcy's law. It is a phenomenological observation that the permeating flux through a porous solid is proportional to the pressure difference across the porous material:

$$J_x = \kappa_\mathrm{P}\frac{\Delta P}{\Delta x} \ . \tag{2.8}$$

The permeability κ_P is the constitutive relation between pressure drop and flux. It is assumed that the pressure drop across the porous material is linear.

Based on this perception that fluid flow is confined to open voids in the material, the *Pore-Flow* model (Silva et al., 2005) was conceived to predict permeabilities and selectivities of porous membranes. It is often assumed that the confined fluid has the same viscosity as the bulk fluid. For fluids confined in very narrow pores however, neither the density nor the viscosity of the fluid are uniform within the pore and can differ from the bulk properties by a considerable amount. Transport models for membrane separations were extended to account for an increased viscosity of the first layer of fluid molecules in contact with the solid (Bowen and Welfoot, 2002) by heuristically adjusting the viscosity of the fluid.

In contrast to the Pore-Flow model, the *solution-diffusion* model is very common among membrane scientists, especially in the field of gas separation (Wijmans and Baker, 1995). Here, the membrane is not viewed as a medium exhibiting defined pores through which fluid flow occurs, it is rather a continuum microporous material through which the permeating species diffuse. The permeation process is therefore a series of adsorption, diffusion and desorption processes that occur in series. The permeability κ_P, which is often also represented by P (in conflict with the denomination for pressure in this work), is therefore:

$$\kappa_\mathrm{P} = D \times S \ , \tag{2.9}$$

where D denotes the diffusion coefficient of a specific substance inside the membrane material and S denotes the solubility of that same substance. The solution-diffusion model is a very simple, yet powerful model to characterise gas transport. It rests on the assumption that non-idealities are not significant at the point of interest.

Likewise, the no-slip condition, on which the Hagen-Poiseuille model is based, has been subject of much debate. While it certainly is a valid assumption for most macroscopic liquid systems, evidence for a departure from the no-slip condition under certain conditions has surfaced (Thompson and Troian, 1997). Based on molecular simulations and experiments with structures that exhibit extremely smooth molecular surfaces (Groombridge et al., 2011; Kunert and Harting, 2007), such as carbon nanotubes (Hummer et al., 2001), very high fluxes have been attributed to considerable slip lengths (Majumder et al., 2005). Thus, the concept of slip length can be exploited to incorporate molecular particularities. Mathematically, the introduction of a slip length into the Hagen-Poiseuille equation allows an increased flow through the porous structure at otherwise identical boundary conditions. A schematic drawing of the Hagen-Poiseuille and slip flow scenarios can be seen in Fig. 2.3. The slip length is defined as the ratio of the axial velocity to the shear rate,

$$L_\mathrm{s} = \frac{u_\mathrm{wall}}{\mathrm{d}u/\mathrm{d}r} \,, \tag{2.10}$$

where u_wall denotes the axial velocity at the wall and $\mathrm{d}u/\mathrm{d}r$ the radial velocity gradient at the wall (Holt et al., 2006). As a result, the expression for the fluid flow is

$$J_x = \frac{(d^2 + 8dL_\mathrm{s})}{32\eta}\frac{\mathrm{d}P}{\mathrm{d}x} \,. \tag{2.11}$$

For low density gases, a different mass transfer model has enjoyed general acceptance in many applications. Similar to the Hagen-Poiseuille model, the *Knudsen diffusion* model deals with a fluid permeating through narrow cylindrical channels. This approach, however, focuses on gases in the low density limit where the mean free path of gas molecules is notably larger than the tubular confinement and therefore wall collisions, rather than interparticle collisions, dominate mass transport. In honour of the ground-breaking work of Martin Knudsen, gaseous flow in porous materials is classified by the dimensionless number named in his honour, which is defined as:

$$\mathrm{Kn} = \frac{\lambda}{L} \,, \tag{2.12}$$

with λ being the mean free path of the particles of the fluid and L being the character-

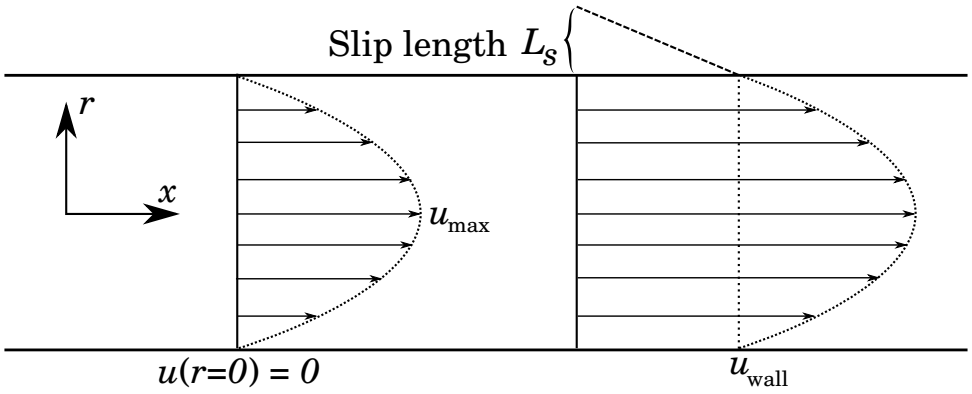

Figure 2.3: A schematic drawing of the Hagen-Poiseuille and Slip flow model.

istic length of the system, e.g. the diameter of a cylindrical pore. When the Knudsen number is smaller than 1, the gas diffusion in a cylindrical pore can be predicted with reasonable accuracy by the Knudsen equation (Arya et al., 2003):

$$D_{\mathrm{K}} = \frac{d}{3}\sqrt{\frac{8k_{\mathrm{B}}T}{\pi m}}\ , \tag{2.13}$$

where m is the molecular mass, T is the temperature and k_{B} denotes Boltzmann's constant. The pressure-driven gas flux through a narrow tube is therefore:

$$J_x = -\frac{D_{\mathrm{K}}}{k_{\mathrm{B}}T}\frac{\mathrm{d}P}{\mathrm{d}x}\ . \tag{2.14}$$

The underlying assumption of the Knudsen model is based on the gas molecules being reflected diffusively after colliding with the confining wall of the pore. Again, for very smooth molecular surfaces, collisions are increasingly specular, which makes this assumption break down. The diffusivity of the gas is in fact higher than predicted by eq. (2.13). Moreover, adsorption to the pore surface leads to discrepancies in the Knudsen approach. Henry's law constants are used as a measure for adsorption strength (Bhatia et al., 2011). Both pore width, molecular interactions and temperature have an influence of how much Knudsen diffusion would be affected by fluid adsorption to pore walls. In the case of strong adsorption, surface diffusion in addition to Knudsen diffusion must be accounted for. With increasing complexity of surface topology, of solid-fluid as well as of fluid-fluid interactions, a rigorous treatment becomes increasingly intractable.

The *Dusty-Gas* model is an extension of the Maxwell-Stefan diffusion approach and likewise strongly based on kinetic theory arguments (Krishna and Wesselingh, 1997).

The porous material is regarded as an ensemble of inert particles (Dusty Gas) randomly distributed in space through which the mobile species diffuse. The expression for isothermal diffusion of an ideal gas mixture is given by (Bhatia et al., 2011):

$$\sum_{j=1,i\neq j}^{n} \frac{x_j J_i - x_i J_j}{\rho_\mathrm{t} D_{ij}^\mathrm{e}} + \frac{J_i}{\rho_\mathrm{t} D_{i0}^\mathrm{e}} = \frac{1}{P}\frac{\mathrm{d}P_i}{\mathrm{d}x} - \frac{x_i B_0}{\eta D_{i0}^\mathrm{e}}\frac{\mathrm{d}P}{\mathrm{d}x} \quad i = 1, ..., n \ . \tag{2.15}$$

The fluxes of the individual species are represented by J_i. P_i and x_i denote the partial pressure and molar fraction of species i, while η is the mixture viscosity and B_0 is the viscous permeability coefficient. D_{ij}^e are the effective binary diffusion coefficients, which include a correction accounting for the porosity and the tortuosity of the porous medium. The effective diffusion coefficient D_{i0}^e accounts for the drag on species i by the Dusty Gas representing the solid pores. The expression for a single-component fluid can be derived from eq. (2.15):

$$J_x = -\left(\frac{D_0^\mathrm{e}}{RT} - \frac{\rho_\mathrm{t} B_0}{\eta}\right)\frac{\mathrm{d}P}{\mathrm{d}x} \ . \tag{2.16}$$

Although this expression bears considerable similarities with eqs. (2.14) and (2.11), it has been criticised to be contradictory (Bhatia et al., 2011). Moreover, the Dusty Gas model is criticised in general of having a number of key flaws with respect to modelling the flow of fluids in porous solids (Bhatia et al., 2011). First, the Dusty Gas is assumed to be randomly distributed, which is not the case for geometrically well-defined pores. Second, fluid densities are assumed to be uniform, neglecting solid-fluid interactions and confinement effects. Third, an arbitrary distinction between viscous and diffusive flux is introduced, which causes contradictions in the frame of reference for the definition of diffusion. Especially non-uniform fluid structure influenced by solid-fluid interactions poses a seemingly non-reconcilable limitation for the Dusty-Gas model. Extensions to non-ideal and dense fluids is equally problematic and contradictory (Bhatia et al., 2011; Keffer et al., 2005).

Numerous more advanced mass transfer models have been proposed in the literature. The details of these are beyond the scope of this work and they are only mentioned briefly, omitting the details of their advantages, pitfalls and intricacies. A significant amount of these advanced models are variations of the Maxwell-Stefan approach tackling some of the caveats of the Dusty Gas Model. Interfacial friction-based models are directly based on the Maxwell-Stefan theory and bear considerable similarities with the Dusty Gas Model (Schneider, 1978; Kerkhof et al., 2001; Zhdanov and Roldughin, 2002). It is not surprising that these models suffer from similar weak-

nesses, namely the neglect of non-uniform fluid density in nanopores and a large number of empirical parameters. Similarly based on the Maxwell-Stefan description, a generalised approach (Krishna and Wesselingh, 1997) was conceived in order to incorporate surface diffusion effects into the mass transfer model by superimposing the diffusion of an adsorbed layer to the Maxwell-Stefan diffusion model. For very narrow pores where an adsorption field acts within the whole range of the pore, the straightforward superposition of surface diffusion is problematic. Based on the Knudsen diffusion model, Bhatia et al. (2004) developed the so-called "Oscillator Model" (Jepps et al., 2003, 2004), giving an exact theory for low-density fluid transport in the presence of adsorption effects. This accounts for the fact that collision dynamics under adsorption to the pore surface are fundamentally different from hard-sphere wall collisions considered by the Knudsen model. Roughness of a molecular surface can also be incorporated in this approach, which makes it a promising approach to be extended to finite densities. While it is possible to extend the approach to finite gaseous densities, modelling high-density, liquid-like fluids seems to be very challenging. Considering a complex molecular structure of the fluid also seems to be a severe limitation of the "Oscillator Model" for practical purposes (Bhatia et al., 2011). More applicable to diffusion processes of dense liquids is the Local Average Density Model (LADM) (Bitsanis et al., 1987, 1988). It can be viewed as a method to combine exact theories for the low density with continuum models which account for inhomogeneities in fluids densities as well as momentum exchange with the confining wall.

2.3 Single-component mass transfer of a confined fluid

For the analysis of molecular simulations, it is convenient to make the distinction between a flow induced by diffusion ($\mathbf{J}^{\mathrm{D}}$), which does not need to be accompanied by a pressure gradient, and the flow which is induced by an external force (e.g. a pressure gradient), called convective flux here ($\mathbf{J}^{\mathrm{C}}$). Notwithstanding this conceptual distinction, both convective (pressure-driven) and diffusive contributions are present in most cases, and the total flux, $\mathbf{J}$, may be formally decomposed into a diffusive flux and a convective flux:

$$J_{i,x} = J_{i,x}^{\mathrm{D}} + J_{i,x}^{\mathrm{C}} = -\sum_{j=1}^{m} L_{ij} \left(\frac{\partial \mu_j}{\partial x} \right) - \kappa_{\mathrm{p}} \left(\frac{\partial P}{\partial x} \right) \ , \tag{2.17}$$

where the diffusive contribution is described via an Onsager approach and the linear phenomenological transport coefficient for pressure-driven mass transport is represented by the permeability κ_{p}. For simplicity, the expression in eq. (2.17) is in the x direction only, which stands for the main direction of mass transport in a porous material. This formulation of mass transport garnered wide-spread support in the literature (Travis and Gubbins, 2000a; Nicholson, 1997), because the expression simplifies to a very straightforward model if the flux of only a single component is considered. Additionally, the porous material has a unique influence which is not specified and apparent a priori. However, there are conflicting views (Bhatia and Nicholson, 2003) to this distinction between diffusive and convective components in the literature, in particular in the case of single-component transport in a porous solid. The Gibbs-Duhem equation gives a direct relationship between the system's natural thermodynamic variables, which in the case of a confined fluid are temperature T, pressure P and, since the porous solid has an interface with the confined fluid, surface tension γ (Nicholson and Parsonage, 1982).

$$\sum_{i}^{m} N_i \mathrm{d}\mu_i = -S\mathrm{d}T + V\mathrm{d}P + A\mathrm{d}\gamma \tag{2.18}$$

For a bulk single-component system at constant temperature with no present interface, the equation reduces to $\mathrm{d}\mu = \mathrm{d}P/\rho$. Since chemical potential, pressure and density gradient are then dependent on each other, it highlights that a strict separation of diffusive and convective flux is not applicable for a single-component fluid. This aspect is also intuitively apparent as diffusion is a process associated to mixtures. The diffusion of a guest specie in a porous material is instead described by a gradient in

one thermodynamic variable that can be translated into the gradient of another and a flux can be linked to either.

$$J_x = -L\left(\frac{\partial \mu}{\partial x}\right) = -\kappa_{\mathrm{p}}\left(\frac{\partial P}{\partial x}\right) = -D_{\mathrm{p}}\left(\frac{\partial \rho}{\partial x}\right) \tag{2.19}$$

It is important to note that these coefficients are functions of pore loading and surface pressure, so the pressure of the adsorbing fluid and the interactions between solid and fluid, which govern pore loading, have a decisive influence on L, κ_{p} or D_{p}. Because it is most intuitive to measure density in a molecular simulation, the latter version is generally preferred over the other two entities. The connection between chemical potential and density, for instance, can be made as follows:

$$J_x = -L\left(\frac{\partial \mu}{\partial \rho}\right)_T\left(\frac{\partial \rho}{\partial x}\right) = \left[\frac{k_{\mathrm{B}}TL}{\rho}\right]\left[\frac{\rho}{k_{\mathrm{B}}T}\left(\frac{\partial \mu}{\partial \rho}\right)_T\right]\left(\frac{\partial \rho}{\partial x}\right) \ , \tag{2.20}$$

and making the assignment of

$$\Gamma = \frac{\rho}{k_{\mathrm{B}}T}\left(\frac{\partial \mu}{\partial \rho}\right)_T = \frac{1}{k_{\mathrm{B}}T}\left(\frac{\partial \mu}{\partial \ln \rho}\right)_T \ , \tag{2.21}$$

where Γ is a dimensionless thermodynamic correction factor, sometimes called *Darken* factor (Maginn et al., 1993). Here, the specific contribution of surface effects is included in the thermodynamic correction factor and averaged for the entire pore. With the methodology applicable to both homogeneous and inhomogeneous systems, as the one studied via non-equilibrium simulation methods in Chapter 3 and 4, this aggregate view allows a comparison in terms of external bulk pressure of the fluid. The Darken factor may be related to the adsorption isotherms for inhomogeneous systems (Krishna, 2009; Chempath et al., 2004). When the chemical potential of a substance is expressed in terms of activity a ($\mu/\mu_0 = k_{\mathrm{B}}T\ln a$), the thermodynamic factor can be expressed as $\Gamma = (\partial \ln a/\partial \ln \rho)_T$. Equivalently, in terms of fugacity f, $\Gamma = (\partial \ln f/\partial \ln \rho)_T$. For low density gases, the Darken factor approaches unity, as the fugacity tends to the pressure and the ideal gas law is applicable.

As mentioned, it is convenient to express the flux equation in terms of a gradient in density and therefore eq. (2.21) can be used in eq. (2.20), which yields:

$$J_x = -D_0\Gamma\left(\frac{\partial \rho}{\partial x}\right) \ , \tag{2.22}$$

where D_0 is the corrected diffusivity, defined as $D_0 \equiv k_{\mathrm{B}}TL/\rho$.

It is important to point out that the transport coefficient in eq. (2.22) is comprised of a thermodynamic component (Γ) and a component accounting for the particle mobility of the substance (D_0), which is commensurate with other transport models such as the solution-diffusion model (Hofmann et al., 2000) or models for liquid transport in a porous membrane (Deen, 1987), which include thermodynamic effects in a so-called partition coefficient. In summary, for isothermal mass transfer of a pure species through a porous medium, there is a relationship between the various diffusion coefficients:

$$D_\mathrm{t} \neq L\frac{k_\mathrm{B}T}{\rho} = D_0 = D_{1,\mathrm{p}}^{\mathrm{MS}}\,. \tag{2.23}$$

An extension of these relations to binary mixtures has been presented and discussed in the literature (Wang and LeVan, 2008). Moreover, the expression for pressure-driven flux yields a relation between permeability and diffusion coefficients:

$$\kappa_\mathrm{p} = D_0\Gamma\left(\frac{\partial\rho}{\partial P}\right)_T\,. \tag{2.24}$$

As much as composition has a decisive influence on diffusion rates, so does confinement and it is important to note that the influence on transport diffusion is not equivalent to the influence on self-diffusion. The confined single-component fluid therefore provides a special scenario to investigate confinement effects on self- and transport diffusion independently and allows this study to go beyond focusing purely on the influence of confinement on self-diffusion. In the following chapter, the necessary tools to investigate diffusion by performing molecular simulation are described in detail, followed in Chapter 4 by a concrete example which is based on the theoretical framework above. In Section 6.1, an alternative scenario highlights the relationship between transport and self-diffusion.

CHAPTER

THREE

THE MOLECULAR SIMULATION "TOOLBOX"

> *Nous devons donc envisager l'état présent de l'univers comme l'effet de son état antérieur et comme la cause de celui qui va suivre. Une intelligence qui, pour un instant donné, connaîtrait toutes les forces dont la nature est animée, et la situation respective des êtres qui la composent, si d'ailleurs elle était assez vaste pour soumettre ces données à l'Analyse, embrasserait dans la même formule les mouvements des plus grands corps de l'univers et ceux du plus léger atome: rien ne serait incertain pour elle et l'avenir, comme le passé serait présent à ses yeux.*
>
> Pierre Simon Laplace,
> *Essai philosophique sur les probabilités* (1814)

Before digital computing engines came to see the world's turbid skies in the 1940s, calculating the collisions in an ensemble of many individual particles was a very tedious endeavour. Because statistical thermodynamicists hoped to gain valuable insight into a wide range of challenging problems, the effort certainly did not prevent such endeavours from being undertaken. In fact, Lord Kelvin delegated the tasks to his research assistant, William Anderson, who calculated 5000 random collisions with curved surfaces over the course of thirteen months (Thomson, 1901; Allen and Tildesley, 1987; Izmailov and Myerson, 2005). At the turn of the twentieth century, the fundamental workings of the atomic hypothesis were still disputed and scientists were going great lengths to either produce definitive proof of their theoretical approach or finally refute a competing approach. Nowadays, a computer can calculate a set of 5000 random collisions in less than a millisecond. It will still require a human intellect to write the instructions for such a computation though, which will take considerably longer than a millisecond. Yet it will probably take much less time than calculating

these trajectories by hand. In the current digital age, most will indeed feel sorry for Mr. Anderson for the thirteen months a computer could have saved him. Nonetheless, his efforts exemplify that the value which can be derived from a trajectory of a molecular ensemble was recognised before computer simulations were possible. Very early on, the trade of engineering realised the value of molecular simulations and this particular field of science was often pushed forward by scientists in chemical engineering departments around the world. Since the mid 20th century, there has been a continuous stream of contributions that were added to this molecular simulation "toolbox", in which individual tools often combine breakthroughs in computer science, mathematics, and physics. This selection of tools can be applied to practical issues faced in the engineering disciplines.

In light of this tradition of molecular simulations, this chapter is devoted to the thermodynamic roots of molecular simulations, followed by a discourse of molecular interactions, synonymously referred to as "interaction potentials" or "force fields". Subsequently, molecular simulation techniques to calculate transport coefficients are reviewed, in particular ways to obtain diffusion coefficients. The focus of this work lies on non-equilibrium techniques and, at the end of this chapter, a modified methodology to perform robust and efficient non-equilibrium molecular simulations is outlined.

3.1 The thermodynamic roots of Molecular Simulations

Not only was the scientific development of molecular simulations vigorously influenced by practical engineering problems, but also the origins of thermodynamics are inextricably linked to engineering in the truest sense of the word. The invention of the engine spawned the science of classical thermodynamics, which is traditionally devoted to understanding the relationship between heat and work. In the 19th century, the technical interest in the steam engine fostered a profound scientific analysis of processes that transform heat into work. The young engineer Sadi Carnot poineered the theoretical thermodynamic treatment and a few years later, the work of James Joule and Robert von Mayer manifested the equivalence of heat and work (Müller, 2007).

Since much of the 19th century was devoted to exploring this rapidly emerging field, thermodynamics can therefore still be considered a relatively young field of science. Incidentally, the foundation of its main pillars, the first and second law of thermodynamics, drew from the attention of other disciplines in the natural sciences. It

was the biologist Hermann von Helmholtz who is credited as discovering the conservation of energy in his experiments on fermentation, which constitutes a holistic formulation of the first law of thermodynamics. More importantly, the science of thermodynamics realised the relevance of non-stationary processes very early on. While many natural phenomena are observed in a state of equilibrium, non-stationary, time-dependent, or non-equilibrium processes (all these terms are mostly synonymous) are prominent in nature and technology. The second law of thermodynamics, which provides an answer to the question why some processes cannot be reversed despite the reverse process complying with the first law, was introduced by Rudolf Clausius and complements the theoretical framework of classical thermodynamics. While these laws of thermodynamics were established as simple truths of nature, it did not halt the inquiry into "why" things behave according to these simply rules. With more evidence pointing towards the accuracy of the atomic hypothesis, an explanation of thermodynamic phenomena with an atomistic argumentation was shaped by Ludwig Boltzmann, Josiah Willard Gibbs and James Clerk Maxwell. Their work founded the field of statistical mechanics, the groundwork of molecular thermodynamics and thus the foundation for molecular simulations. The turn of the previous century was marked by numerous ground-breaking discoveries in relation to the atomic hypothesis. Boltzmann's work on statistical mechanics, giving rise to a molecular explanation of macroscopic properties of bulk fluids, was undeniably of immense value for science. Following Boltzmann's pioneering work, other physical phenomena were under scrutiny for a potential basis in molecular character. As such, Albert Einstein showed that Brownian motion, in itself the basis for diffusion, can be explained by molecular thermodynamics (Einstein, 1905). As outlined in section 2.2, the continuum description of diffusion was made only a few decades prior to Einstein's seminal theoretical work. Likewise, Maxwell and Stefan were attempting to incorporate the work of Adolf Fick into the contemporary understanding of thermodynamics and statistical mechanics.

The paradigm shift took place as previously empirical observations could be explained through a rigorous statistical analysis and the assumption that matter consists of individual atoms and molecules rather than being a continuum. Relationships that were previously established could now be broken down to more basic assumptions. In consequence, it became apparent that the bulk properties of a medium are governed by the microscopic interactions between the molecules. A statistical observation of the molecular system yields all intensive and extensive thermophysical quantities.

Insight into the microscopic behaviour of a system allows for the determination of a vast number of properties that are of interest to scientists and engineers. These capabilities were the foundation for the scientific and technical demand for systems to be simulated on a molecular level. Apart from the breadth of information becoming available, information which was previously not accessible via experimental observation could be obtained. In other instances, the possibility to replace dangerous and expensive experiments with computer simulation is beneficial (Borak and Diller, 2001; Jasperson et al., 1996). In yet other instances, the replacement of routine experimental work for tedious tasks, such as sensitivity analyses or parameter scanning, was perceived as a remedy which high-throughput molecular simulations in great numbers could provide (Wilmer et al., 2012). The list of potential applications for molecular simulations is virtually endless. In many cases, researchers use molecular simulations to scope a system of interest and rapidly screen the system for the conditions that are most interesting to be explored experimentally (Smit and Maesen, 2008; Gubbins and Moore, 2010; Wilmer et al., 2012; Amrouche et al., 2012; Hart and Colina, 2014).

3.1.1 Molecular interactions

The physical properties of a substance are determined by the intermolecular forces between the atoms and molecules the substance consists of. While statistical mechanics establish the connection between microscopic configurations and a system's macroscopic state, molecular simulations provide access to microscopic configurations based on a well defined model for the force fields. The molecular interactions are the treasure chest of thermodynamics, since they govern the movement of molecules and hence determine the evolution of molecular trajectories. Once the motion and position of all molecules in a system at all times is known, thermodynamic observables follow from the interaction potential and it is possible to determine temperature, pressure, chemical potential, entropy or any other physical property of the substance in a straightforward manner as a statistical ensemble average. In fact, molecular simulations are often useful for obtaining properties which are difficult to determine experimentally, such as isobaric heat capacities, shear viscosities, surface tensions or diffusion coefficients. Due to the pivotal role molecular interactions play in obtaining physical properties from molecular simulations, one of the main challenges is modelling the molecular interactions effectively and defining the right force field given computational, numerical, mathematical and practical constraints.

Molecular modelling

Generally speaking, molecular modelling is an attempt to describe the plethora of interactions between molecules in mathematical terms, resulting in a functional description of an average potential energy which combines different physical effects such as Pauli repulsion, dispersion interactions (i.e. van-der-Waals forces), electrostatic interactions, hydrogen bonding etc. While these effects can be classified as *inter*molecular forces, there are also numerous types of *intra*molecular forces, which keep the atoms within a molecule together. Historically, molecular interactions have evolved in their complexity, from simple ideal-gas and hard-spheres, via the square-well potential and Lennard-Jones potential, up to polarisable force-fields and a quantum-mechanical treatment of intra- and intermolecular forces (Stone, 2013).

The importance of dispersion interactions for vapor-liquid equilibria, subject of much inquiry and long-standing debate in scientific circles of the 18th and 19th century (Lafitte et al., 2013), was irrefutable since the work of van der Waals (van der Waals, 1873) in the late 19th century and the early 20th century, which also marked the proposal of the *Lennard-Jones* potential (LJ) (Jones, 1924; Lennard-Jones, 1931). The Lennard-Jones potential is of specific interest for molecular simulations as it is a simple, closed-form mathematical function capable of representing the effective potential energy of a simple isotropic fluid in a a qualitative way. The interaction potential u_{ij} is defined by

$$u_{\mathrm{LJ}}(r_{ij}) = 4\varepsilon \left[\left(\frac{\sigma}{r_{ij}} \right)^{12} - \left(\frac{\sigma}{r_{ij}} \right)^{6} \right] , \tag{3.1}$$

with r_{ij} being the distance between the centres of two equivalent LJ particles i and j. In conjunction with van der Waals's approach to molecular interactions, two parameters σ and ε define the LJ potential and scale the size and interaction energy between two particles, respectively. The widespread use of the LJ potential roots in the convenience of its computation and not its particular accuracy in representing the forces between molecules. While the exponent of the attractive term, $(\sigma/r_{ij})^6$, has a theoretical basis, the repulsive term, $(\sigma/r_{ij})^{12}$, is obtained by merely taking the square of the attractive term, which makes for a very fast and efficient computation. Such efficiency was of significance when computing power was scarce and it was necessary to use every short-cut, but with an increasing availability of computational capacity, force fields have become more versatile (and arguably more accurate). Nonetheless, the LJ potential is still the most widely used force field and it constitutes a reference

for every other force field because of the vast amount of data and comparisons that have accumulated in the literature.

In addition to the dispersive and repulsive interactions, molecular models must often account for *electrostatic interactions* due to a non-uniform charge distribution within molecules. This can be done by the inclusion of point charges. The Coulomb interaction, i.e. the attraction or repulsion of two charged sites i and j, is described by

$$u_{\mathrm{C}}(r_{ij}) = \frac{1}{4\pi\epsilon_0}\frac{q_i q_j}{r_{ij}} \ , \tag{3.2}$$

where r_{ij} is the distance between the point charges q and ϵ_0 denotes the permittivity of vacuum. The forces between molecules that exhibit differences in electronegativity within the molecule can also be modelled with multipoles. A hydrochloric acid molecule, for instance, exhibits a strong dipole due to the high electronegativity of the chlorine atom. By modelling this charge distribution with a single dipole rather than two individual charges, the number of interactions sites can be reduced. This can be taken further and higher order poles can replace even more partially charged sites as in the case of a model for carbon dioxide, where two negative charges on the oxygen atom and a positive charge on the carbon atom can be replaced by a single quadrupole (Gray and Gubbins, 1984). Reducing the number of interactions sites N is useful because, if no short-cuts are taken, the number of computations for this N-particle system increases with $N!$. However, defining dipole moments as well as the magnitude and location of charges requires molecular models to go through a challenging optimisation process. It is also worth noting that the LJ potential decays with $1/r^6$, while Coulombic interactions only decay with $1/r$. They have a much longer range than dispersion interactions. The higher the order of the type of polarity, the quicker it decays with respect to distance. For example, the decay of dipolar interactions is proportional to $1/r^3$ and quadrupolar interactions decay with $1/r^5$.

In a similar way to the intermolecular interactions, one may postulate simple closed-form analytical expressions for the forces acting within a molecule. The functional forms of the intramolecular interactions in the molecular simulations presented in this work are the following:

$$U_{\mathrm{intra}} = \sum_{\mathrm{bonds}} [k_1(l-l_0)^2] + \sum_{\mathrm{angles}} [k_2(\theta-\theta_0)^2] + \sum_{\mathrm{torsions}} [k_3(1-d\cos n\phi)] \tag{3.3}$$

where k_i denote the force constants, which will be different for each type of bond (Wang et al., 2004; Martin and Siepmann, 1998). The equilibrium bond lengths l_0,

bonding angles θ_0, and torsion angles ϕ (also called dihedrals) are specific model parameters and can also be optimised based on the model's representation of physical properties or quantum mechanical calculations.

In this work, the simple LJ potential provides the basis for an investigation of the slit pore system presented in Chapter 4. In the subsequent chapters, real gases are modelled based on a combined potential comprised of the LJ force field, partial charges and bonded interaction. Likewise, for the force field for a microporous polymer a combination of bonded and non-bonded interactions (LJ and point-charges) is employed.

It is a true challenge to derive, find and employ the "right" potential for the system of interest. There are many assumptions, simplifications and trade-offs that need or should be made when choosing a force field for a specific purpose. It is essential that a force field is validated for the material and property of interest to provide confidence in the results obtained.

To this date, many different potential models have been developed. Force fields exist that were designed to model specific fluid properties, for example gas viscosity, vapour pressure or saturated liquid density or surface tensions (Reid et al., 1987; Avendaño et al., 2011). A range of studies have tried to produce transferable force fields which can be used without purpose-fit parameter optimisations. Among them are the so-called Optimized Potentials for Liquid Simulations (OPLS) (Jorgensen et al., 1996), transferable force fields to model small molecules (e.g. Transferable Potential for Phase Equilibria (TraPPE) (Rai and Siepmann, 2007)), force fields applicable to a wide range of polymeric systems (e.g. Polymer Consistent Force Field (PCFF) (Sun et al., 1994)). The force field should be chosen with care to model the system of interest, as each is usually generated for specific types of system to model certain properties. In light of the specific requirements and known or unknown limitations of a force field, one can say that the agreement with measurable physical properties is desired in molecular simulations, as well as the efficiency with respect to computational effort.

"Short cuts"

The theoretical basis of statistical mechanics builds on the assumption that systems can be taken to the thermodynamic limit, which means that the number of particles N of the N-body system under consideration is very large, ideally somewhere close to N_A (6.022×10^{23}). Repeatedly calculating the interactions between so many particles is infeasible and mostly unnecessary. To this end, a number of "short cuts" that lower

the computational effort have been invented.

In the present study, hydrogen atoms are incorporated into larger atomic clusters such that groups like CH_2 and CH_3 constitute a single interaction site. This is referred to as the *United-Atom* approach, and many generalised force fields have adopted this approach. Apart from less interaction sites reducing simulation time, hydrogen atoms have a minor effect on the thermophysical properties if hydrogen bonding plays no major role.

Another short cut is the introduction of *periodic boundary conditions* (PBC) and the *minimum image convention*. The number of atoms in a molecular simulation is still extremely small compared to the number of atoms in thermodynamic systems on the macroscopic level. Therefore, PBC are applied to mimic the conditions of an infinite quasi-bulk medium (Metropolis et al., 1953; Allen and Tildesley, 1987). The simulation box is treated as a single cell in the center of an infinite periodic lattice of identical cells. Once a molecule moves out of the simulation box on one side, it re-enters the simulation box on the opposite side. By applying periodic boundary conditions, the simulation box has effectively no walls and the fluid has no phase boundaries. The system can thus avoid surface and confinement effects and essentially imitate a subsystem of the bulk. Since the number of interaction partners of a particle rises to infinity, the *minimum image convention* is applied, meaning every molecule only interacts with a single "image" of every other particle (Allen and Tildesley, 1987).

Yet another short cut aimed at reducing the amount of interactions to be repeatedly evaluated is the *cut-off radius* (Frenkel and Smit, 2001), which defines the distance beyond which any interactions are neglected or accounted for implicitly. In order to mitigate the effect of non-differentiable energy potentials, the LJ cut-and-shifted potential was introduced as a variation of the LJ potential. Here, the potential energy is truncated at the cut-off radius r_c, but the potential energy within the cut-off radius is also shifted by the potential energy at the cut-off.

$$u_{cs}(r_{ij}) = \begin{cases} 4\varepsilon \left[\left(\frac{\sigma}{r_{ij}}\right)^{12} - \left(\frac{\sigma}{r_{ij}}\right)^{6} - \left(\frac{\sigma}{r_c}\right)^{12} + \left(\frac{\sigma}{r_c}\right)^{6} \right] & r_{ij} < r_c \\ 0 & r_{ij} \geq r_c \end{cases} \tag{3.4}$$

It must be noted that shifting the potential and choosing different cut-off radii yields different potentials with different microscopic and macroscopic physical properties. Alternatively, the truncated energy of a potential can be accounted for implicitly. One can assume that the volume outside of the cut-off sphere is made up of a homogeneous fluid of constant density. The correction term added to the potential is then given by

$$\Delta u_i = 2\pi\rho \int_{r_c}^{\infty} u(r) r^2 dr \ . \tag{3.5}$$

When determining the potential energy of the entire system of N molecules, the assumption of *pairwise additivity* between two molecules reduces the number of interactions significantly by neglecting the fact that the presence of other molecules alters intermolecular forces between two molecules.

$$u_{\text{total}} = \frac{1}{2} \sum_{i=1}^{N} \sum_{j=1}^{N} u_{ij} = \sum_{i=1}^{N} \sum_{j>i}^{N} u_{ij} \ . \tag{3.6}$$

This is in principle an incorrect assumption. The extent to which three-body interactions are affecting the accuracy of a simulation has been studied (Sadus and Prausnitz, 1996) and it accounts for deviations of less than 5 % in the worst cases. In this study multi-body interactions are neglected. The effects of multi-body interaction can in fact be averaged and generally included in 'effective' pair potentials.

Finally, the interaction between two unlike LJ particles can be specified by the *Lorentz-Berthelot* combining rules (LB):

$$\sigma_{\text{AB}} = \frac{1}{2} \left(\sigma_{\text{A}} + \sigma_{\text{B}} \right) \ , \tag{3.7}$$

$$\varepsilon_{\text{AB}} = \sqrt{\varepsilon_{\text{A}} \times \varepsilon_{\text{B}}} \ . \tag{3.8}$$

The interaction parameters of species A and B are combined to yield the parameters σ_{AB} and ε_{AB}. Combining rules are of crucial importance when simulating mixtures, but they also apply when a molecular model consists of several different LJ particles and a particle interacts with a different particle of another molecule. Apart from the LB combining rules, a whole range of different combining rules have been proposed. The LB combining rules remain the most popular choice, however.

In general, thermodynamic and structural properties may be expressed in reduced units for all physical quantities including temperature, density, and time. This is done in most of this work with the exception of Chapter 5. The quantities are defined as $T^* = k_{\text{B}}T/\epsilon$, $\rho^* = N_{\text{f}}\sigma^3/V$ and $t^* = t\sqrt{(\epsilon/m)}/\sigma$. The asterisk will be omitted and only be specifically denoting reduced units where confusion with physical units is possible. The LJ parameters and m, which represents the molecular weight, can be used to express all other units of interest. For instance, diffusion coefficients may be expressed in units of $\sigma\sqrt{(\epsilon/m)}$.

3.1.2 Stochastic and deterministic simulation methods

The two most wide-spread simulation methods are Monte Carlo (MC) simulations, which are of stochastic nature, and Molecular Dynamics simulations, based on a deterministic approach (Allen and Tildesley, 1987; Frenkel and Smit, 2001; Rapaport, 2004). A profound historical account of the development as well as advantages, limitations and future challenges of both Monte Carlo (Theodorou, 2010) and Molecular Dynamics (Maginn and Elliott, 2010) can be found in the literature. To a large extent, Molecular Dynamics have lagged behind Monte Carlo techniques in obtaining equilibrium properties. However, due to its deterministic nature, it gives a realistic description of the dynamics of a microscopic system, which in turn can be exploited to calculate transport properties. Moreover, the parallelisation of deterministic Molecular Dynamics algorithms has proven to be easier to implement than for Monte Carlo algorithms. Recent advances in parallel computing architectures give Molecular Dynamics an edge in performing complex large-scale simulations with many trillions of particles (Eckhardt et al., 2013). The following sections will clarify the specific approach of both Monte Carlo and Molecular Dynamics techniques and the role they played in this work.

Monte Carlo Simulations (MC)

Force fields provide the functional form and parameters to calculate the total configurational energy U of an ensemble of N atoms as a function of their coordinates (r^N):

$$U_{\text{total}} = U_{\text{intra}} + U_{\text{inter}} = U(\mathbf{r}_1, \mathbf{r}_2, \mathbf{r}_3, \ldots \mathbf{r}_N) = U(\mathbf{r}^N) \tag{3.9}$$

with the functional forms of intra- and intermolecular potentials differing in complexity between force fields. The total energy of the system is a complex function of all the positions of the particles (configurational part) and the momenta of all particles (kinetic part) which together constitute the system's phase space. The functional form of the internal energy is very complex for a dynamic system, yet it clearly has preferred states which correspond to the natural physical tendency of all system's to prefer the state for which its energy is minimised. The role of molecular simulation is to obtain the microscopic structure of a system based on its force field and deducing the thermodynamic observables by sampling the system's phase space and finding these preferred states. The probability of finding a system in a configuration around $\mathbf{r}^N$ is:

$$P(\mathbf{r}^N) = \exp\left(-U(\mathbf{r}^N)/k_\mathrm{B}T\right)/Z \ , \tag{3.10}$$

where Z is the partition function of the system. It's symbol Z stems from the German word *Zustandssumme*, the summation of all states:

$$Z = \int \exp\left(-U(\mathbf{r}^N)/k_\mathrm{B}T\right) \mathrm{d}\mathbf{r}^N \ . \tag{3.11}$$

For a system with more than a handful of particles and a non-trivial functional form for U, it is impossible to compute the partition function directly. Monte Carlo simulations, devised to circumvent exactly this direct calculation of the partition function, are a traditional form to simulate molecular ensembles on computers, dating back to the post-war era (Metropolis et al., 1953). The name, an insinuation to the eponymous casino on the French riviera, stems from the fact that the algorithm uses a process involving random particle movements to sample the phase space. The sampling is based on random evolutions of the system's configuration, which are either accepted or rejected based on the Boltzmann factor $\exp\left(-\Delta U/k_\mathrm{B}T\right)$, where ΔU is the difference in potential energy between the new configuration and the former. This procedure is referred to as importance sampling as it weighs the importance of the states it samples with the Boltzmann factor.

Since the temperature plays a role in the importance sampling, Monte Carlo simulations are usually but not necessarily performed in the Canonical ensemble (N, V, T), i.e. in a system of constant volume, temperature and constant number of particles . In this scenario, the random evolutions are typically random displacements of particles. Different ensembles can be sampled if the random moves and weighing factors are adjusted accordingly, such as systems at constant pressure, which can be simulated by performing small random changes to the system's volume (Panagiotopoulos, 1987). The Grand Canonical ensemble is noteworthy as it allows the simulation at constant temperature, volume and chemical potential (Adams, 1974). Such simulations are very useful for obtaining adsorption properties of a specific system, from which in turn thermodynamic factors can be determined (Theodorou, 2010). For this purpose, random insertions and deletions of particles are additional necessary moves. The probability of insertions P^+ or deletions P^- being accepted or rejected depends on the specified chemical potential and the system's temperature in the following manner:

$$P^+ = \min\left[\frac{V}{\Lambda^3(N+1)} \exp\left(\frac{\mu - \Delta U}{k_\mathrm{B}T}\right) \ , \ 1\right] \ , \tag{3.12}$$

$$P^{-} = \min\left[\frac{\Lambda^3 N}{V}\exp\left(-\frac{\mu + \Delta U}{k_{\mathrm{B}}T}\right)\ ,\ 1\right]\ . \tag{3.13}$$

where μ denotes the chemical potential and the difference in potential energy ΔU is the difference between the inserted or deleted particle being there or not. Λ denotes the thermal de Broglie wavelength ($\Lambda = \sqrt{\hbar/2\pi m k_{\mathrm{B}}T}$), accounting for the thermal part of the Hamiltonian in the partition function.

$$\Delta U = U(N+1) - U(N) \quad \text{or} \quad U(N-1) - U(N) \tag{3.14}$$

A cornerstone of Monte Carlo simulations is the fulfilment of detailed balance, which means that in equilibrium the probabilities of any stochastic manupulation of the simulated system, such as removing and inserting particles or making the system's volume bigger or smaller are equally likely (Frenkel and Smit, 2001). For any Monte Carlo approach, it is important that at the simulated state point the system is able to reach detailed balance.

Molecular Dynamics (MD)

Molecular Dynamics simulations offer a route to obtain the explicit movement of all particles in a molecular ensemble (Alder and Wainwright, 1957; Stillinger and Rahman, 1974). The molecules are regarded as mechanical objects which move and collide predominantly according to classical equations of motion. Quantum effects have been incorporated into MD simulations, but the majority of MD studies treat particles in a Newtonian way in order to maintain computational efficiency. The intermolecular potential yields the force f_{ij} between two molecules by deriving the potential with respect to the distance between the interaction partners i and j:

$$f_{ij} = -\frac{\partial u_{ij}}{\partial r_{ij}}\ . \tag{3.15}$$

The acceleration of the particle follows from the sum of all forces acting on it. A numerical integration is required to compute the specific trajectory of every single molecule during a simulation and acting forces have to be repeatedly updated depending on the movement of the individual particles. The numerical integration is performed by time dicretisation methods, where the trajectories of the molecules are computed over a very large number of small time steps δt. The positions, velocities and accelerations of all particles at a later time $t + \delta t$ are calculated considering the forces acting on the

molecule by the molecules surrounding it at time t, while these forces are often regarded constant during the time step δt. A variety of algorithms exist to perform the time integration, the Verlet, Velocity-Verlet, and Gear predictor-corrector algorithms being popular and effective examples (Allen and Tildesley, 1987). A main concern in the application of these algorithms is the approximation that the forces between the interaction sites are constant throughout the time step. The forces change as the molecules move during the time interval δt. To generate a more accurate trajectory of the molecules, modern algorithms employ a cascaded computation. In the case of the Gear predictor-corrector algorithm, a predicted position of the molecule, based on its velocity and acceleration, helps to calculate the new forces, and therefore the acceleration at the new position. The difference between the former acceleration and the new acceleration is used to correct the new position, velocity and acceleration of the molecule. These corrected values are regarded as the state of the molecule at $t + \delta t$. For each time step, the properties of the micro-ensemble can be determined and averaging over observables at each time step allows for the computation of macroscopic properties (Frenkel and Smit, 2001).

The equations of motion for the particles according to Verlet (1967) are given by:

$$\begin{aligned} \frac{\mathrm{d}\mathbf{r}_i(t)}{\mathrm{d}t} &= \mathbf{v}_i(t), \\ \frac{\mathrm{d}\mathbf{v}_i(t)}{\mathrm{d}t} &= \frac{\mathbf{f}_i(t)}{m_i} \end{aligned} \tag{3.16}$$

where m_i, $\mathbf{v}_i(t)$ and $\mathbf{f}_i(t)$ denote the mass, velocity and total force acting on particle i, respectively. The ideal implementation of the Verlet integration conserves energy and is used to simulate an ensemble in the Microcanonical ensemble (N, V, E). A numerical Verlet implementation introduces errors, which can be minimised by a sufficiently small time step. MD simulations are routinely checked to determine if the system's energy drifts, which indicates to the choice of time step being too long. Also, it must be noted that in equilibrium conditions the total momentum of the ensemble should be zero.

Temperature is proportional to the amount of kinetic energy in the system. The kinetic temperature is given by

$$\mathcal{T} = \frac{1}{3} \sum_{i=1}^{N} \frac{m_i v_i^2}{k_\mathrm{B} N}, \tag{3.17}$$

The number of degrees of freedom for a point mass is 3, hence the factor of one third on

the right hand side, in accordance with the equipartition theorem. A single LJ sphere does not have any rotational degrees of freedom, thus each LJ particle has the same three translational degrees of freedom. The number of degrees of freedom is $3N$ in a system containing N single LJ spheres.

The equations of motion can be modified to constrain the temperature of the system in order to perform simulations in the Canonical ensemble at constant temperature. For an isokinetic thermostat (Brown and Clarke, 1984), the introduction of the parameter $\chi(t)$ into eq. (3.16) acts like a friction coefficient that guarantees a constant kinetic temperature $\mathcal{T}$.

$$\begin{aligned} \frac{\mathrm{d}\mathbf{r}_i(t)}{\mathrm{d}t} &= \mathbf{v}_i(t), \\ \frac{\mathrm{d}\mathbf{v}_i(t)}{\mathrm{d}t} &= \frac{\mathbf{f}_i(t)}{m_i} - \chi(t)\mathbf{v}_i(t), \end{aligned} \tag{3.18}$$

subject to the constraint:

$$\frac{\mathrm{d}\mathcal{T}(t)}{\mathrm{d}t} = \frac{\mathrm{d}}{\mathrm{d}t}\left(\frac{1}{k_{\mathrm{B}}N_{\mathrm{dof}}}\sum_{i=1}^{N_{\mathrm{w}}} m_i\mathbf{v}_i(t)\cdot\mathbf{v}_i(t)\right) = 0\ , \tag{3.19}$$

where k_{B} is the Boltzmann's constant, N is the total number of particles, and N_{dof} is the number of degrees of freedom. This is a very useful implementation of a thermostat since for any subsystem that is not subject to a thermostat, the equations of motion that govern their dynamics are the same as in eq. (3.16) setting $\chi(t) = 0$ at every time step. To achieve an increase in computational efficiency, a Verlet list of closest neighbours can be employed when calculating the forces for each time step (Allen and Tildesley, 1987).

3.2 Transport properties from Molecular Simulations

Transport properties are almost exclusively calculated from MD simulations as they yield a time evolution of the microscopic ensemble. In essence, obtaining transport properties from MD simulations is based on the fluctuation-dissipation theorem, which states that a system's response to an equilibrium fluctuation is equivalent to the response to a (small) perturbation. Thus, by monitoring the decay of fluctuations during an equilibrium simulation, it is possible to compute transport coefficients which relate the resulting fluxes to a given thermodynamic driving force, such as a resulting mass

flux due to a gradient in concentration, which embodies a gradient in chemical potential as the driving force. The well-established Green-Kubo relations (Kubo, 1957) are used to essentially express most transport properties, such as diffusion coefficients, viscosity and thermal conductivity, and thereby bestow transport coefficients, which were previously purely perceived as phenomenological relations, a fundamental microscopic definition based on statistical mechanics. Equilibrium Molecular Dynamics (EMD) simulations have been performed to analyse self-diffusivities of liquids since early 1980s (Evans and Morriss, 1984).

In the following, the equilibrium route to obtain various "flavours" of diffusion coefficients from Molecular Dynamics simulations is presented, and subsequently followed by an account of several methodologies to obtain diffusion coefficients from non-equilibrium Molecular Dynamics simulations, which in turn are usually not based on the Green-Kubo formalism.

3.2.1 Self-diffusivity

In the canon of transport properties, *self-diffusion* is a special case, yet a fundamentally important one as it is of high interest to the molecular modelling community. Based on Einstein's molecular theory for diffusion, self-diffusion is the key property quantifying a fluid's mobility. In a bulk system of a pure substance at equilibrium, the self-diffusion is defined as a measure of the mobility of a single tagged particle in a bulk of otherwise identical particles. The corresponding transport property is the self-diffusion coefficient D_s (Maginn et al., 1993; Gubbins et al., 2011). Since random thermal motion of the particles is the source for self-diffusion, it highly depends on the system's temperature and density. In the case of fluid transport through porous materials, confinement also has a non-trivial effect on self-diffusion. The calculation of D_s within a molecular ensemble can be performed using Einstein's relation or equivalently by using the Green-Kubo relations (Chaikin and Lubensky, 1995):

$$D_\mathrm{s} = \frac{1}{2d} \lim_{t\to\infty} \frac{\mathrm{d}}{\mathrm{d}t} \left\langle \frac{1}{N_\mathrm{f}} \sum_{i=1}^{N_\mathrm{f}} |\mathbf{r}_i(t) - \mathbf{r}_i(0)|^2 \right\rangle = \frac{1}{d} \int_0^\infty \left\langle \frac{1}{N_\mathrm{f}} \sum_{i=1}^{N_\mathrm{f}} \mathbf{v}_i(t) \cdot \mathbf{v}_i(0) \right\rangle \mathrm{d}t \ , \qquad (3.20)$$

where $\mathbf{r}_i(t)$ and $\mathbf{v}_i(t)$ are the position and velocity of particle i at time t, respectively, N_f is the number of fluid particles, and d is the dimensionality of the system. In Eq. (3.20), the terms in the angular brackets denote an ensemble average, either of the particle's mean square displacement (MSD) for the first expression on the right-hand-side, or

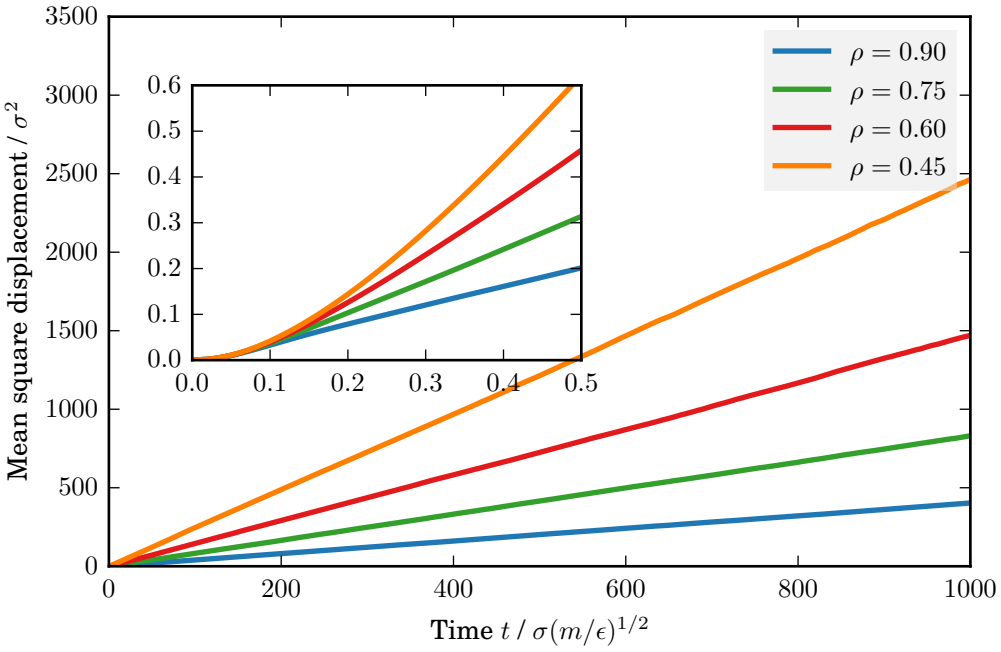

Figure 3.1: Mean square displacements of the bulk LJ fluid at temperature $T = 1.5$ and a fluid density between 0.45 and 0.9.

of the velocity auto-correlation function (VACF) for the second expression. In a dense fluid, the MSD increases linearly with time due to frequent collisions of the particles (Chaikin and Lubensky, 1995). This linear relationship relates to the self-diffusivity, describing the mobility of the particles. An example of MSDs can be seen in Fig. 3.1 showing the time dependence of the MSD of the LJ fluid at various densities. It shows that the MSD exhibits a so-called ballistic regime at short time scales, meaning a quadratic time dependence. It is due to molecules flying through space in a straight line before they eventually collide with each other and embark on a random walk through space. Depending on the density of the substance, the ballistic regime is longer or shorter. The VACF originates from the more general expression for transport properties based on statistical mechanics (Kubo, 1957). The diffusion of a single tagged particle in a mixture of two different species can also be referred to as tracer diffusion, which is closely related to self-diffusion, as outlined previously. The distinction is due to the fact that a tagged particle in a mixture will not only interact with particles of the same species but also with particles of a different species, implying that composition has an influence.

In general, the self-diffusivity D_s and the transport diffusivity D_t (as defined in eq.

(2.1)) are inherently different. For an infinitely diluted mixture of low density gases, the value for D_t, describing the transport diffusion of the solute, approaches the self-diffusivity D_s (Cussler, 2009).

3.2.2 Collective diffusivity

While self-diffusion is a property defined even for single-component fluids, diffusion coefficients usually describe the mass flux within fluid mixtures consisting of multiple components. For such systems, *collective diffusion* is an appropriate measure to account for the concentration dependence of diffusion coefficients. The case of a confined single-component fluid is special as collective diffusion is a defined property of interest for the appropriate systems. As is the case for self-diffusion being calculated from the VACF, it is possible to calculate the collective diffusion coefficient from the collective velocity correlation function (CVCF). As mentioned above, the motion of a single particle is correlated to the motion of other particles within the system. The mobility of a particle is thus inherently a collective property and it is therefore necessary to take the CVCF of the entire system into account. Accordingly, the integration over this CVCF yields the collective diffusivity D_c (Gubbins et al., 2011):

$$D_\mathrm{c} = \frac{1}{2d} \lim_{t\to\infty} \frac{\mathrm{d}}{\mathrm{d}t} \left\langle \frac{1}{N_\mathrm{f}} \left[\sum_{i=1}^{N_\mathrm{f}} \mathbf{r}_i(t) - \mathbf{r}_i(0) \right]^2 \right\rangle = \frac{1}{d} \int_0^\infty \left\langle \frac{1}{N_\mathrm{f}} \sum_{j=1}^{N_\mathrm{f}} \mathbf{v}_j(t) \cdot \sum_{i=1}^{N_\mathrm{f}} \mathbf{v}_i(0) \right\rangle \mathrm{d}t \ . \tag{3.21}$$

As opposed to the VACF, the collective correlation function the CVCF converges very slowly. It can be see in Fig. 3.2 that the CVCF has a long time tail and there is considerable additional simulation effort required in order to compute the collective diffusion coefficient to sufficient statistical accuracy (Maginn et al., 1993). Often, several very long simulations need to be performed to obtain viable results.

It should also be noted that in eq. (3.21), there is an additional summation as compared to Eq. (3.20), but since the movement of individual particles remains part of this summation, self-diffusivity and a cross contribution D_ξ constitute the collective diffusivity. This relationship is more evident when looking at the definition of the CVCF in eq. (3.21) (on the very right hand side), for which the multiplication of the two sums yields the definition of self-diffusivity ($\sum_j \mathbf{v}_j(t) \cdot \sum_i \mathbf{v}_i(0) = \sum_j \mathbf{v}_j(t) \cdot \mathbf{v}_j(0) + \sum_j \sum_{i\neq j} \mathbf{v}_i(t) \cdot \mathbf{v}_j(0)$). Therefore, the self-diffusivity and a cross contribution D_ξ constitute the collective diffusivity: $D_\mathrm{c} = D_\mathrm{s} + D_\xi$. For low density fluids, the correlation of

a specific particle's velocity with the velocity of other particles is negligible compared to its auto-correlation and therefore D_ξ is negligible. The collective diffusivity thus approaches the self-diffusivity at the low-pressure limit (Nicholson, 1997).

Especially for porous media at low pore loading, it is convenient to purely calculate self-diffusion coefficients as it is the most common approach to characterise a system's transport properties. It is fast and convenient to calculate and is clearly defined for a pure substance at equilibrium. It is important to keep in mind, however, that phenomenological transport coefficients, such as the transport diffusivity D_t, or the Maxwell-Stefan diffusivity D_MS are inherent to inhomogeneous and/or multicomponent systems. They only correspond to the self-diffusion coefficient in the special cases of infinite dilution (Reid et al., 1987).

Collective diffusion coefficient are routinely calculated for multi-component mixtures in order to determine Maxwell-Stefan diffusion coefficients (Liu et al., 2011), as there is a sound theoretical basis of the connection between them (Van De Ven-Lucassen et al., 1998). Similarly, it is possible to demonstrate that the collective diffusion coefficient is equivalent to D_0 as defined in the previous chapter (section 2.3).

Since EMD simulation reproduce realistic molecular trajectories, the MSD or VACF can be directly determined from the saved trajectories of a MD simulation by using eq. (3.20) and (3.21). The results can be compared to experimental measurements from PFG-NMR and QENS experiments (Gubbins et al., 2011).

3.2.3 Non-equilibrium Molecular Dynamics

To simulate collective diffusivities from EMD is computationally expensive and therefore non-equilibrium approaches as a direct route to simulate transport phenomena have been pursued. Since diffusion is a process that is invoked by a departure from equilibrium, a multitude of different approaches has been devised, of which the majority drive the system of interest away from equilibrium. These approaches frequently mimic a real experiment in order to link observation from simulation with phenomenological transport properties. *Transient* MD methods are a telling example for this notion. The Gradient Relaxation Molecular Dynamics (GRMD) method was introduced by Maginn et al. (1993) to study mass transport in zeolites. The approach determines the diffusivity by monitoring the time-dependent recurrence of a non-equilibrium system to a state of equilibrium. More specifically, a step profile in the density of a fluid in zeolite cages is imposed and used as a starting point for a transient MD simulation. Diffusive mass transport causes the density profile to smoothly flatten out to a state of

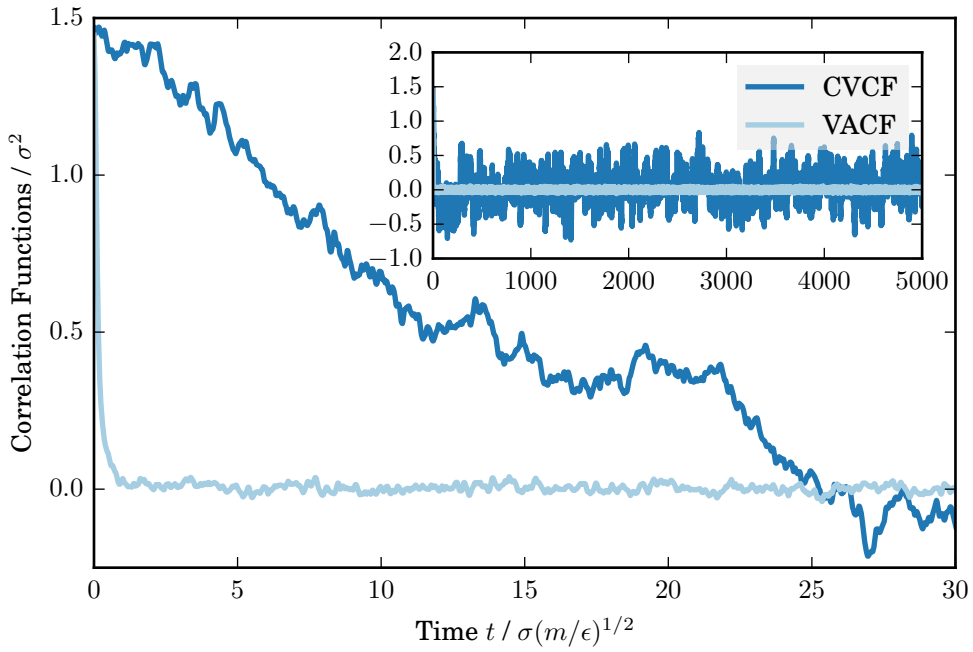

Figure 3.2: Collective and Auto-Correlation functions of the LJ fluid confined in the wide, repulsive pore ($H = 5.0$ with WCA walls) at $T = 1.5$. The pore loading of a unit cell amounted to 305 particles, which corresponds to a bulk pressure of 0.8. The reader is referred to Chapter 4 and Fig. A.8 and A.9 for the resulting values for D_s and D_c.

equilibrium density. The time evolution of the density profile is analysed and yields the diffusion coefficient. A similar methodology was touched on by Salih (2010), the Joule Expansion method, where a fluid is expanded through a capillary or porous medium into an initially evacuated subsystem. The relaxation of the density (pressure) can be analytically related to a Fickian diffusion coefficient. Surely, many similar computer experiments of this transient nature could be envisioned to calculate the diffusivity. The principal difficulty of this methodology, however, lies in determining whether the simulation occurs in the linear response regime as well as in limitations of the statistical reliability.

Another statistically more reliable subcategory of non-equilibrium techniques are methods to simulate a non-equilibrium system in a steady state. Heffelfinger and Swol proposed the Dual Control Volume Grand Canonical Molecular Dynamics (DCV-GCMD) method (Heffelfinger and van Swol, 1994) in an attempt to directly simulate diffusive flux triggered by a gradient in chemical potential and in the absence of a pressure gradient. To this end, an elongated simulation box is divided into three relevant compartments. Reservoir compartments are located at the right and left end of the system and the flow region is located in the centre, between the two reservoirs. Each reservoir is kept at a constant chemical potential by inserting and deleting particles from the reservoir. In one instance, the simulated fluid is divided into two species that only differ in colour. By keeping high and low chemical potential regions for the two species on opposite sites of the simulation box, an individual flow of each of the coloured species is induced in spite of the overall system being kept at constant density. In other instances, a single component fluid is simulated and imposing a difference in chemical potential leads to one reservoir being at a higher pressure than the other, which in turn allows a net flux to occur in the flow region (Travis and Gubbins, 2000a). The DCV-GCMD method has the advantage that it is evident whether a simulation happens in the linear response regime or not. While the steady state nature of the process improves the statistical uncertainties of this method as averaging may be performed for long simulation times, the combination of stochastic and deterministic elements poses a challenge for two reasons (Arya et al., 2001). First, inserted particles must be assigned a velocity that matches the average streaming velocity, which in turn is not known a priori. Second, the insertion and deletion of particles alters the dynamics of the molecules and the number of insertion or deletion events can have a limiting influence on mass transport.

Last but not least, the External Field Non-Equilibrium Molecular Dynamics (EF-

NEMD) method has been one of the first methods introduced (Evans and Morriss, 1984), although wide spread use of this method was hindered by limitations in computational power as the systems studied usually need to be relatively large to yield reliable results. The approach itself is straightforward and following the general notion of non-equilibrium thermodynamics. An equilibrated molecular dynamics sample is taken out of equilibrium by a weak external force field acting on all (or part) of the fluid particles. The external field implies an additional acceleration in a specific direction, producing a macroscopic flux in the same direction. For small perturbations, it is common to regard this external force field equivalent to a chemical potential gradient. It can be compared to gravity homogeneously acting on all particles of the sample. However, the external field is an extension to the Hamiltonian of the ensemble (Allen and Tildesley, 1987), and thus it has an effect on the interaction between particles. The effect might not be negligible in some cases, in particular, when considering the interaction between fluid and wall particles. Moreover, some reservation to the EF-NEMD method are targeted towards the fact that it has not been formally demonstrated under what conditions the equivalence of external field and chemical potential gradient is justified and when and if the assumption breaks down (Arya et al., 2001). Nonetheless, more recent publications indicate that the method yields good results and shows greater potential for an extension to more complex systems (Chempath et al., 2004).

3.3 Boundary-driven non-equilibrium MD

Owing to its efficiency and ease of application, the EF-NEMD method has been modified recently by making the external field act only in a sub-region of the system. This avoids the fact that an external field alters the Hamiltonian of the particles in the region of interest. A few studies have applied related approaches to investigate contraction and expansion of fluid flow (Castillo-Tejas et al., 2009), the permeation of water through transport proteins (Zhu et al., 2004), pressure-driven transport through nanoscopic cylinders (Huang et al., 2011) and transport through different graphitic pores (Salih, 2010).

The investigation in this work is based on a variation of the EF-NEMD method (Frentrup et al., 2012). The external field also acts as a quasi-gravitational field in the x direction, i.e. in the direction of the flow, but only in a thin slab at the left boundary of the simulation box (see the red shaded region in Fig. 3.3) in order to induce the flow with the minimal perturbation to the system.

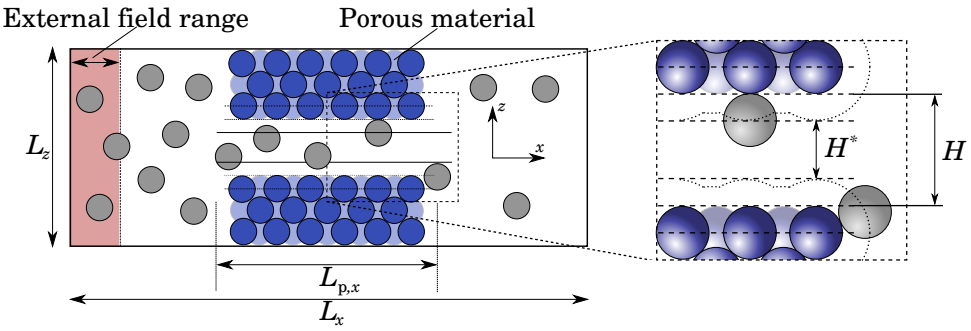

Figure 3.3: Schematic representation of the slit pore geometry. Blue spheres fixed by harmonic springs represent the particles of a porous solid. Gray spheres are fluid particles. Periodic boundary conditions are applied in all directions. A close-up of the slit pore channel and the definition of the pore width H^* are also shown. The volume accessible to the fluid is schematically depicted by the dotted line. The y direction (in plane) is not shown.

Periodic boundaries apply in all three dimensions (Frenkel and Smit, 2001), but due to the application of the external field, the density is not uniform in the entire system. The external force, acting in the x direction, builds up a pressurised bulk on the left of the porous structure, provoking an increase in density in this region. The fluid is squeezed into the porous structure and flow through the slit pore develops. While the density in the bulk region is uniform for a moderate perturbation, a linear density gradient develops within the pore. In order to quantify the differences in density, the density distribution along the length of the pore was measured. To this end, the simulation box was divided into thin slabs. For each slab, the average amount of molecules was measured during the simulation and a density profile along the x direction, the direction of flow, can be obtained. The flux can be measured by counting net molecular movements in the x direction. It is also possible to save the initial positions of the fluid particles, obtain the unwrapped final positions of fluid particles and deduce, from these two sets of data, the overall displacement corresponding to the net flux. This approach essentially yields an average velocity v_x, and it is thus very convenient to directly measure velocities during the simulations and compute the net molar flux from the conservation of mass ($J_x = \rho \times v_x$). Due to continuity, the flux must be constant throughout the simulation box.

The simulations yield a difference in density as well as the flux triggered by this density gradient and based on these observables a “Pseudo-Fickian” approach can be

used to determine the effective diffusion coefficient, which is thus defined as:

$$J_x \approx -D_{\text{eff}} \left(\frac{\Delta\rho}{\Delta x} \right) . \tag{3.22}$$

Eq. (3.22) establishes the relationship between the flux and a gradient in density via the effective diffusion coefficient. With the bulk densities available from the simulations, the density gradient can be expressed as:

$$\frac{\Delta\rho}{\Delta x} = \left(\frac{\rho_{\text{right}} - \rho_{\text{left}}}{L_{\text{p},x}} \right) , \tag{3.23}$$

where $L_{\text{p},x}$ is the length of the respective pore. Due to the external field acting on the fluid particles, dissipated heat increases the temperature of the fluid during the simulation and the removal of this excess energy from the simulation is crucial to perform steady state simulations. In order to maintain a simulation at constant temperature, rather than applying a thermostat to the fluid particles, which can negatively influence the calculation of transport properties, the release of excess dissipated heat was carried out by applying a thermostat only to the wall particles of the system. The wall particles vibrate about their lattice positions and heat is transferred from the fluid to the wall through particle collisions, leaving the motion of the fluid molecules unperturbed by the thermostat.

The described boundary-driven NEMD methodology is tested on model systems with a LJ fluid flowing through a planar slit pore in the centre of the simulation cell. The slit pore was constructed using a hexagonal closed packed lattice and the solid particles were tethered to their lattice positions using a harmonic potential. For the fluid particles, the cut and shifted LJ potential (Vrabec et al., 2006) was used. The molecular diameter shall be referred to as the intermolecular distance where the potential energy is zero, σ. The cut-off distance of the LJ potential was chosen to be 2.5σ. For the solid-solid and fluid-solid interactions, a purely repulsive potential known as the Weeks-Chandler-Andersen (WCA) potential was used (Weeks, 1971). The WCA potential is a cut and shifted LJ potential with a cut-off radius $r_{ij}^{\text{c}} = 2^{1/6}\sigma$. For soft-sphere molecules, such as the LJ fluid and the WCA wall, the pore width and length cannot be defined unambiguously (Travis and Gubbins, 2000b). For the following discussion, the pore width H shall be defined as the distance between the centre of mass of the inner-most wall layer less one molecular diameter of a fluid molecule, while the width accessible to fluid, H^*, is the pore width H less one molecular diameter of a fluid molecule, as outlined in Fig. 3.3.

Pore size H	2.5	2.5	5.0	5.0
Dimensions of the simulation box [σ]				
Simulation box length L_x	40.0	80.0	40.0	40.0
Simulation box depth L_y	8.736	8.736	8.736	8.736
Simulation box height L_z	13.113	13.113	10.371	26.096
Number of wall molecules N_{w}	1200	2400	600	2400
Number of fluid molecules N_{f}	1490	2958	1412	2982
Est. volume accessible to fluid V [σ^3]	2695.9	5506.1	2589.5	5529.5
Est. overall fluid density [$1/\sigma^3$]	0.553	0.537	0.545	0.539
Porosity H^*/L_z	0.115	0.115	0.386	0.153
Pore length $L_{\mathrm{p},x}$	18.6	36.03	18.6	18.6

Table 3.1: For the purpose of validating the boundary-driven NEMD approach, four different pore geometries were constructed. The system parameters are listed above. The volume accessible to the fluid is estimated by subtracting a box-shaped sections for the wall structure. The values were calculated by subtracting the volume of the porous medium from entire box volume ($V_{\mathrm{est}} = [(L_x L_z) - L_{\mathrm{p},x}(L_z - H^*)]L_y$), meaning that smooth edges of the pore wall were not explicitly taken into account.

Two different values for the pore width were realised in order to shed light on the influence of various combinations of system parameters. Namely, a narrow pore with a pore width $H = 2.5$ and a wide pore with $H = 5.0$. In order to investigate finite size effects, a smaller system and a larger system was created for each of the two pore sizes. While the system of the narrow pore was stretched along the length of the slit pore in the x direction, the system of the wide pore was enlarged perpendicular to the pore in the z direction by adding more layers of wall molecules. The details of the systems' geometry are given in Table 3.1.

The slit pore lies symmetrically in the centre of the simulation box. The pore length $L_{\mathrm{p},x}$ is defined as the distance between the outer-most wall particles plus 2σ. Thus, the pores have a length of 18.6 and 36.03σ for the three short and the long systems, respectively. The values given for the volume accessible to the fluid, V, in Table 3.1 are close estimates for the actual accessible volume.

It can be seen from Table 3.1 that the overall fluid density was kept constant for the

different test systems. The systems were equilibrated for 200 000 time steps during which a steady state could be reached. Subsequently, a production run of 2.5 million time steps was performed to obtain measurements for molar flux and density gradients. Simulations were performed for a variety of external field magnitudes between 0.05 and $0.7\epsilon/\sigma$. The thin slab in which the external force acts was chosen to be three molecular diameters.

Density gradients of different magnitudes of the external field are shown in Fig. 3.4. The grey shaded area depicts the location of the pore. Measuring the density in the bulk regions is an uncomplicated task as the available volume in these regions is correctly defined. However, the density within the pore is subject to the complications in defining the pore width. Furthermore, at the entrance and exit of the pore, the available volume changes in an abrupt fashion, going from bulk to confinement. This point transition was not explicitly taken into account in the density profiles, and thus creates the spikes in the profiles. The spikes are located at the entrance and exit of the slit pore. The average density in the bulk sections was taken only from the simulations from which the difference in density could be calculated unambiguously. A weak external force invokes a linear response in the density distribution at these conditions producing constant bulk densities and linear density gradients inside the pore

The density gradient and the difference in bulk densities increase with the magnitude of the external field. Depending on the system setup, the response is non-linear for larger magnitudes of the external force field (Frentrup et al., 2012). The gradient inside the pore deviates from a linear gradient and for the large system, even the bulk density can depart from being uniform. A similar conclusion can be derived from Fig. 3.5b. The ratio of the difference in bulk densities between the upstream and downstream sections, i.e. the density gradient that induces the flow, $\Delta\rho$, may be calculated directly. While the molar flux is linearly correlated to the external field, as can be seen in Fig. 3.5a, the increase in $\Delta\rho/\Delta x$ shows a growing deviation for high magnitudes of the force field. These larger external forces ($f_{\mathrm{ex}} \geq 0.3\epsilon/\sigma$) correspond to situations removed from the linear regime and should be treated with care, if at all.

For the small realisation of the wide pore, the deviation of $\Delta\rho/\Delta x$ from a linear response is most prominent (triangles in Fig. 3.5b). It is obvious that the fluid faces less resistance from the porous structure compared to the other realisations because the ratio of the void area to the total area is much smaller than in the other cases. Porosity is given as a measure to evaluate this aspect and the values for each system's porosity are given in Table 3.1. By enlarging the system and adding porous structure in the z

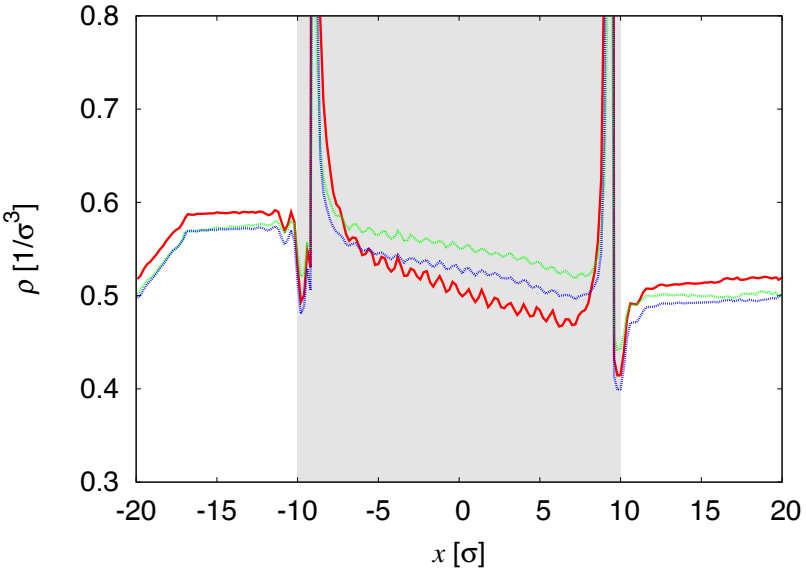

Figure 3.4: Density profiles along the length of the simulation box, i.e. in x direction for a range of external forces. The profiles are shown for the small realisation of the narrow pore (red) and both small (blue) and large (green) realisation of the wide pore at an external force of $f_{\text{ext}} = 0.2$. The grey shaded area in the centre depicts the region in which the pore is located.

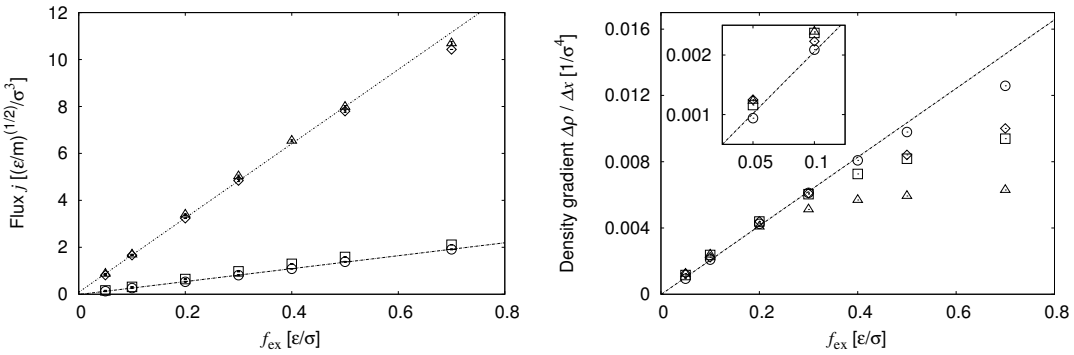

(a) Response of the molar flux.

(b) Response of the density gradient.

Figure 3.5: Influence of the external force field on (a) the molar flux and (b) the density gradient, $\Delta\rho/\Delta x = (\rho_{\text{right}} - \rho_{\text{left}})/\Delta L_x$. Circles and squares represent the small and large realisation of the narrow pore, triangles and diamonds the small and large realisation of the wide pore, respectively. The straight dashed lines are a guide to the eye.

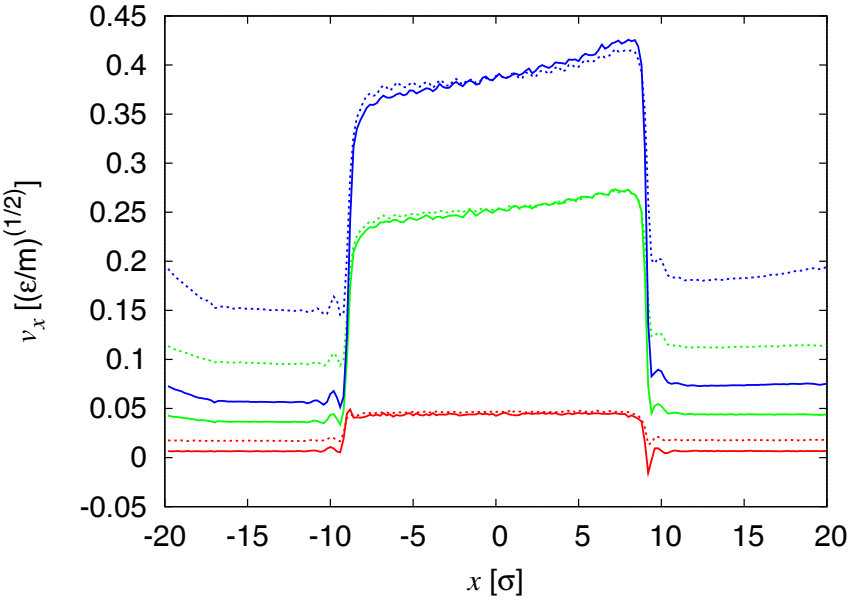

Figure 3.6: Average streaming velocity profile for the wide pore at two different porosities. Solid lines depict the system at low porosity (i.e. large realisation in Fig. 3.1) while dashed lines represent the results of the high porosity system (i.e. small realisation in Fig. 3.1). The profiles are for $f_{\text{ex}} = 0.05, 0.3$ and $0.5\epsilon/\sigma$ from bottom up.

direction, the porosity is greatly reduced and a larger bulk subsystem is created. As a consequence, the fluid cannot cross through the pore as easily. Similar observations can be made when analysing the average particle velocity in the flow direction. The reduction of porosity reduces the streaming velocity of the fluid in the bulk sections while the streaming velocity in the pore is the same as for the more porous system. As shown in Fig. 3.6, the bulk streaming velocity is more than halved in the bulk subsystems by reducing the porosity from 0.386 to 0.153.

Only the wall was thermostatted during these NEMD simulations with an isokinetic thermostat and therefore the effective removal of heat is important to ensure that simulation results are comparable to the equilibrium state. In Fig. 3.7, the temperature plots shows that the external field has a strong influence on the extent to which simulations depart from thermal equilibrium. The temperature profiles in Fig. 3.7 also shows that low magnitudes of the external field only result in a slight departure from thermal equilibrium. It was furthermore observed that an increase in system size facilitates the effective removal of heat (Frentrup et al., 2012), which seems logical as it also increases the interface between solid and fluid.

The dependence of D_{eff} on the external force is plotted in Fig. 3.8. The figure shows

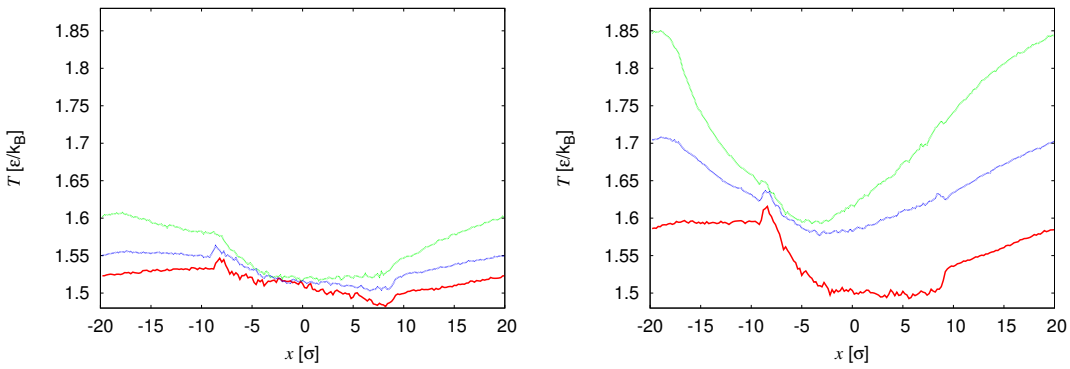

(a) $f_{\mathrm{ex}} = 0.2$ **(b)** $f_{\mathrm{ex}} = 0.5$

Figure 3.7: Temperature profiles for the small realisation of the wide pore. The profiles for an external force of $f_{\mathrm{ex}} = 0.2$ are shown on the left in a) and for $f_{\mathrm{ex}} = 0.5$ on the right in b).

that the effective diffusivity is not independent of the external field applied. As is expected, D_{eff} increases with the magnitude of the external field. Also, the results for the larger and the smaller system deviate from each other; as entrance effects play a larger role for the smaller system, a lower effective diffusion coefficient for the small system is expected.

Based on linear response theory, the quantity of interest is the limit of D_{eff} as the force tends to zero (Kjelstrup et al., 2010), corresponding to the transport diffusion coefficient D_{t}. As can be seen in Fig. 3.8, this quantity is independent of the size of the system, and both small and large realisations of each pore width coincide. For $H = 2.5$, an effective diffusion coefficient for a vanishing external force field is $(D_{\mathrm{eff}})|_{f_{\mathrm{ex}}\to 0} = 9.55(5)$, where the number in parentheses gives the uncertainty in the last digit. For $H = 5.0$, $(D_{\mathrm{eff}})|_{f_{\mathrm{ex}}\to 0}$ is equal to $18.6(1)$. Certainly, the coefficient changes with the available pore opening as expected. There is a compromise between applying an extremely small external force, which would guarantee that the system remains in the linear regime (thus extrapolation to zero force would be meaningful) but would exhibit poor statistics due to the poorly developed flow and a large external flow which produces an efficient simulation and smaller fluctuations but may correspond to an excessive perturbation of the system. There is no recipe for the precise magnitude of the force to be used.

The fact that the results obtained for effective diffusivities are independent of the system size is an outstanding feature of this methodology. The traditional pitfall of

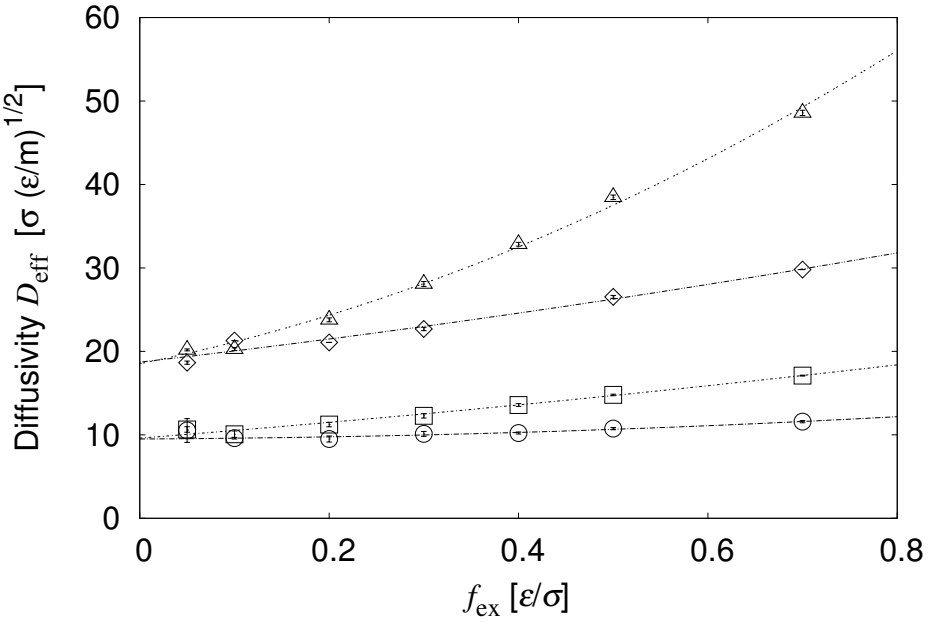

Figure 3.8: Effective diffusivities for the narrow and wide pore. Circles (small realisation) and squares (large realisation) denote the narrow pore system, triangles (small realisation) and diamonds (large realisation) denote the wide pore system. Errors are estimated as the deviation between several runs for the same state point. In general, the error bars are smaller than the symbols. The dashed lines are a weighted least square fit to quadratic functions for which the relative errors were used to weigh the data.

non-equilibrium techniques are primarily the departure from the linear response regime and for an inhomogeneous system such as the one simulated in the present work, finite size effect can play a major role in determining the importance of entrance effects. The simulation results give faith that both these issues could be mitigated by extending to the limit of zero external force for the calculated diffusivities.

Many simulation studies revert to treating the solid as a rigid structure and apply a thermostat to the fluid. This can result in large errors when computing dynamic properties such as diffusion coefficients as the dynamics are artificially modified in order to account for thermalising effect of the solid.

The simulations presented in this chapter were performed with a purpose-built MD code. However, it is also important to note that the methodology was devised in order to allow for easy implementation into existing MD software packages. Given the breadth of potential applications and the extensive functionality of existing freely available MD packages, the methodology was implemented into the software packages DL_POLY and LAMMPS. It was soon realized that the capabilities of LAMMPS (Plimpton, 1995), and especially its suitability to implement non-equilibrium MD simulations with versatile options for thermostatting and applying perturbations, were beyond those of the DL_POLY package. Therefore, in the subsequent chapters, simulations were performed with the LAMMPS simulation code (Release date: 25 July 2012).

CHAPTER

FOUR

MODELLING OF DIFFUSIVE MASS TRANSPORT IN PLANAR SLIT PORES

Essentially, all models are wrong, but some are useful.

G. E. P. Box and N. R. Draper,
Empirical Model Building and Response Surfaces (1987)

4.1 Introduction

Porous materials are classified and to a large extent specifically chosen for industrial separation purposes based on their pore width. Steric effects are a comprehensive tool to render a porous material selective. Beyond steric effects, confinement may alter the perceived properties of fluids and can influence transport properties significantly. It is very difficult to predict how altered diffusion dynamics, such as ballistic or single-file diffusion, change the separation characteristics of a porous material.

The most relevant characteristics and technical criteria for porous materials are pore width and pore size distribution, surface area, and structure factors, i.e. tortuosity and porosity, which are both related to pore size distribution to some extent. Moreover, solid-fluid interactions and wall rugosity have a decisive influence on wall friction. They interplay with the former characteristics by influencing adsorption behaviour and transport dynamics, such as wall slip and other factors on fluid flow. Recently, more control over nanoscale features of a material has spurred the investigation of fluid behaviour in nanoscale confinement, i.e. in materials with pores smaller than 2 nm, which renders them microporous materials according to the International Union

of Pure and Applied Chemistry's (IUPAC) definition of pore sizes (McNaught and Wilkinson, 1997; Schuth et al., 2002).

The effect of a pore size variation on the mobility of fluids in porous materials has focused primarily on cylindrical pores in the form of zeolites (Bhatia, 2010) and carbon nanotubes (Zheng et al., 2012), on slit-shaped pores in the form of graphitic pores (Nicholson, 1998; Vieira-Linhares and Seaton, 2003; Albo et al., 2006) or model structures (Furukawa et al., 1997; Nicholson, 1999). A further advanced molecular representation of porous materials of high interest because of their fluid transport properties includes random structures (Gelb and Gubbins, 1998, 1999), which attempt to embody glassy materials, and virtual carbons (Biggs and Buts, 2006; Marsh and Rodriguez-Reinoso, 2006) as an attempt to model realistic geometries for e.g. amorphous carbon, as well as realistic structures of polymeric membrane materials (Larsen et al., 2011) or materials of biological origins, such as water-transporting proteins (Zhu et al., 2004). The transferability of research findings is limited because the materials can have such different properties that they cannot be compared to other systems. For example, the "density" in cylindrical silicalite pores is often reported in loading per unit cell or zeolite cage, but if no adsorption isotherm is given, it is impossible to relate the results to properties of other systems.

Such lack of transferability is especially unfortunate in the case of the slit pore system, which is often used as a surrogate model for adsorption models (Everett and Powl, 1976). Despite the slit pore model being a popular and relevant model for molecular simulations, data on transport diffusion in slit pores is rare and among the available data, a consensus at the most basic of levels has hardly been reached. As seen in Fig. 4.1, the reported values for transport diffusion disagree by up to two orders of magnitude. This high level of disagreement stems from the fact that the parameter space of a simple planar slit pore system is more extensive and complex than is apparent at first sight. A specific cylindrical zeolite has a fairly narrow definition of pore width, pore surface characteristics and even force-field parameters, which determine solid-fluid interactions. The literature holds countless examples of planar slit pores that have assumed different shape and parameters (Song and Chen, 2008; Travis and Gubbins, 2001; Sokhan et al., 2001). Adding to the complexity, small differences in model parameters, such as slightly different wall collision properties, will often significantly impact transport properties. The nature of fluid-wall interactions is crucial and whether they are defined by wall reflections or by defining a specific interaction potential between fluid particles and wall particles needs to be clearly specified. Nu-

merous simulation studies have established the discrepancies between smooth walls with either diffusive, specular or a combination of these types of reflections and structured, atomic walls (Song and Chen, 2008; Cai et al., 2008). Cai et al. (2008) considered three different pore models for graphite sheets: a smooth wall (Steele potential, see eq. (4.2)), a diffuse thermalising wall and a structured wall. Differences in diffusion coefficient between diffusive, specular and structured pores that differ by four orders of magnitude were reported (Cai et al., 2008). Likewise, the difference between diffusive and specular collisions has been reported by Cracknell et al. (1995a). While the low density diffusion coefficient for specular reflections diverges to infinity, diffusive reflections slow down the transport coefficient and transport and self-diffusion coefficient converge to a limited value. Figure 4.1 also shows the inherent difficulty in calculating transport diffusion coefficients to a high degree of confidence as the results from one and the same laboratory can differ by a sizeable amount. Transport diffusion is a collective property of the system and accumulating a sufficient amount of statistical data to perform a robust analysis is very challenging.

It was pointed out that, while the Steele potential yielded the correct self-diffusivity of the system, a structured wall was necessary for a correct calculation of the transport diffusivity. The thermal diffusive wall did not yield correct results at all.

In contrast, there is much more consensus about the transport diffusion of methane, represented by a single LJ sphere, in a cylindrical silicalite pore. Despite the system's complexity, the parameters are well defined and disallow an open parameter space and ambiguous system parameters. Often, transport diffusivites are reported alongside self- and collective diffusivities and the results from different research groups are consistent (Skoulidas and Sholl, 2002; Maginn et al., 1993).

Since an accurate theoretical treatise for the diffusion of low density gases in pores exists, an accurate treatment of gas transport in pores of varying roughness has been sought (Arya et al., 2003; Jepps et al., 2003; Bhatia et al., 2011). It has been pointed out that the self-diffusion of the ideal gas diverges to infinity and therefore D_{K} must also go to infinity for a Knudsen gas in a perfectly smooth pore exhibiting specular wall collisions (Arya et al., 2003). For rough walls, D_{K} has a limit, however. It depends on the roughness of the pore and is minimal for a pore with purely diffusive reflections. For intermediate scenarios, the magnitude of the effective diffusion coefficient depends on the ratio of specular to diffusive reflections.

Another difficult aspect with respect to comparing transport coefficients is the different trends that self-, collective and transport diffusion follow as the fluid gets

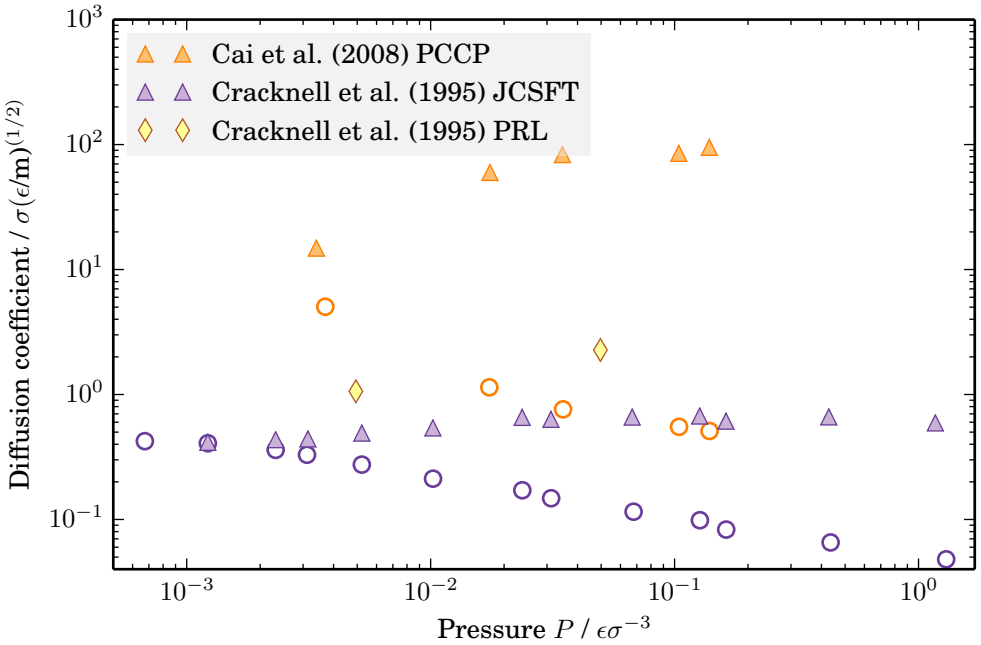

Figure 4.1: A selection of reported simulation data for self- and transport diffusivities of the LJ fluid ((Cracknell et al., 1995a) in purple and (Cai et al., 2008) in orange) inside a planar slit pore. The models are designed for methane adsorption and diffusion in a carbonaceous material at room temperature, which translates to $T = 2.0$ in reduced units. The pore width was 2.5 in both cases. Empty circles denote self-diffusivities while filled triangles denote transport diffusion coefficients. Filled diamonds denote the data reported by (Cracknell et al., 1995b) which just included two different values for transport diffusion.

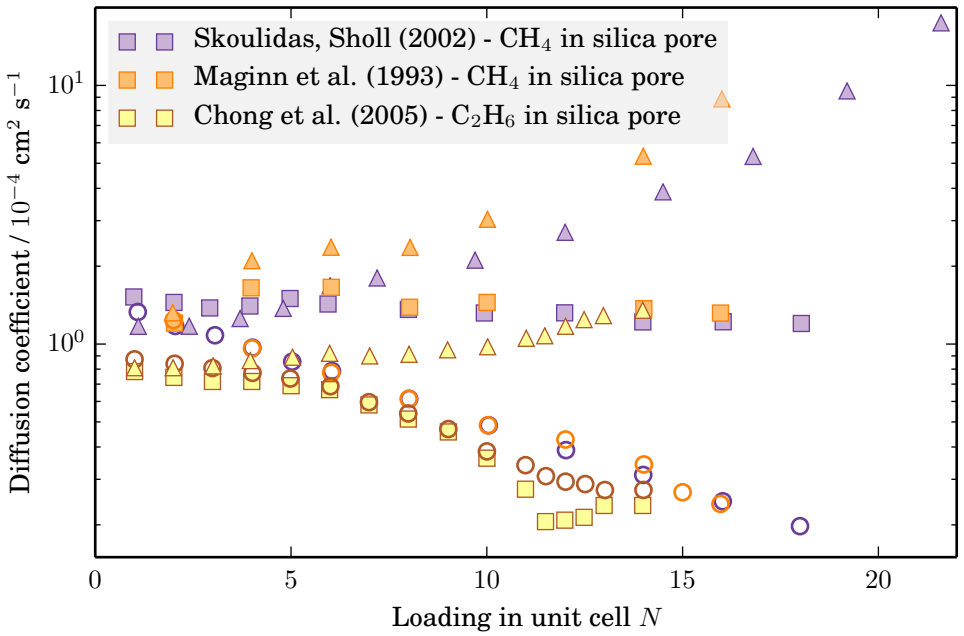

Figure 4.2: A selection of reported simulation data for self-, collective and transport diffusivities of CH_4 ((Skoulidas and Sholl, 2002) in purple and (Maginn et al., 1993) in orange) and C_2H_4 ((Chong et al., 2005) in yellow-brown) inside a cylindrical silica pore. Empty circles denote self-diffusivities. Filled squares and triangles denote collective and transport diffusion coefficients, respectively.

denser. While all three properties need to converge to the same value at the ideal gas limit, self-diffusion rapidly declines as density increases whereas collective and transport diffusion often increase. These trend are confirmed through comparison with QENS and PFG-NMR measurements (Sholl, 2006). It is also widely accepted that collective diffusion is a combination of self-diffusion and cross interactions, and therefore $D_0 > D_s$, which is more significant at higher densities (Skoulidas and Sholl, 2002). While self-diffusivities are commonly reported, collective and transport diffusion coefficients are more challenging properties to obtain. It is very difficult to compute these properties for non-homogeneous systems, such as a fluid under confinement. The proliferation of non-equilibrium simulation methods and increased access to computational resources makes it easier to investigate these properties and reporting is becoming more frequent.

A significant number of studies have been targeted toward calculating the diffusion of guest molecules in cylindrical pores of amorphous silica or on various slit pores models, mostly representing carbon structures. More recently, cylindrical pores representing carbon nanotubes have garnered topical interest. Seldom have the effect of solid-fluid interactions on diffusion coefficients been the focus of an investigation, although the wide variety of conceivable nano-materials as fostered an increased interest in such effects. The exceptional potential for high flux water transport is often attributed to the molecular smoothness of a carbon nanotube, but since pores can be altered through functionalisation, a step change from no transport to high transport can be observed as hydrophilicity of the pore is altered (Melillo et al., 2011).

It is necessary to have a clear picture of how confinement influences fluid transport in a qualitative as well as quantitative way and obtain a better understanding of the properties of the pervasive planar slit pore model. To this end, mainly the effect on self-, collective and transport diffusion due to a variation in pore loading and solid-fluid interactions in two differently sized pores is investigated in this chapter. The investigation is limited to the simple Lennard-Jones fluid confined in a structured planar slit pore of varying interaction potential, namely a repulsive wall, which is comprised of WCA particles, and two attractive walls comprised of LJ particles. The different pore sizes studied are a narrow pore which is 2.5 molecular diameters in width and a wider pore of 5.0σ. In the following, interaction potentials of the pores are compared with common models in the literature first. Then, apart from presenting diffusivities, thermodynamic effects have also been considered and studied by obtaining adsorption isotherms of the different systems of interest. Subsequently, the calculation of

diffusion coefficients for bulk and confined systems is given, including self-diffusion as well as collective and transport diffusivities. Finally, the results are compared to the Knudsen and Hagen-Poiseuille approach to predict fluid flow in slit pores.

4.1.1 Model potentials for a planar slit pore systems

In this work, the walls are comprised of individual LJ particles that are of the same size as fluid particles. They are tethered by a harmonic force to their lattice positions in order to render them part of the solid pore wall. It is nowadays common to model walls explicitly as computing power is less of a limitation. The additional interactions due to wall-wall collisions are permissible. The larger the pore width of the system and the denser the confined fluid, the more the wall-wall interactions become negligible.

However, it was previously very common to model walls implicitly rather than including individual wall particles into the time integration since computational resources were scarce and structured walls were replaced with an averaged wall force field. A direct attempt to describe fluid wall interactions implicitly is the *LJ 9-3 wall potential*. This force field is the result of a straightforward integration of the standard 12-6 LJ potential assuming the individual particles are part of a uniform semi-infinite quasi-continuum wall (Israelachvili, 2011). The resulting potential is a function of a single Cartesian coordinate z, which denotes the distance to the centre of mass of the first layer of wall particles:

$$u_{\mathrm{fw}}(z) = \frac{4}{3}\pi\rho_{\mathrm{w}}\varepsilon_{\mathrm{fw}}\sigma_{\mathrm{fw}}^3\left[\frac{1}{15}\left(\frac{\sigma_{\mathrm{fw}}}{z}\right)^9 - \frac{1}{2}\left(\frac{\sigma_{\mathrm{fw}}}{z}\right)^3\right], \tag{4.1}$$

where ρ_{w} is the number density of the wall particles, σ_{fw} and $\varepsilon_{\mathrm{fw}}$ are size and energy parameters of the fluid-wall interactions, respectively. The main drawback of the LJ 9-3 potential is the assumption that wall particles are uniformly distributed throughout the solid. This is a crude assumption and in reality, they have fixed lattice positions, which has a big influence on the potential energy surface of a pore wall, particularly at close distances and for walls sparsely populated, as can be seen in Fig. 4.3. A pseudo-empirical improvement, which closely resembles the explicit description of walls is the *Steele potential* (Steele, 1978), which is widely used in the literature and often employed to model slit pores of graphitic carbon.

$$u_{\mathrm{fw}}(z) = 2\pi\rho_{\mathrm{w}}\varepsilon_{\mathrm{fw}}\sigma_{\mathrm{fw}}^2\Delta\left[\frac{2}{5}\left(\frac{\sigma_{\mathrm{fw}}}{z}\right)^{10} - \left(\frac{\sigma_{\mathrm{fw}}}{z}\right)^4 - \left(\frac{\sigma_{\mathrm{fw}}^4}{3\Delta(z+0.61\Delta)^3}\right)\right] \tag{4.2}$$

Here, Δ denotes the distance between two successive lattice planes of wall particles. The Steele potential can be understood as an improvement over the LJ 9-3 potential with respect to incorporating the atomic layers of a crystalline wall. The next layer of molecules, which a fluid molecule approaching the wall can interact with, is located at least the distance Δ from the first surface layer. In effect, the Steele potential is an analytical closed-form coarse-grained potential of a structured wall consisting of LJ particles. Free energy mapping of detailed wall-fluid potentials can be performed for any type of force-field, even with structural and energetic heterogeneities (Forte et al., 2014).

The functional form of these effective force fields is solely dependent on the distance z from the wall. Wall collisions have to be addressed explicitly for such a wall force field. As mentioned previously, the choice often falls on either purely specular or purely diffusive collisions. The accuracy of the respective choice greatly depends on the state of the system and surface properties, in particular on fluid density, surface roughness and pore size. While most systems will exhibit diffusive reflections entirely, due to their particularly rough walls, it became apparent over time that specular reflections play a decisive role for nanoporous system. Especially carbon nanotubes exhibit a specifically smooth surface and molecules colliding with the wall of a carbon nanotube are mostly reflected specularly (Bhatia et al., 2005). These arguments become irrelevant if atomistically explicit walls are considered. Because of the increased interest in the transport properties of nanoporous systems, modelling pore walls explicitly has become the state-of-the-art approach.

Figure 4.3 visualises the differences between a range of potentials for planar walls. The dashed lines depict the Steele potential with two different parameter sets, the LJ 9-3 wall and, for reference, a single LJ sphere. The three solid lines show the potential energy surface of the pore walls which are further used throughout this chapter. The blue line depicts the repulsive WCA potential, which is why it does not exhibit a potential well, while red and green lines depict the attractive walls with $\varepsilon_{\text{fw}} = 1.0$ and $\varepsilon_{\text{fw}} = 2.0$, respectively. Interaction potentials were calculated by probing the respective slit pore with a simple Lennard-Jones sphere ($\sigma = 1.0, \varepsilon = 1.0$) and averaging the interactions in the xy plane. Hence, the corrugations in the energy surface cannot be seen in Fig. 4.3.

Because of the closer packing of graphite, both in terms of the in plane packing as well as the shorter layer-to-layer distance Δ, the graphitic Steele potential has the deepest potential well. Fig. 4.3 also shows that the Steele potential with the same para-

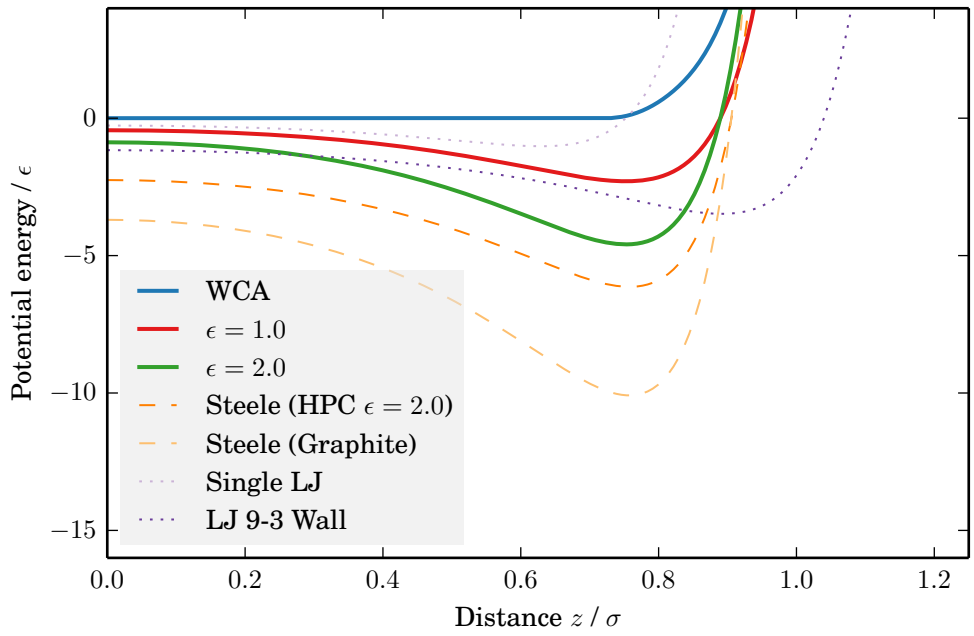

Figure 4.3: Interaction potentials of the structured walls with three different types of interactions (WCA, LJ with $\varepsilon_{\mathrm{fw}} = 1.0$, and with $\varepsilon_{\mathrm{fw}} = 2.0$). For reference, the Steele potential with the same density parameters ($\rho = 0.75$, $\Delta = 0.874$) as well as with parameters for graphite are depicted by dashed lines in orange (Radhakrishnan et al., 2002). In addition, the LJ 9-3 wall potential as well as a single LJ sphere are depicted by the dotted lines in purple. The centre of mass of the first wall layer is located at $z = 1.25$.

meters as the strongly wetting wall (green line) would be a reasonably good model as the interactions potentials are very similar. It is important to note that the location of the well depth for the Steele potential as well as for the structured walls is at the same distance z from the wall. This is dramatically different for the LJ 9-3 wall, which has its potential well shifted towards the wall by almost 0.1σ due to the assumption that interaction sites are uniformly distributed within the solid. A single LJ sphere in turn has a much weaker interaction than any of the wetting walls depicted since only one interaction partner is available in this case. Its potential well is shifted further away from the location of the wall.

4.1.2 System setup of this work

The parameter space for a planar slit pore is very large, as pointed out previously, and it is therefore important to specify the system in detail. Apart from pore width, pore loading and fluid-wall interactions, parameters such as temperature and wall topology can have a stark influence on transport properties. In this chapter, the investigated system is the same planar slit pore system as it is described in chapter 3 (section 3.3), yet the focus of this chapter will be on the influence of fluid-wall interactions which determine the adsorption strength of the pore. To this end, the wall will be modelled in three ways: 1) a repulsive pore comprised of WCA particles ($r_{\mathrm{c}} = 2^{(1/6)}$); 2) a weakly wetting pore made up of LJ particles that are the same as the fluid ($\varepsilon_{\mathrm{fw}} = 1.0$); and 3) a strongly wetting LJ pore with twice as attractive wall particles ($\varepsilon_{\mathrm{fw}} = 2.0$). Moreover, two pore sizes will be simulated, a narrow pore with $H = 2.5$ and a wide pore, $H = 5.0$. Confined inside the pore is the cut and shifted Lennard-Jones fluid with a cut-off radius $r_{\mathrm{c}} = 2.5$. The temperature will be fixed at $T = 1.5$, which is above the critical point of the LJ fluid and thus no phase separation is to be expected inside the pore. Because there are many theories to predict mass transport in pores at low density, the applicability of NEMD at a range of significantly high pore loadings will be a major focus of this chapter.

4.2 Adsorption Isotherms

The thermodynamic factor describes the relationship between two thermodynamic variables, as it was pointed out in Chapter 2. However, the thermodynamic factor of the bulk is different to that of a fluid inside a porous solid. While the relationship between chemical potential and density constitutes the thermodynamic factor of a bulk fluid, it is the relationship between chemical potential and the amount of adsorbed fluid particles inside the pore since density is ambiguously defined for the confined fluid. Thermodynamic factors can thus be determined from an equation of state for a bulk fluid and from adsorption isotherms for the confined fluid (Maginn et al., 1993). A common way to calculate such adsorption isotherms of porous materials is to perform Grand Canonical Monte Carlo simulations (Chempath et al., 2004). In this case a hybrid MD and MC approach was employed, in which Grand Canonical insertions and deletions were carried for the porous system while all particle trajectories were calculated via an MD algorithm instead of random displacements. This

methodology was implemented in the simulation software LAMMPS, since EMD and NEMD simulations were carried out with the same software. This ensures that the force fields and pore structures that were used for GC, EMD and NEMD simulations are exactly the same. Moreover, equations of state are not always available for every bulk fluid and it is convenient to also determine the $P\rho T$ behaviour of a bulk fluid via this Grand Canonical Molecular Dynamics (GCMD) approach. In this case, the integrity of the simulation results of this hybrid GCMD approach is demonstrated by the comparison of $P\rho T$ for the pure LJ fluid (see Fig. 4.4).

4.2.1 Grand Canonical insertions

To ensure the accuracy of GCMD simulations, both a bulk $P\rho T$ behaviour and adsorption isotherms were calculated and the bulk behaviour was compared to an accurate equation of state for the LJ fluid, which is reported in the literature (Johnson et al., 1993). For the calculations of the former, GCMD simulations were initiated on an empty simulation box at a fixed chemical potential. The Grand Canonical insertions quickly fill the simulation box with particles and the fluid quickly attains the density corresponding to the respective chemical potential. Calculations of adsorption isotherms were performed in a similar fashion. The simulation box contains an empty slit pore in such a way that an infinitely big pore is generated due to the application of periodic boundary conditions. The unit cell of the infinite pore is then quickly filled with fluid particles according to the applied chemical potential. Throughout the simulation the number of particles is allowed to fluctuate due to stochastic insertions and deletions. As with Grand Canonical simulation techniques employing random insertions in general, the method works very well for low density fluids. At high densities however, the approach reaches its limits since successful insertions become very unlikely and detailed balance is not guaranteed anymore. In addition, the confinement effect of the pore limits this further. While it was possible to reach fluid densities up to 0.84, which corresponds to a bulk pressure of 5.11, GCMD simulation for the confined systems could only reach bulk pressures between 3 and 4 (in red. units).

The system was thermostatted at a temperature of $T = 1.5$ with a Nosé-Hoover thermostat (Frenkel and Smit, 2001). The time step was chosen at 0.001. Equilibration was performed for 100000 time steps. The production run lasted 200000 time steps. Every 10 time steps 1000 insertions or deletions attempts were undertaken at an equal 50% ratio. The bulk system was cubic with a box length of 20σ. The confined system consisted of a slit pore which was 11.85σ long in the x direction and 10.26σ in the y

direction. The height of the simulation box varied with pore width. For the narrow pore, the simulation box was 6.37σ in the z direction with the pore occupying 3.87σ, while the wide pore was 8.87σ in height. This leaves a pore width of 2.5 and 5.0σ respectively. The pore width is defined as described in chapter 3. The pore system is similar to the pore described in section 3.3, but it is important to note that no bulk sections were in contact with the slit pore in this case.

Figure 4.4 shows simulation data of GCMD simulations for pressure and chemical potential of a bulk fluid as a function of density compared to the data from the Johnson equation of state for the Lennard-Jones fluid (Johnson et al., 1993). A correction term to the pressure was applied since the simulations were carried out with a cut and shifted potential employing $r_\mathrm{c} = 2.5$ as cut-off. The pressure correction (Johnson et al., 1993) is

$$P_\mathrm{cs} - P = -\frac{32}{9}\pi\rho^2\left[\left(\frac{\sigma}{r_\mathrm{c}}\right)^9 - \frac{3}{2}\left(\frac{\sigma}{r_\mathrm{c}}\right)^3\right] . \tag{4.3}$$

The reference point of both simulations and equation of state for the chemical potential, i.e. where $\mu_0 = 0$, was chosen at the lowest simulated density ($\mu_0 = \mu^\mathrm{sim}(\rho = 0.0041) = \mu\mathrm{EoS}(\rho = 0.0041) = 0$). The simulation results are in excellent agreement with the equation of state. This underlines the applicability of the GCMD approach for equilibrium simulations in the Grand Canonical ensemble. Individual plots for pressure vs. density (Fig. A.1), chemical potential vs. density (Fig. A.2), and chemical potential vs. pressure (Fig. A.3) relationships are included in the appendix.

4.2.2 Thermodynamic factor

Bulk Lennard-Jones fluid

Given the confident agreement between simulation and reference equation of state regarding the $P\rho T$ behaviour of the employed cut-and-shifted LJ potential, the obtained data can be used to determine the thermodynamic factor of a pure fluid:

$$\Gamma_\mathrm{bulk} = \frac{\rho}{k_\mathrm{B}T}\left(\frac{\partial\mu}{\partial\rho}\right)_T = \frac{1}{k_\mathrm{B}T}\left(\frac{\partial\mu}{\partial\ln\rho}\right)_T . \tag{4.4}$$

It is important to note that chemical potential and pressure are not independent for the isothermal pure component fluid. The thermodynamic factor can be related to the inverse of the isothermal compressibility (McQuarrie, 2000) (compare section 2.3):

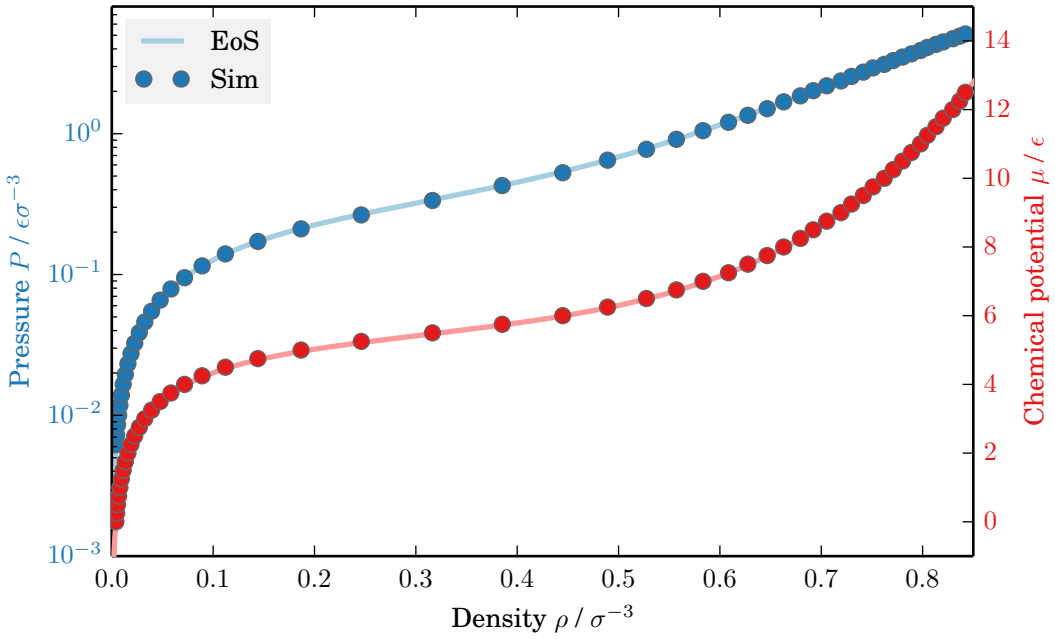

Figure 4.4: Simulation results in comparison to an equation of state for pressure and chemical potential of the bulk Lennard-Jones fluid with cut-off radius at $r_c = 2.5$. The error bars are smaller than the symbols. The blue line represents the results for pressure and corresponds to the axis on the left, while the red line, denoting chemical potential, corresponds to the right axis.

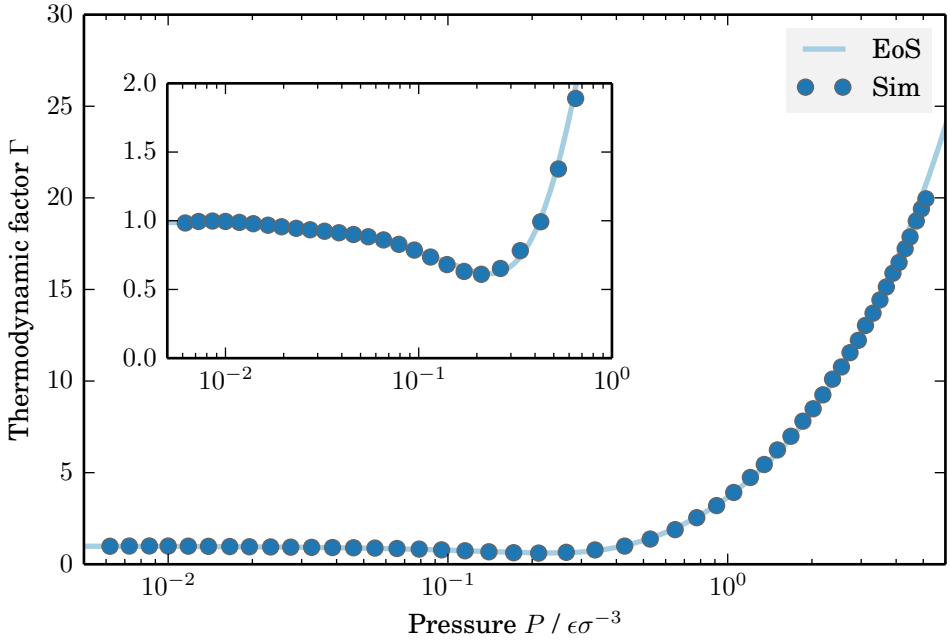

Figure 4.5: Thermodynamic factor of the bulk Lennard-Jones fluid.

$$\frac{\rho}{k_\mathrm{B}T}\left(\frac{\partial\mu}{\partial\rho}\right)_T = \frac{1}{k_\mathrm{B}T}\left(\frac{\partial P}{\partial\rho}\right)_T . \tag{4.5}$$

The results for the thermodynamic factor of the pure LJ fluid as a function of pressure are shown in Fig. 4.5. Results were obtained by numerical differentiation of the equation of state data and for the simulation data by differentiating cubic splines. As the fluid tends to the dilute gas limit, it approaches ideal gas behaviour, for which the thermodynamic factor is 1. The thermodynamic factor has a minimum at a pressure of approximately 0.2 and then rises sharply with increasing pressure. The data from simulation and equation of state also agree very well for this derivative property.

Confined Lennard-Jones fluid

Thermodynamic factors from confined fluids can be obtained from adsorption isotherms rather than an equation of state of the bulk fluid, but this implies that eq. (4.4) does not apply for the bulk fluid. The adsorption isotherms for both small and wide slit pore are shown in Fig. 4.6 and Fig. 4.7, respectively. The fluid uptake, expressed as the number of particles inside a pore unit cell, is plotted as a function of pressure. The difference between a repulsive, weakly and strongly wetting pore walls is apparent. For the system with $\varepsilon_\mathrm{fw} = 2.0$, a significantly increased uptake of fluid particles

	Narrow pore $H = 2.5$				Wide pore $H = 5.0$			
	α	β	γ	τ	α	β	γ	τ
WCA	140.32	4.04	23.38	1.66	324.12	2.16	36.34	1.80
$\varepsilon_{\mathrm{fw}} = 1.0$	378.47	2.19	29.28	1.69	378.47	2.19	29.28	1.69
$\varepsilon_{\mathrm{fw}} = 2.0$	183.56	18.89	36.72	1.69	453.15	7.67	20.66	0.89

Table 4.1: This table shows the fitted parameters of the modified Tóth equation (Eq. (4.6)) for the six isotherms that were determined from GCMD simulations.

especially at lower pressures is clearly visible.

A modified Tóth isotherm (Tóth, 1962) was employed to fit adsorption isotherms to the simulation data:

$$N(P) = \alpha \frac{\beta P}{(1 + (\beta P)^{\tau})^{(1/\tau)}} + \gamma P \, , \tag{4.6}$$

where α, β, and γ denote adjustable parameters to fit to the respective isotherm. The original Toth equation was simply extended with an additional linear term to improve the fit to the data.

The fluid density inside the pore is not well defined and, in addition, the density distribution is not constant throughout the pore. Depending on the fluid-wall interactions and the pore loading, the density distribution can exhibit pronounced adsorption layers and a strong depletion in the centre of the pore, which can be seen in Fig. 4.8. What is more, the pore width will vary slightly along the structured pore, which is made up of individual particles. Due to this ambiguity in the definition of pore density, an alternative definition of the thermodynamic factor for the confined fluid is necessary. Although the pore volume is not well defined, we can assume that it will be the same for all the variations of the slit pore system studied here. Figure 4.3 showed that the potential wells are at the same position for each of the wall potentials, although the WCA wall is an exception here since it has no potential well. When assuming constant pore volume V_{p}, the average molar uptake at a fixed external pressure (corresponding to a fixed chemical potential) is $\langle \rho \rangle = \langle N \rangle / V_{\mathrm{p}}$. One can therefore express Γ as a function of the molar uptake:

$$\Gamma_{\mathrm{conf}} = \frac{\langle \rho \rangle}{k_{\mathrm{B}} T} \left(\frac{\partial \mu}{\partial \langle \rho \rangle} \right)_T = \frac{\langle N \rangle}{k_{\mathrm{B}} T} \left(\frac{\partial \mu}{\partial \langle N \rangle} \right)_T = \frac{1}{k_{\mathrm{B}} T} \left(\frac{\partial \mu}{\partial \ln \langle N \rangle} \right)_T \, . \tag{4.7}$$

The results of eq. (4.7) applied to the simulation data and the respective fits can

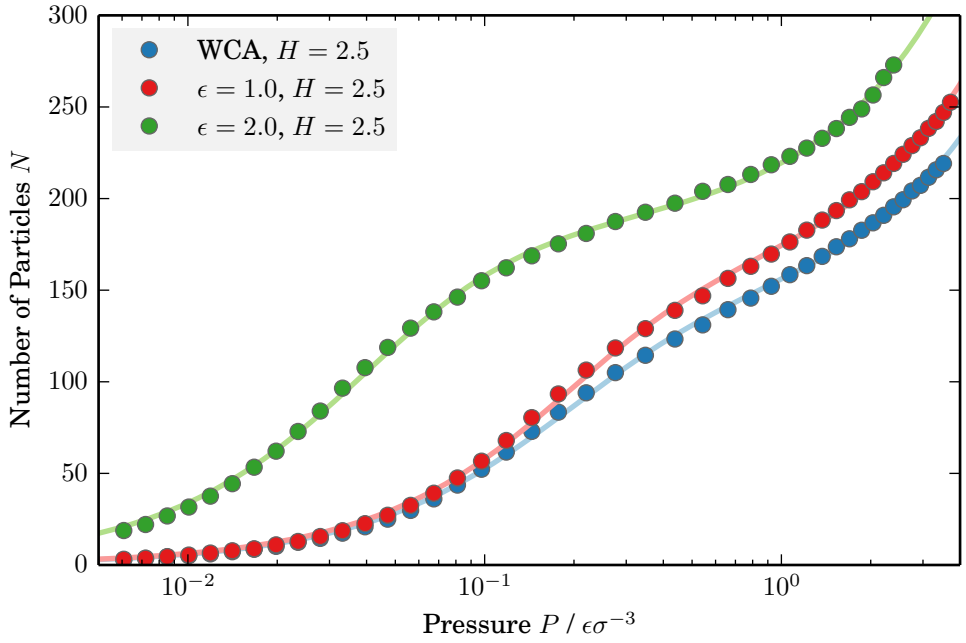

Figure 4.6: Adsorbed particles inside the narrow pore ($H = 2.5$) at the corresponding bulk pressure. The solid lines are obtained by fitting eq. (4.6) to the respective adsorption isotherms.

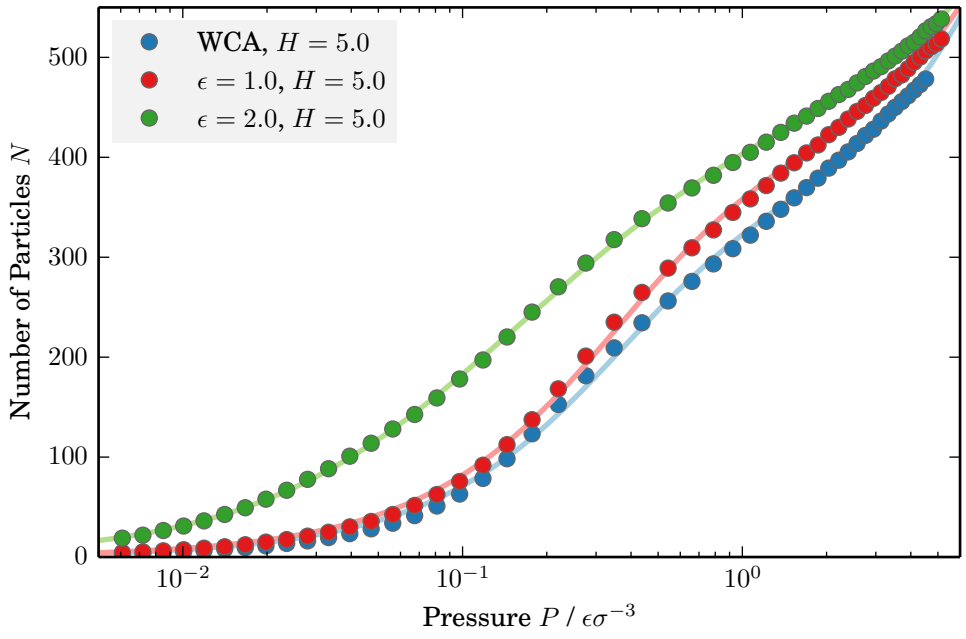

Figure 4.7: Adsorbed particles inside the wide pore ($H = 5.0$) at the corresponding bulk pressure. As in Fig. 4.6, the solid lines denote fits to eq. (4.6).

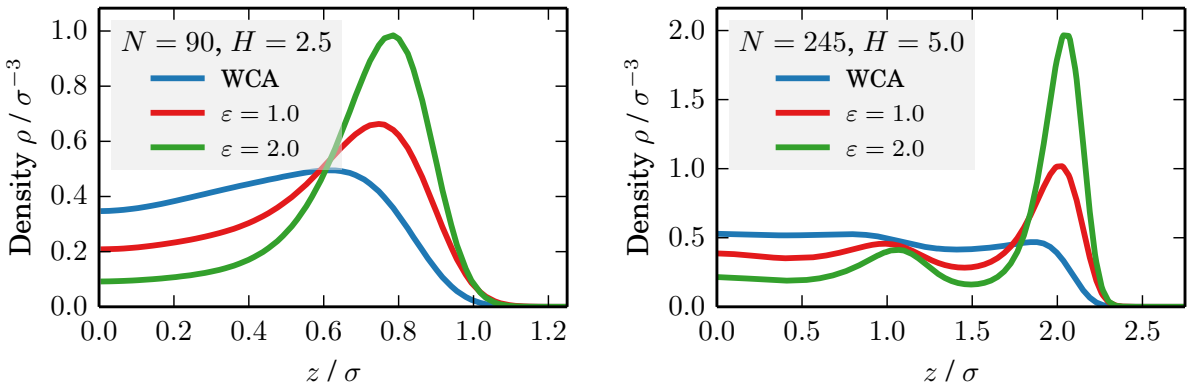

(a) $H = 2.5$ **(b)** $H = 5.0$

Figure 4.8: Profiles of the density distribution inside the narrow pore a) and the wide pore b). The centre of the pore is the origin of the plots and the centre-of-mass of the first layers of the wall particles are located at $z = 1.25$ and $z = 2.5$ for the narrow and wide pore respectively.

be seen in Fig. 4.9 for the narrow pore and Fig. 4.10 for the wide pore. For the low pressure limit, the behaviour is identical to that of the bulk fluid with Γ approaching unity. Figures 4.9 and 4.10 also show that a sharp increase in the thermodynamic factor is to be expected earlier than for the bulk fluid. Both systems show that solid-fluid interactions have an influence on the pressure at which this occurs. Especially for the strongly adsorbing narrow pore shown in Fig. 4.9 (green line denoteing $\varepsilon_{\mathrm{sf}}$), the thermodynamic factor surpasses 1.5 at a pressure of 0.04, while for the bulk fluid the pressure is surpassed at about 0.4, which is an order of magnitude higher than the confined fluid. The effect is not as pronounced for the wide pore, but the effect of a variation in solid-fluid interactions is clearly visible. Although confinement can produce a rapid increase in the thermodynamic factor at lower pressures, the data also indicates to that the thermodynamic factor reaches a limit at higher pressures. Physically, this is to be expected as the uptake into the slit pore is limited. With increasing pressure, it is obvious that fluid transport can only be observed until the fluid solidifies for both bulk and confined fluid. Thus, the thermodynamic factor has a natural upper limit. In fact, a slit pore with strong fluid-wall interactions induces a fluid to solidify inside the pore at a lower pressure compared to a bulk fluid. Determining the limit of the thermodynamic factor with Grand Canonical simulations is impossible, however. Since random insertion cannot be performed for dense fluids, the regions of high pres-

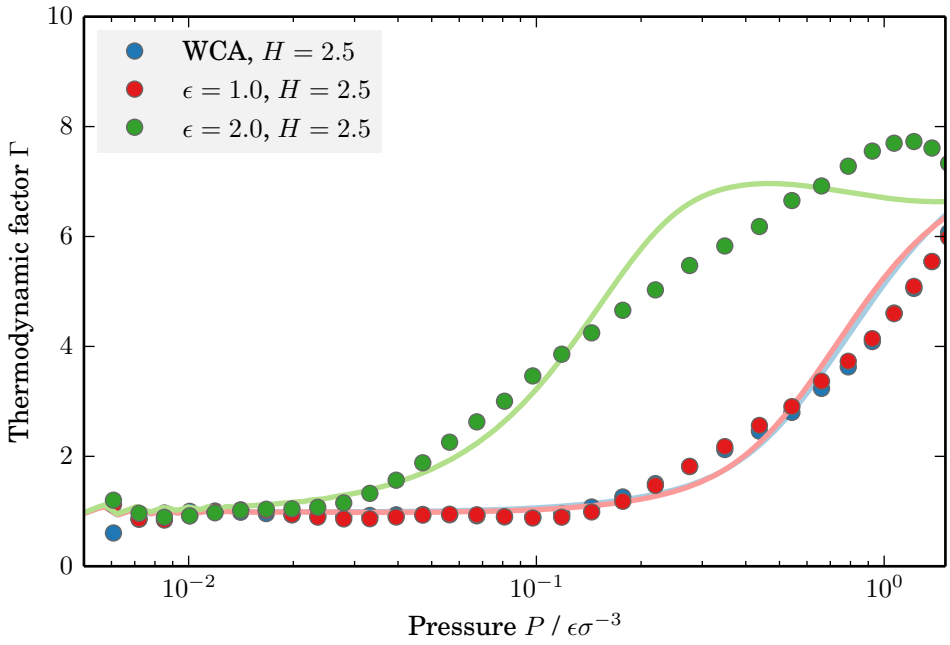

Figure 4.9: Thermodynamic factor of the confined Lennard-Jones fluid, inside the narrow pore with $H = 2.5$. The symbols denote the simulation data obtained by differentiating cubic splines and the solid lines represent the numerical differentiation of fitted curves for the narrow pore in Fig. 4.6.

sure are difficult to measure *in silico*. The difficulties stemming from limitations of the simulation approach are magnified by the fact that the thermodynamic factor is a derivative property and therefore particularly vulnerable to noisy data. Plots containing additional data of the thermodynamic factor are included in the appendix (Fig. A.4 and Fig. A.5), but the data is not presented here as it is not deemed reliable due to the complications at simulating higher densities.

4.3 Diffusion and particle mobility

4.3.1 Self-diffusion

Self-diffusion describes the diffusion of a single particle in an ensemble of identical particles. It is thus a measure for particle mobility. Dense fluids have frequent collisions and the MSD is a linearly correlated with time at longer time scales. While all real fluids should converge to a linear time progression for time $t \to \infty$ in theory, times

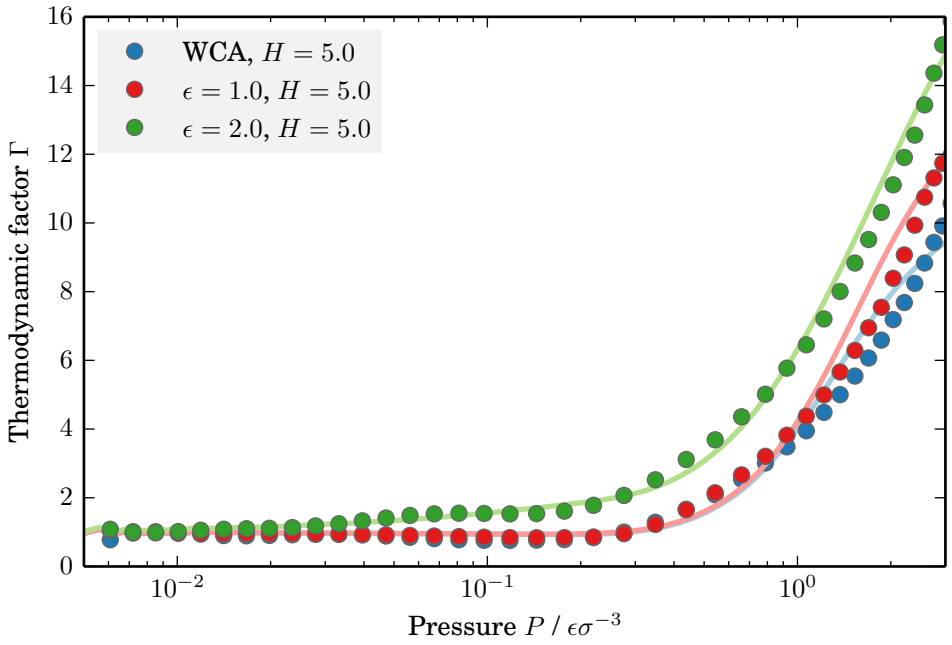

Figure 4.10: Thermodynamic factor of the confined Lennard-Jones fluid, inside the wide pore with $H = 5.0$. Lines and symbols as in Fig. 4.9, only referring to the wide pore fits of Fig. 4.7.

scales in the pico-second regime are sufficient to obtain linear scaling for simple dense liquids. According to the Einstein equation, the linearity of the MSD is proportional to the diffusion coefficient. In this work, this approach of determining diffusion coefficient from MSD curves was preferred over the integration of the VACF to determine diffusivity.

It is apparent from eq. (3.20) that the dimensionality of the system has an influence on the diffusion mechanism. For the bulk LJ fluid, diffusion is isotropic and all orthogonal directions contribute equally. Thus, $D_s = D_{\mathrm{s},xx} + D_{\mathrm{s},yy} + D_{\mathrm{s},zz}$. Here, the isotropic bulk self-diffusivity is therefore determined by observing the three-dimensional MSD ($d = 3$):

$$D_\mathrm{s} = \frac{1}{6} \lim_{t\to\infty} \frac{\mathrm{d}}{\mathrm{d}t} \left\langle \frac{1}{N_\mathrm{f}} \sum_{i=1}^{N_\mathrm{f}} |\mathbf{r}_i(t) - \mathbf{r}_i(0)|^2 \right\rangle \ . \tag{4.8}$$

An ensemble of 4000 LJ particles in a cubic simulation box of length 30σ was initiated from a hexagonally-close-packed lattice structure. During an equilibration of 50000 time steps, the system was thermostatted at a temperature of $T = 1.5$ with a Nosé-Hoover thermostat. The time step was chosen at 0.001. Subsequent EMD simulations, during which no thermostat was applied (NVE ensemble), were run for 5 million time steps and MSD were continuously calculated during the simulation. Every 1000000 time steps, a new origin was chosen for the calculation of the MSD and the five different MSD curves were averaged for increased accuracy. A series of simulations were performed for various densities at regular intervals between 0.01 and 0.9.

The obtained self-diffusion coefficient for the cut-and-shifted LJ fluid as a function of pressure is shown in Fig. 4.11, where the results are compared to a correlation for self-diffusion of the LJ fluid. The correlation for self-diffusion and density reads as follows (Silva and Liu, 2008):

$$D_\mathrm{s} = \alpha \left(\frac{\sqrt{T}}{\sigma^2_\mathrm{BLSM}} \right) \exp\left(\frac{\beta\rho}{(\gamma - \rho)} \right) \frac{\exp\left(\frac{\delta}{T}\right)}{\rho} \ , \tag{4.9}$$

where α, β, γ, and δ are fitted parameters and σ_BLSM is the Boltzmann radius (Silva and Liu, 2008), which can be expressed as:

$$\sigma_\mathrm{BLSM} = 2^{(1/6)} \left(1 + \omega\sqrt{T}\right)^{(1/6)} \ . \tag{4.10}$$

where ω is a also fitted parameter. The results show that self-diffusion exhibits a monotonic decline as pressure increases. In fact, the data in Fig. 4.11 is plotted on

α	β	γ	δ
0.2116	-0.75	1.2588	-0.27862
$\omega = 1.3229$			

Table 4.2: This table shows the fitted parameters of the self-diffusion correlation of the bulk LJ fluid.

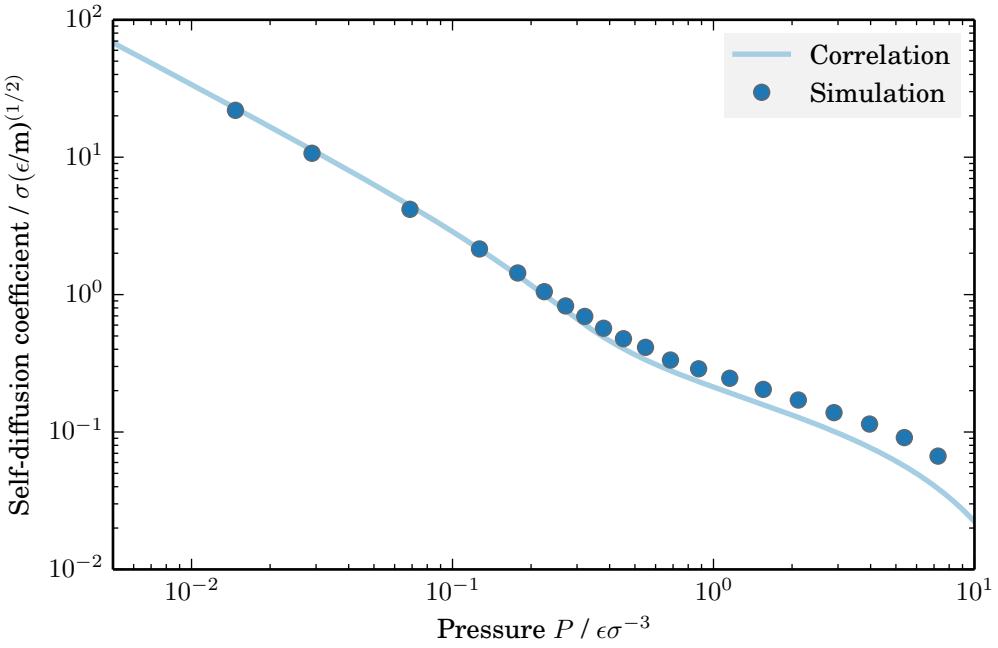

Figure 4.11: Self-diffusion coefficients at $T = 1.5$ as a function of pressure for the bulk Lennard-Jones fluid.

a logarithmic scale and self-diffusion decays exponentially as the system gets denser at increasing pressures.

In contrast to the self-diffusion of the bulk fluid, diffusion of the confined fluid is anisotropic. Although $D_{\mathrm{s},zz}$ can be defined mathematically and could in theory be a measure for particle mobility in the z direction, the fluid is confined in the z dimension by impermeable walls and no transport can occur in this direction. The definition of a diffusion in the z direction is therefore not meaningful from a physical point of view. The property of interest for the LJ fluid confined by a planar slit pore is therefore the in-plane diffusivity, $D_{\mathrm{s},xy}$. The in-plane diffusion process is characterised by two dimensions ($d = 2$) and the Einstein equation for the self-diffusion of the confined

fluid yields:

$$D_{\mathrm{s},xy} = \frac{1}{4} \lim_{t\to\infty} \frac{\mathrm{d}}{\mathrm{d}t} \left\langle \frac{1}{N_\mathrm{f}} \sum_{i=1}^{N_\mathrm{f}} \left[(x_i(t) - x_i(0))^2 + (y_i(t) - y_i(0))^2 \right] \right\rangle . \tag{4.11}$$

Self-diffusivities for the confined fluid were calculated for each of the slit pore variations described in section 4.2 at various pore loadings from 30 up to 310 particles per unit cell for the small pore, and 60 to 590 particles per unit cell for the wide pore. Based on the adsorption isotherms obtained in section 4.2, the pore loading can be related to an external pressure.

The results for self-diffusion of the confined LJ system inside the slit pore models of three different types of fluid-wall interactions as a function of external pressure can be seen in Fig. 4.12 and Fig. 4.13. For data regarding self-diffusivities as a function of pore loading per unit-cell, please refer to the appendix, Fig. A.6 and Fig. A.8. As expected, the self-diffusion of a confined fluid also declines monotonically with an increase in pressure, as it does for the bulk fluid. The data also shows the significance of fluid-wall interactions for transport properties. The difference between a repulsive wall and a strongly wetting wall with $\varepsilon_{\mathrm{fw}} = 2.0$ amounts to an order of magnitude, both for the narrow and wide pore system. It can also be seen in Fig. 4.12 and Fig. 4.13 that the differences are more significant in the gaseous regime. Given that repulsive walls can be expected to generate a higher degree of specular reflections for colliding gas molecules, the pronounced difference in self-diffusion for low-density fluids is likely to be found in the nature of fluid-wall collisions.

4.3.2 Collective diffusion

Self-diffusion as a measure for single-particle mobility has limited informative value with regards to effective mass transport properties. Self-diffusion will significantly decrease with an increase in fluid density, while the effective mass transport coefficient of the system, that is the mass transport as a result of a gradient in density, will be greatly increased by an increase in fluid density. Diffusion is an inherently collective property as the motion of molecules is directly correlated to the motion of the molecules surrounding it, both in the state of equilibrium as well as under non-equilibrium conditions.

However, despite the fact the determination of self-diffusion coefficients for pure-component systems in bulk is very common, a collective diffusion coefficient cannot be defined for a pure-component bulk fluid. To some extent, this comes down to a matter

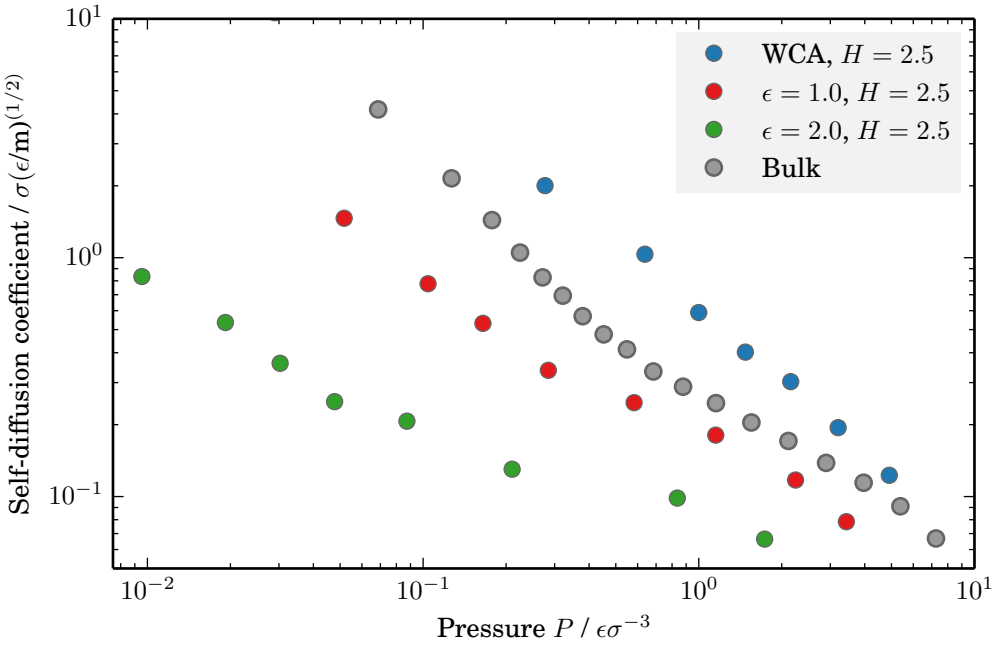

Figure 4.12: Self-diffusion coefficients of the confined Lennard-Jones fluid as a function of pressure for the narrow pore ($H = 2.5$). The bulk self-diffusivity as a function of pressure from Fig. 4.11 (Simulation data at $T = 1.5$) is plotted in grey.

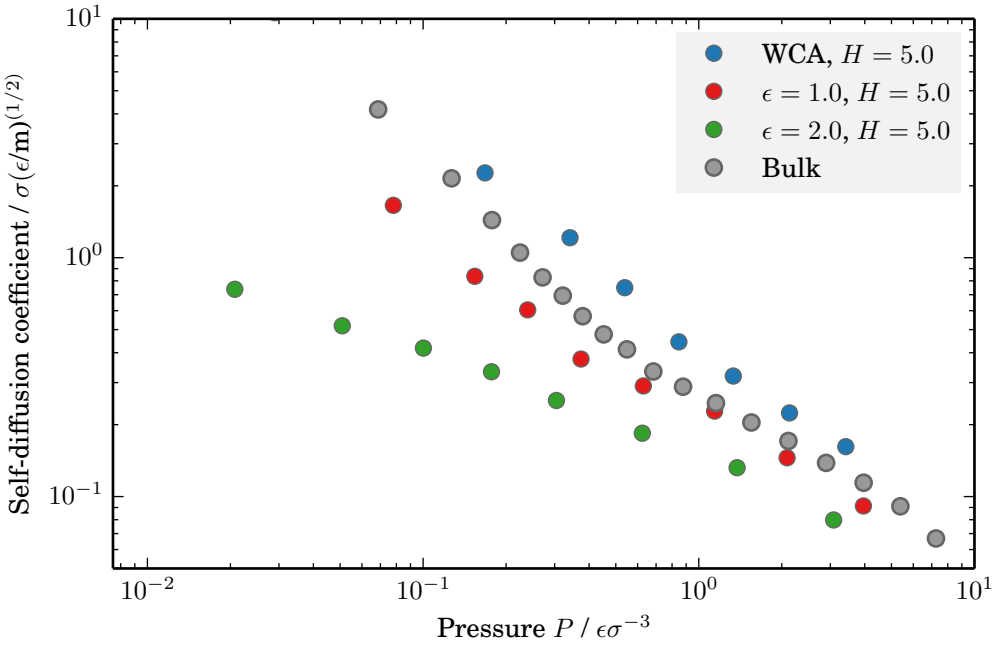

Figure 4.13: Self-diffusion coefficients of the confined Lennard-Jones fluid as a function of pressure for the wide pore ($H = 5.0$). As in Fig. 4.12, the bulk self-diffusivity is plotted in grey.

of definition, but it is physically fairly obvious that no net diffusive mass flux can occur in a pure bulk. While self-diffusion is related to the MSD of a single particle, collective diffusion is correlated to the MSD of all particles, that is the MSD of the centre-of-mass of the ensemble. A vantage point focused on molecular simulations underlines the lack of collective diffusivity for a pure fluid. From this point of view, the NVE ensemble conserves the linear momentum of the collection of particles. Thus, there are no fluctuations in the collective (centre-of-mass) velocity in a single-component (i.e. pure) bulk fluid and, unlike the MSD of individual particles, the collective MSD is always zero. For a pure fluid under confinement, however, the confining walls can be perceived as a second species and it is therefore possible to define a collective diffusion coefficient. Due to confinement, fluid and wall exchange momentum and the collective velocity of the fluid particles does fluctuate and the collective MSD is non-zero.

In the case of the planar slit pore, the in-plane diffusion is of interest and thus the expression for collective diffusivity, eq. (3.21), can be simplified to the two dimensional form:

$$D_{\mathrm{c},xy} = \frac{1}{4N_\mathrm{f}} \lim_{t\to\infty} \frac{\mathrm{d}}{\mathrm{d}t} \left\langle \left[\sum_{i=1}^{N_\mathrm{f}} x_i(t) - x_i(0) \right]^2 + \left[\sum_{i=1}^{N_\mathrm{f}} y_i(t) - y_i(0) \right]^2 \right\rangle \ . \tag{4.12}$$

It is important to note that in comparison to eq. (4.11), the summation over the ensemble takes precedence and thus the collective mean square displacement is observed. One could also express the collective diffusivity in term of the centre-of-mass displacement:

$$D_\mathrm{c} = \frac{1}{4N_\mathrm{f}^2} \lim_{t\to\infty} \frac{\mathrm{d}}{\mathrm{d}t} \left\langle \left[\mathbf{r}_\mathrm{COM}(t) - \mathbf{r}_\mathrm{COM}(0) \right]^2 \right\rangle \ , \tag{4.13}$$

where $\mathbf{r}_\mathrm{COM}$ denotes the position of the centre-of-mass of all fluid particles. Calculating self-diffusion coefficients is the standard approach to determine a system's transport properties. It is convenient to calculate and is clearly defined for a pure substance at equilibrium. It is important to keep in mind, however, that phenomenological transport coefficients, such as the transport diffusivity D_t, or the Maxwell-Stefan diffusivity D_MS are inherent to inhomogeneous and/or multicomponent systems. They only correspond to the self-diffusion coefficient in the special cases of infinite dilution (Reid et al., 1987).

Notwithstanding, collective diffusion coefficients are inherently difficult to determine for low-density states because the pore loading per unit cell is very low and extremely long simulations are required to overcome the low signal-to-noise ratio in this

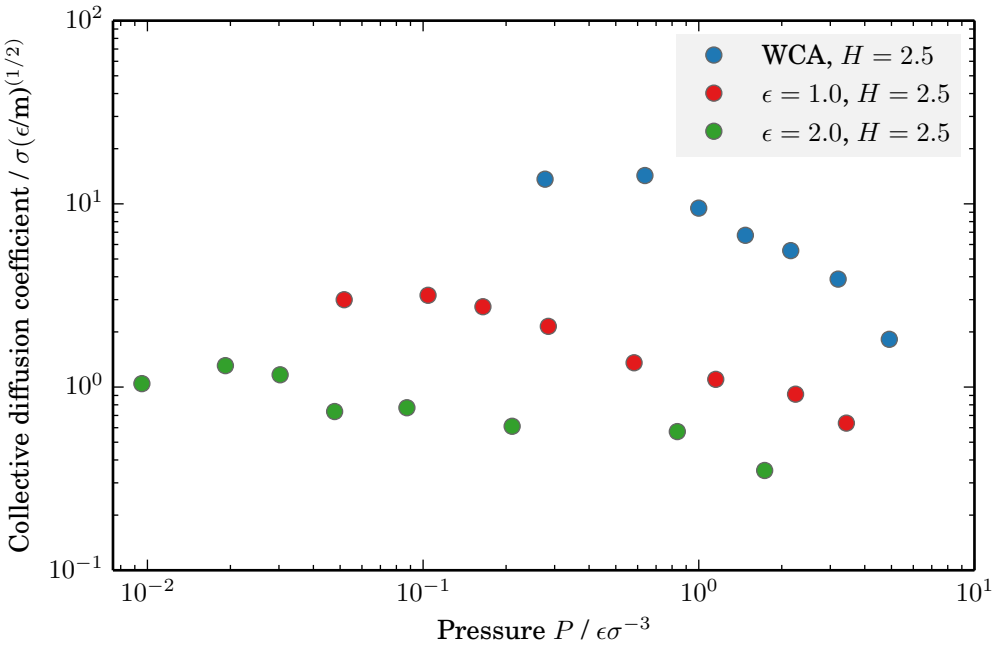

Figure 4.14: Collective diffusion coefficients of the confined Lennard-Jones fluid, inside the narrow pore with $H = 2.5$.

scenario. In this work, it was necessary to perform production runs for 50 million time steps after an equilibration of 50000 time steps. Such long simulation lengths are necessary due to the long time tail of collective correlation functions. Collective diffusivities as a function of external pressure for various slit pore models are shown in Fig. 4.14 ($H = 2.5$) and Fig. 4.15 ($H = 5.0$). Again, the simulations were performed at fixed pore loadings and the external pressure was determined from GCMD simulations, as was the case for the self-diffusion coefficients. The results for collective diffusion as a function of unit cell loading are given in the appendix (Fig. A.7 ($H = 2.5$) and Fig. A.9 ($H = 5.0$)). The results show that both self- and collective diffusivities generally decline as the pressure of the fluid increases and therefore the fluid gets denser. This highlights that they are measures for the mobility of the fluid but neglect thermodynamic influences on transport originating from the compressibility of the fluid. It is also important to note that self-diffusivity declines more rapidly than the collective diffusion coefficients, as is expected based on the treatment in section 3.2.2.

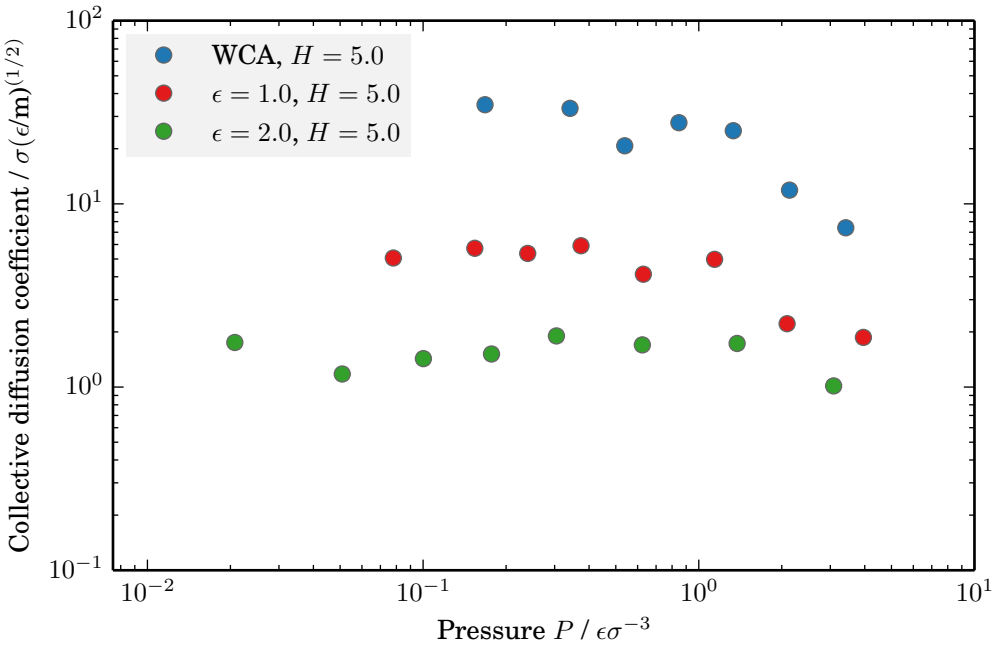

Figure 4.15: Collective diffusion coefficients of the confined Lennard-Jones fluid, inside the wide pore with $H = 5.0$.

4.3.3 Transport diffusion from NEMD

The above digression focuses on obtaining transport coefficients from EMD simulations. As outlined in section 3.3, NEMD simulations can be used to obtain effective diffusion coefficients directly by measuring the gradient in density in a system and the flux resulting from said perturbation. The slit pore system was also used here to study effective mass transport for the slit pore variations used for EMD simulations: one narrow and one wide slit pore with pore width $H = 2.5$ and $H = 5.0$, respectively, and the same three types of fluid-wall interactions. In order to create a system where density gradients can be maintained and measured confidently, the pores were surrounded by two regions on either side in which the bulk fluid is in contact with the pore rather than generating an infinite pore via periodic boundary conditions. This in turn makes the system similar to the model systems studied in section 3.3. The system was perturbed from its original state via an external field applied to the boundary as described in section 3.3. An equilibration run of 50000 time steps during which no external perturbation was applied were followed by another 100000 time step long simulation during which the external field was activated, allowing the system to reach a steady-state. Productions runs were then performed for 5 million time steps during

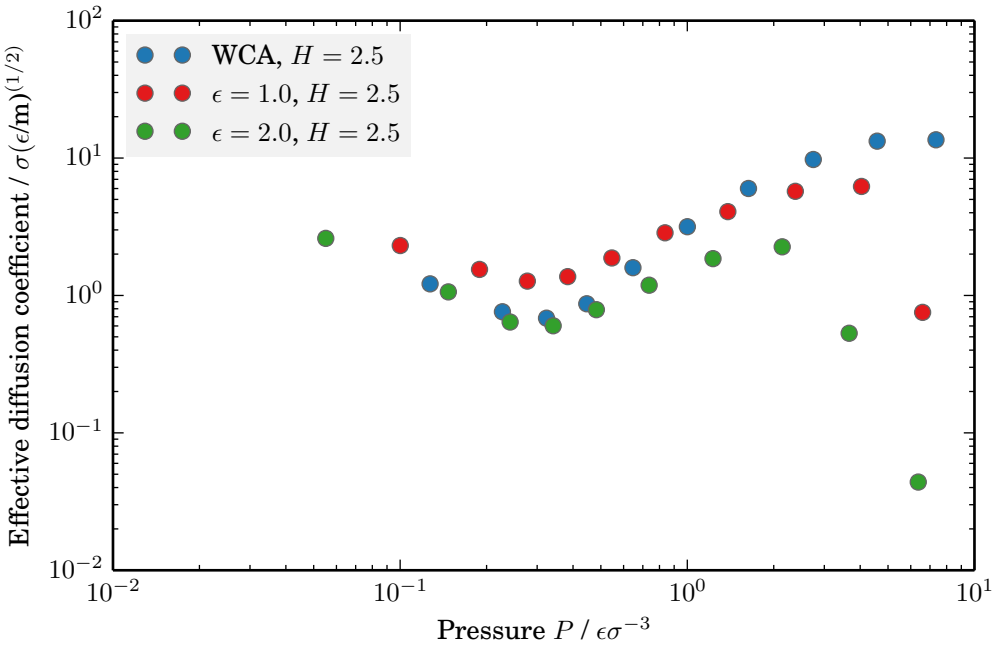

Figure 4.16: Effective diffusion coefficients of the confined Lennard-Jones fluid from NEMD simulations, inside the narrow pore with $H = 2.5$.

which the steady-state flux and density gradients were measured. Density gradient and steady-state molar flux, J, were calculated from the density and velocity distributions in the direction of flux. Although the simulation time of 5 million time steps in an order of magnitude lower than EMD simulations times for collective diffusivity calculations, a set of simulations with varying strengths of the perturbing external field were required. In this study, the magnitude of the external field was between 0.05 and $1.3\varepsilon/\sigma$.

As explained in section 3.3 of this work, effective diffusivities were calculated by extrapolating the results of a range of simulations with varying magnitude of external perturbation to the point of no perturbation (i.e. the zero force limit). This approach follows the notion of linear response theory and it counter-balances the problem that small perturbations result in a small signal, namely a smaller flux and density gradient. Large perturbations can divert the system too far from equilibrium.

A set of configurations of both narrow and wide pore were created with a variation of fluid particle loading. The number of fluid particles varied between 250 and 2500 fluid particles for the narrow pore (10 different values) and between 500 and 4000 particles for the wide pore (15 different values). The bulk regions are in direct contact

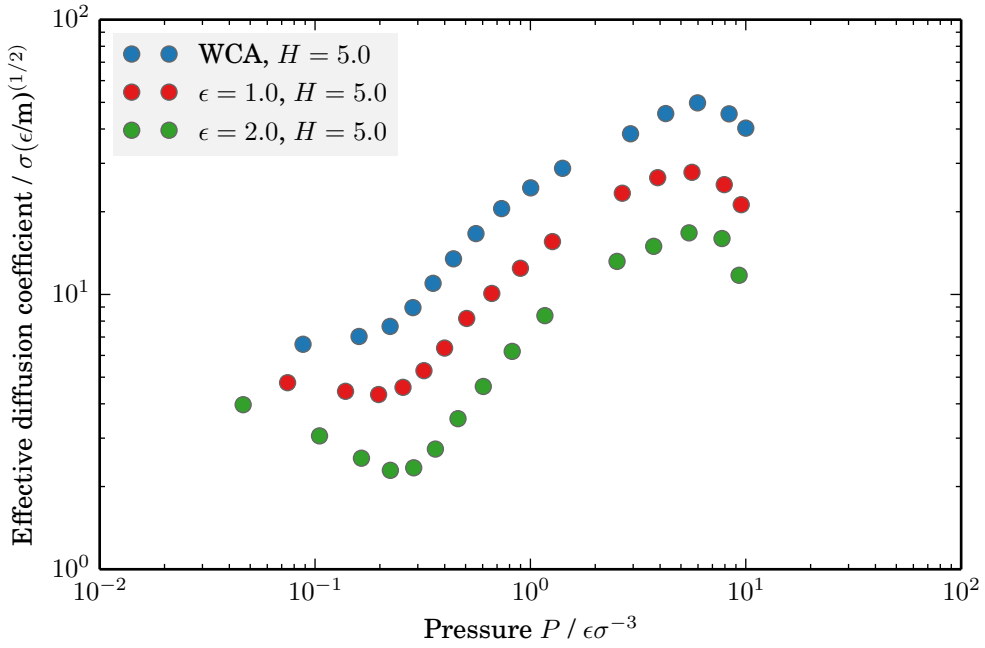

Figure 4.17: Effective diffusion coefficients of the confined Lennard-Jones fluid from NEMD simulations, inside the wide pore with $H = 5.0$.

with the fluid inside the pore and once the configurations were equilibrated, the bulk regions yield the bulk densities ($\bar{\rho}$). The respective bulk pressure was then determined from the equation of state data ($P(\bar{\rho})$), which was shown to represent the simulation data with great accuracy (see Fig. 4.4). The results for D_{eff} as a function of external bulk pressure for each of the variations of the narrow pore system are shown in Fig. 4.16, and for the wide pore in Fig. 4.17. The results are also tabulated in the appendix (Tables A.3 and A.5).

4.4 Comparison of transport models

The mainstream theories to describe and predict mass transport in microporous materials have been summarised in chapter 2 (section 2.2.2). Their respective advantages and drawbacks depend on many factors but for the simple case of a pure-component LJ fluid diffusing through a porous medium, the various transport theories are equivalent to the largest extent. Often there is a fundamental discrepancy in the assumed boundary conditions applying to fluid flow. As mentioned previously, the Knudsen model assumes diffusive reflections for fluid particles colliding with the pore wall.

Since the model is based on observations of gas flowing through micrometer sized glass cylinders (Knudsen, 1909), the assumption would be very accurate for a very low density fluid diffusing through large pores with rough walls. It is therefore applicable to predict dilute gas transport through large capillaries for which the mean free path of the gas molecules is large in comparison to the pore size (corresponding to a large Knudsen number). Although the Knudsen approach applies to cylindrical pores, it can be used for the slit pore model by regarding the pore width H rather the pore diameter d as the characteristic length scale for Knudsen flow, and thus the applicable Knudsen equation ((2.13)) is:

$$D_{\mathrm{K}} = \frac{H}{3}\sqrt{\frac{8k_{\mathrm{B}}T}{\pi m}} \,. \tag{4.14}$$

In terms of the model parameters that it takes into account, equation (4.14) considers only pore width. The Knudsen model is not capable of accounting for fluid-wall interactions or variations in fluid density explicitly. Although refined models of the Knudsen approach have been published, they are limited to adjusting the nature of wall collisions the Knudsen model is based on (Arya et al., 2003). For the two pore models of interest here, the Knudsen model yields $D_{\mathrm{K}} = 1.628\ \sigma(\epsilon/m)^{(1/2)}$ for the narrow pore $H = 2.5$, and $D_{\mathrm{K}} = 3.257\ \sigma(\epsilon/m)^{(1/2)}$ for $H = 5.0$. The values are expressed in reduced units with $k_{\mathrm{B}}T = 1.5$ and $m = 1.0$. Apart from the limitations regarding solid-fluid interactions, the Knudsen model is based on a geometrically clear and simple definition of pore width, which is not satisfied for a structured, molecular pore. Here it was assumed that the pore width H, which was employed in the Knudsen model, is simply the width between the first layers of wall molecules, which is erroneous especially for very small pores. For small structured pores, it is possible to determine an effective pore width based on the Knudsen model, but the availability of experimental or simulation data is required to do this.

The Hagen-Poiseuille equation, on the one hand, is based on a no-slip boundary condition, which arguably could also stem from very rough walls that generate a loss of momentum for the fluid in contact with the pore wall. On the other hand, the Hagen-Poiseuille equation is applicable to high-density fluids, where convective contributions, i.e. inertial effects, dominate mass transport. Moreover, the no-slip boundary condition, based on the idea of a rough and sticky pore wall, is appropriate for macroscopic pore dimensions. These assumptions fail on the molecular level. Porous structures with smooth molecular surfaces, such as carbon nanotubes, are clear counterexamples and while the definition of a pore wall is challenging itself,

the application of stick conditions is highly inaccurate for such surfaces. Moreover, the Hagen-Poiseuille equation, which derives from classical continuum fluid mechanics, applies to Newtonian fluids and is based on: a) a linear constitutive relationship between shear stress and velocity gradient and b) that the viscosity of the fluid does not depend on the shear rate. While this assumption would be valid for the LJ fluid, there are many cases in which non-Newtonian effects need to be considered.

The molar flux in a planar slit pore predicted from classical hydrodynamic theory can be expressed as:

$$J_x = \frac{\rho H^2}{32\eta}\left(\frac{\partial P}{\partial x}\right) , \tag{4.15}$$

where η denotes the dynamic viscosity of the fluid (and again H is the pore width and ρ is the molar density of the fluid). As in the case for pressure-driven gas flow described by Knudsen, the Hagen-Poiseuille equation observes pressure-driven fluid flow through a capillary and the transport coefficient is therefore a permeability (first term on the right hand side in eq. (4.15)), which needs to be related to a corresponding transport diffusivity via an equation of state as follows:

$$D_{\mathrm{HP}} = \frac{\rho H^2}{32\eta}\left(\frac{\partial P}{\partial \rho}\right) . \tag{4.16}$$

The Hagen-Poiseuille equation being based on continuum hydrodynamics, the fluid viscosity is a key property determining the characteristics of fluid flow inside the pore.

It will be assumed that the confined fluid will exhibit bulk viscosity, even though this assumption bears large potential for error. It allows a correlation for the viscosity being used for the prediction of Poiseuille flow in a slit pore (Galliéro et al., 2005). The authors state that the correlation adequately represents the reduced viscosity of the LJ fluid in gas, liquid, and supercritical states, for $0 \leq \rho \leq 1.275$ and $0.6 \leq T \leq 6$. The error is smaller than 10% for reduced densities up to 0.8. The correlation yields fluid viscosity from a purely temperature-dependent part and a temperature and density-dependent part: $\eta(T,\rho) = \eta_0(T) + \Delta\eta(T,\rho)$. It is

$$\eta_0 = a_0 \frac{(T^*)^{1/2}}{\Omega_{\mathrm{v}}} A_{\mathrm{c}} , \tag{4.17}$$

where Ω_{v} denotes the Enskog collision integral (which derives from kinetic theory (Reid et al., 1987)), and A_{c} is a correction factor (equal to 1 for the LJ fluid or 0.95 for methane).

$a_0 = 0.17629$					
b_1	b_2	b_3	b_4	b_5	b_6
0.062692	4.09557	8.743269 $\times 10^{-6}$	11.12492	2.542477 $\times 10^{-6}$	14.863984
ω_1	ω_2	ω_3	ω_4	ω_5	ω_6
1.16145	0.14874	0.52487	0.77320	2.16178	2.43787

Table 4.3: Coefficients of the viscosity correlation for the LJ fluid (Galliéro et al., 2005).

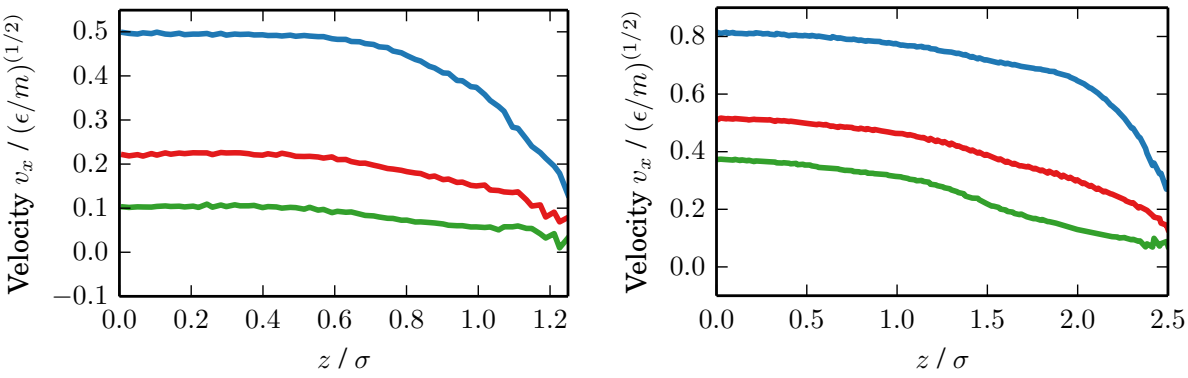

(a) $H = 2.5$ **(b)** $H = 5.0$

Figure 4.18: Velocity profiles inside a) the narrow pore at a loading of 1750 particles which corresponds to a bulk density between 0.61 and 0.66 ($P = 1.23 - 1.63$), depending on solid-fluid interactions, and b) the wide pore at a loading of 3000 particles which corresponds to a bulk density between 0.73 and 0.75 ($P = 2.52 - 2.92$). The colours are the same as in Fig. 4.8 (blue- WCA; red - $\epsilon = 1.0$; green - $\epsilon = 2.0$).

$$\Omega_v = \omega_1 T^{-\omega_2} + \omega_3 \exp(-\omega_4 T) + \omega_5 \exp(-\omega_6 T) \tag{4.18}$$

In addition, the correlation for the residual viscosity is given as:

$$\Delta\eta = b_1(\exp(b_2\rho) - 1) - b_3(\exp(b_4\rho) - 1) + \frac{b_5}{T^2}(\exp(b_6\rho) - 1)\ . \tag{4.19}$$

A further refinement with respect to the solid-fluid interaction (Dusty-Gas Model (Krishna and Wesselingh, 1997)), wall collisions (Oscillator model (Bhatia, 2010)) or non-uniform density distribution inside the confining pore (Local area density model

(Bitsanis et al., 1988)) are possible. While these refinements strive to incorporate solid-fluid interactions, their success is mostly limited to extreme conditions, such as the low-pressure limit. The velocity profiles shown in Fig. 4.18 show the influence of solid-fluid interactions and the slip flow conditions inside the smooth planar pore. The profiles highlight how significantly the mobility of the adsorbed layer can be influenced in the case of a strongly wetting wall. It is important to remember that is difficult to define an unambiguous solid boundary and calculating slip-lengths from the given profiles is a non-trivial task. By assigning a hard shell around the wall particles at their van-der-Waals radii and averaging the position of the corrugated wall, a slip length can be calculated by fitting a parabolic velocity profile to the velocity profile and extrapolating beyond the boundary. Since Knudsen and no-slip Hagen-Poiseuille are the most commonly applied theories to predict porous mass transport, the present comparison will not go beyond these two models.

Figures 4.19 and 4.20 show an extensive comparison between the different routes to obtain transport coefficients, namely predictions of the Knudsen (dashed line) and Hagen-Poiseuille equations (solid line), EMD simulations results based on the Darken model (empty circles) as well as effective transport diffusion coefficients obtained from NEMD simulations (filled circles). In order to obtain transport diffusivities based on the Darken model, collective diffusion coefficients were multiplied by the thermodynamic factor at the respective pressure ($D_{\mathrm{t}}^{\mathrm{Darken}} = D_c\Gamma$, refer to Fig. 4.9 and 4.10 and sections 2.3 and 3.2.2 for details). The tabulated results are also given in the appendix (Tables A.1 and A.2). The Knudsen approach to pressure-driven gas transport ($J = -D_{\mathrm{K}}/k_{\mathrm{B}}T \ \mathrm{d}P/\mathrm{d}x$) applies to the low-pressure limit, where the thermodynamic properties of gases can be approximated by the ideal gas law ($\rho = P/k_{\mathrm{B}}T$), and thus the thermodynamic factor is 1. Since the Knudsen approach does not incorporate a density/pressure dependence, Knudsen diffusivities are only comparable to effective transport diffusion coefficients at low pressures. Therefore, the dashed line indicating the Knudsen prediction is a constant.

It is evident from Fig. 4.19 and 4.20 that the Hagen-Poiseuille model rests on inertial effects dominating transport. At lower pressures, the fluid flow departs the hydrodynamic regime, where it considerably underestimates transport. Unrelated to this failure at the low pressure regime, there is a consistent underprediction of effective transport diffusion coefficients by the Hagen-Poiseuille equation. This is likely due to the assumption of a no-slip condition. The introduction of a slip length would add another parameter to the prediction model, which is already based on a large number

of parameters for viscosity correlation and equation of state.

Figures 4.19 and 4.20 also shows transport diffusion coefficients obtained from boundary-driven NEMD simulations in comparison to transport diffusivities based on the Darken model. The results from NEMD simulations appear considerably more consistent than EMD simulation results. Comparing the narrow and wide pore system, however, the EMD and NEMD data show that simulations for wider pores are more reliable than more narrow pores. Also, it is apparent that NEMD simulations are particularly useful for the transition regime. NEMD simulations with very low pore loading are very difficult and do not yield satisfying results because the net molar flux is very small and most of the computational effort is spent on simulating the movement of wall particles. On the other end of the spectrum, NEMD simulations are challenging for very dense fluids because the external perturbation can have spurious effects such as introduce freezing inside the pore (Radhakrishnan et al., 2002), which results in a collapse in fluid transport. It is likely that a solid-like state was induced in the case of the narrow, attractive pores at high pressures, which would explain the pronounced decrease in the effective diffusivity in Fig. 4.19.

4.5 Conclusions

This chapter shows a comprehensive comparison between various routes to obtain the transport diffusion coefficient of confined fluids in a planar slit pore. Apart from two different sizes of the pore and three different variations of solid-fluid interactions, studying the effects of pore loading resulted in very large number of simulations to be performed in different ensembles (a series of GCMD simulations to obtain isotherms, EMD simulations to obtain self- and collective diffusion coefficients, and NEMD simulations for effective diffusion coefficients.) The obtained data set allows for a detailed analysis of each methodology and a comparison to alternative theoretical methods to predict mass transfer in confinement. The Knudsen approach and Hagen-Poiseuille equation are severely limited with respect to incorporating the full molecular character of nano-confined systems and do not account for differences in solid-fluid interactions, but for limiting cases, such as the low density limit, or larger pore sizes, they provide quick semi-quantitative predictions. With respect to performing NEMD simulation to obtain transport diffusion coefficients, it must be noted that the simulations are ideally suitable for the transition regime between the Knudsen regime and the dense Newtonian fluid, because the approach can be challenging and suffers from in-

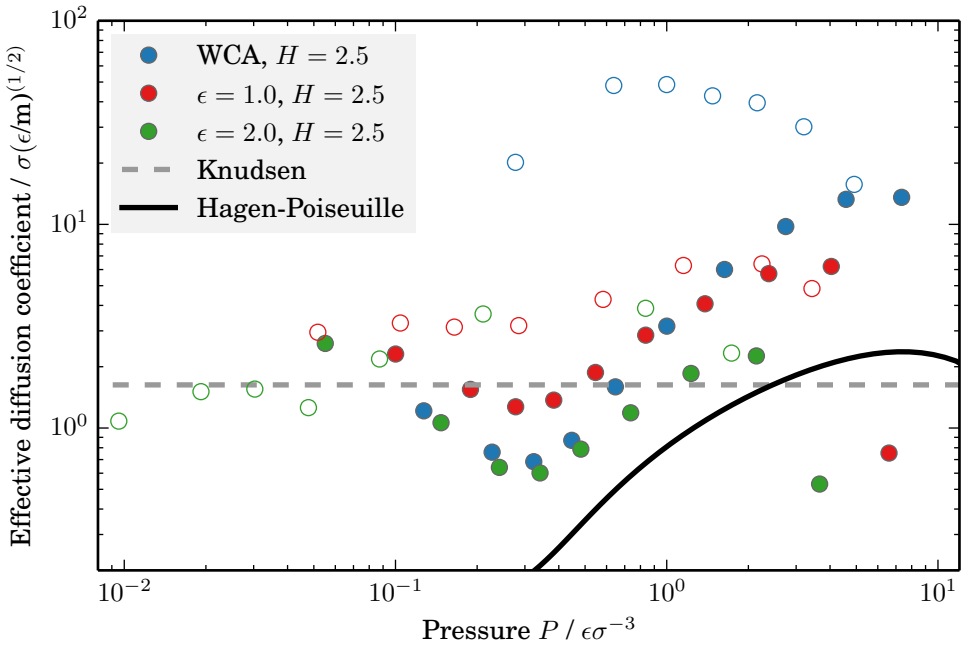

Figure 4.19: Predictions of transport coefficients from NEMD simulations (filled circles) inside the narrow pore with $H = 2.5$, in comparison to EMD simulations results based on the Darken model (empty circles), as well as predictions of the Knudsen model (dashed line) and the Hagen-Poiseuille equation (solid line) based on density and viscosity correlations for the LJ fluid (Johnson et al., 1993; Galliéro et al., 2005).

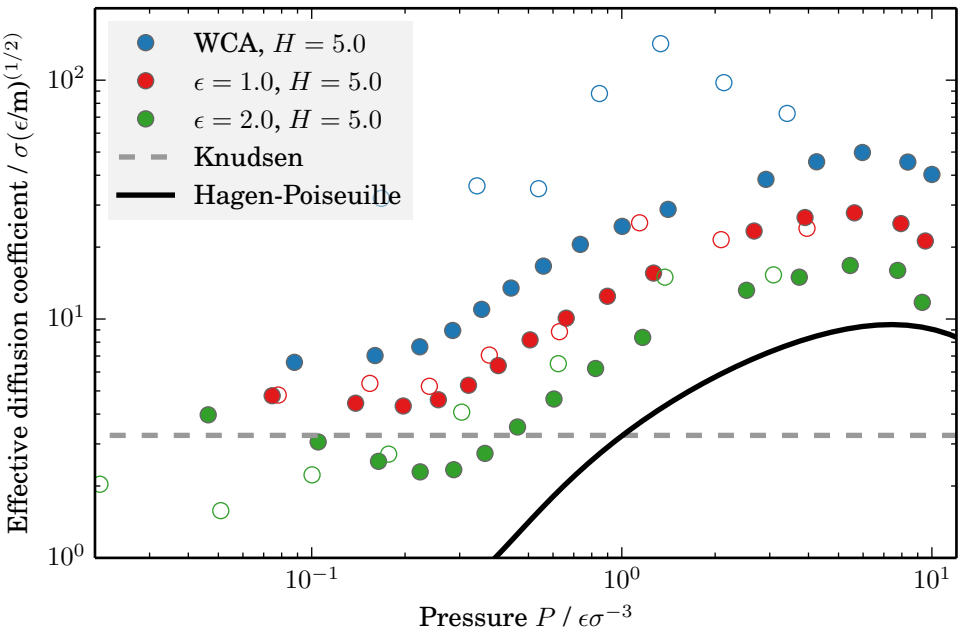

Figure 4.20: Predictions of transport coefficients from NEMD and EMD simulations and Knudsen and Hagen-Poiseuille equations inside the wide pore with $H = 5.0$, depictions as in Fig. 4.19.

accuracies for extreme scenarios. While GCMD simulations for adsorption properties paired with EMD simulations for obtaining diffusion coefficients is a common route to obtain transport diffusion coefficients, the complications in calculating collective diffusivities, in particular the limited statistical accuracy, poses a severe limitation. Nonetheless, it needs to be pointed out that NEMD simulations still require a reasonable amount of computational power. Simulations are carried out at different values for the external field and therefore the number of performed simulations adds up. Even if a long EMD simulation (50 million time steps) is required to obtain reasonable results for collective diffusion coefficients, an array of $5 - 10$ NEMD simulation at 5 million time steps each adds up to a similar computational load.

CHAPTER

FIVE

MODELLING OF GAS PERMEATION THROUGH PIM-1

Cualquier cosa que puedas imaginar es real.

Pablo Ruiz Picasso (1881-1973)

In the previous chapters, the investigation had a focus on well defined model systems through which fundamental mechanisms can be studied and the comparison to theoretical procedures are possible. In the following chapter, the potential of the boundary-driven NEMD approach is presented for a realistic system with a direct link to a practical engineering application, namely the permeation of penetrant gases through a microporous polymer, which is a problem of interest in membrane science and in the development of novel materials for gas separation purposes.

5.1 Introduction

The quest for improvements in the efficiency of gas separation membrane materials have spawned interdisciplinary research efforts targeted at searching for novel materials that deliver improved performance with a lower economic and environmental footprint (Koros and Mahajan, 2000; Baker, 2002; Bernardo et al., 2009). Pressure-driven gas separation, through versatile and easily manufactured polymeric membranes with high permeation and selectivity, are of particular interest and highly sought-after for fulfilling those purposes (Brunetti et al., 2010; Budd and McKeown, 2010).

Separating gases through a selective polymer membrane requires the gases to exhibit different rates of permeation through the polymer material. In order to find effective strategies to identify the individual parameters affecting permeability, it is

important to reach a detailed understanding of permeation mechanisms in porous polymers. Differences in permeability stem from variations in sorption and diffusion of gases in the polymer, which in turn are brought about by variations in polymer chemistry, microstructure or pore topology.

Molecular simulations have been instructive in investigating transport properties in structured molecular materials such as zeolites (Krishna, 2009), MOFs (Keskin and Sholl, 2009), and carbon structures (Lim et al., 2010). Equilibrium Molecular Dynamics is the most proliferated method to perform simulations of transport properties on the molecular scale since the movement of molecules, determined by intermolecular forces, is simulated explicitly. The usage of alternative techniques, such as Transition State Theory (TST) and kinetic Monte Carlo (Abouelnasr and Smit, 2012), have also been published in the literature. There have been several studies about calculating permeation in glassy polymers through simulation (Neyertz and Brown, 2013; Hofmann et al., 2000; Yampolskii, 2012; Müller-Plathe, 1994). Of relevance to this work are simulations of high free volume polymers such as PIM-1 (Fang et al., 2010, 2011; Heuchel et al., 2008; Chang et al., 2013). Solubility is usually determined from an adsorption isotherm obtained from a Grand Canonical Monte Carlo (GCMC) simulation, where the periodic image of the bulk polymer is in virtual contact with a reservoir of the gas of interest. Diffusivity in turn is determined from the self-diffusion coefficient of the gas inside the polymer, calculated from the mean square displacement of the gas molecules captured by the trajectories of an MD simulation. Usually, despite equilibrium and transport properties both being obtainable from MD simulations, the two key properties for gas separation membranes, solubility and diffusivity, are not simultaneously calculated. The solution-diffusion model, which describes permeation as a sequential process of adsorption, diffusion and desorption, is then used to estimate permeabilities.

There are significant shortcomings to the above mentioned approach. Firstly, self-diffusion is an approximation for transport diffusion, which is only exact at the zero pressure limit, thus at infinitely low gas uptake. Secondly, the solution-diffusion model applies to non-porous polymers which may exhibit a pore hopping mechanism for diffusing gases, a model incompatible with standard methodologies for calculating diffusivities from molecular simulation. Random walks, due to frequent ambidirectional collisions leading to Brownian motion, are the basis for determining diffusivities from the time derivative of the mean square displacement, also known as the Einstein equation. In this scenario, the mean square displacement (MSD) of the

molecules is linearly correlated with time: MSD$(t) \sim t$ (Gubbins et al., 2011). For amorphous polymers, anomalous diffusion, especially at short time scales under 5 ns, is observed (Müller-Plathe et al., 1992; Müller-Plathe, 1994). Similar to the diffusion inside confined spaces, such as single-file diffusion inside a cylindrical pore, the mean square displacement does not show a linear progression with respect to time, the diffusion is in fact slower. One may express the MSD as a power law, MSD$(t) \sim t^{\gamma}$, with the exponent γ being equal to one for a linear relationship. In the case of single-file diffusion, the exponent would be 0.5. The diffusion mechanism in microporous polymers is a combination of random unconstrained diffusion and strongly directional confined motion, leading to an exponent between 0.5 and 1. For very long time scales, the diffusion mechanism approaches random Einstein diffusion, but depending upon the penetrant gas, this can require simulation times of considerably more than 20 ns. The key challenge for MD simulations is to reach time scales long enough to observe Einstein diffusion and obtain reliable diffusion coefficients from the time-dependence of the MSD. Molecular simulation studies of gas diffusion in glassy polymers indicate that it is very challenging to unambiguously distinguish between diffusion mechanisms (Neyertz and Brown, 2009). The combination of these uncertainties, linked to the sometimes inappropriate invokement of the solution diffusion model lead to large errors (Fang et al., 2010, 2011; Chang et al., 2013) and overprediction of permeabilities. Alternatively, modelling of small molecule diffusion processes in high free volume polymers has been performed with techniques based on transition state theory (Hofmann et al., 2000; Heuchel et al., 2008), but the approach does not yet account for the internal flexibility of the polymer facilitating transport. Recently, an efficient screening of microporous polymer permeability using Monte Carlo solubility simulations in combination with empirical calculations of diffusion coefficients has proven useful for hypothetical PIMs (Hart and Colina, 2014).

In an effort to overcome some of these shortcomings, the present study of gas transport in microporous polymers implements the boundary-driven NEMD methodology in which the imposed external field creates a gradient in density, which in turn corresponds to a pressure gradient between the bulk gas phases, corresponding to permeate and retentate. As previously described in chapter 3, the external field is applied at the boundary and the thermostat is applied only to the solid. In the following, the methodology to set up the molecular model and its characteristics are outlined, followed by a discussion on developing the non-equilibrium simulation scheme. The simulation results presented thereafter cover the essential gas separation properties such as

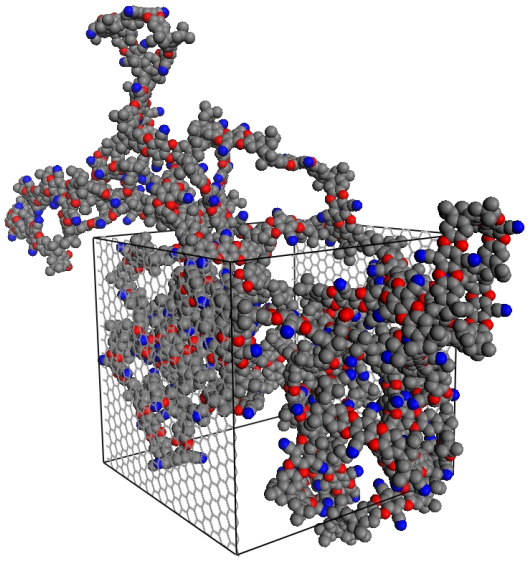

Figure 5.1: The final polymerised structure of the thin-slice PIM-1 simulation box, PIM-1(2D). The polymer is polymerised and periodic in the y and z dimensions, with the x dimension being capped by fluid-transparent rigid walls. The polymer is illustrated in unwrapped coordinates; however, periodic boundary conditions were used, with the wrapped coordinates sample shown in Figure 5.3.

permeability and gas uptake, and inquire into the transport mechanism of penetrant gases in PIM-1.

5.1.1 Molecular modelling

The porous material representing the polymer membrane is constructed by placing polymer slice in contact with bulk gas on either side, which exhibit different pressures during the NEMD simulations due to the external field applied, driving the transport of gas through the polymer. An atomistically thin polymer layer subject to gas adsorption will most likely swell. Furthermore, ultra-thin polymer membranes will exhibit an enhanced molecule mobility at the free surfaces with significant changes in conformation. In a finite-size simulation box, modelling this behaviour will require excessively large system sizes with no guarantee of accuracy. While one could study a "frozen" polymer configuration, the need to consider the flexibility and possible rearrangement of the polymer matrix is recognised in this study. Thus, as a compromise of limiting the displacement of the polymer, artificial walls are placed along the yz plane on each side of the polymer facing the gaseous bulk (Fig. 5.1). These walls are transparent to

sample	ρ_{sim} $(\mathrm{g\ cm^{-3}})$	f %	$\mathrm{SA_{geo}}$ $(\mathrm{m^2 g^{-1}})$	φ $(\mathrm{cm^3 g^{-1}})$	Ref.
PIM-1	0.93(0.02)	24.3(1.3)	595(85)	0.448(0.019)	(Hart et al., 2013a)
PIM-1(2D)	0.916	25.8	530	0.469	this work

Table 5.1: Porosity of the PIM-1 simulated samples

the fluid and allow for gases to permeate. They also ensure that the polymer slice will retain its bulk properties throughout the simulation on average.

Force fields

The force fields used to simulate the molecular mechanics of the polymer and gas models were taken from available transferable force fields, which model the structural and adsorptive properties of PIM-1 with quantitative accuracy (Larsen et al., 2011; Hart et al., 2013a). The polymer is described by means of a united-atom representation to facilitate computational efficiency with non-bonded interaction parameters taken from the Transferable Potential for Phase Equilibria (TraPPE-UA) (Rai and Siepmann, 2007; Martin and Siepmann, 1998; Wick et al., 2005; Lee et al., 2005). To model the flexibility and motion of polymer chains, bonded interaction parameters were taken from the Generalized Amber Force Field (GAFF) (Wang et al., 2004). All polymer force field parameters of PIM-1, including atomic partial charges, are given in detail by Larsen et al. (2011). Available models for Helium (Martin and Siepmann, 1997) and a flexible model for CO_2 (Potoff and Siepmann, 2001) were used, which are based on LJ sites with point charges in the case of carbon dioxide. As the presence of the bulk regions make the system inhomogeneous, the periodicity required to account for long-range interaction is not given and thus NEMD simulations are run without Ewalds summations for the electrostatic interactions (Frenkel and Smit, 2001). Instead, Coulombic interactions are cut off at 15 Å.

Structure Generation

In order to construct an atomistic sample of a slice of an amorphous polymer, the predictive virtual synthesis software, *Polymatic* (Abbott, 2013; Abbott et al., 2013), in conjunction with the LAMMPS simulation package (Plimpton, 1995) (Release date: 25

July 2012) was used. Polymatic has recently been used to simulate a wide variety of polymeric materials including porous and nonporous glassy polymers (Hart et al., 2013b; Abbott et al., 2013; Hart et al., 2013a, and references therein). One of the benefits of using this procedure is the versatility in designing an environment in which the sample is polymerised. To construct the initial simulation sample, a 3D periodic cell of 4.44 nm in edge length is packed with PIM-1 monomers. Rigid walls are placed at the periodic boundaries of the x direction of the sample, which resulted in a 3D simulation box of PIM-1 monomers with the restriction that no monomer can penetrate the x boundary. To facilitate polymerisation, high temperature MD simulations in the canonical ensemble are run at 2000 K in between bonding steps. During the MD simulations, the walls are held frozen. With the aid of artificial charges ($\pm 0.3e$) on bonding capable chain ends, the polymerisation proceeds until no more bonds can be made within a reasonable time frame. In this particular scenario, 250 cycles of 5 ps MD simulations were emplyed. The result is a polymerised PIM-1 sample that resembles a 4.5 nm thin slice of polymer, as the polymer is not periodic in the x dimension. The final simulation configuration is shown in Figure 5.1.

5.1.2 Model characterisation

The physical properties of the polymer sample were characterised by means of density, fractional free volume, geometric surface area, and pore size distribution. To calculate these propeties, the rigid walls were removed, and the box dimensions were corrected to account only for space occupied by the polymer ($a = b = 4.44$ nm, $c = 4.53$ nm). The density (ρ_{sim}) was calculated as the mass of the polymer, m, divided by the total volume of the simulation cell (including all pore volume). The fractional free volume (f) was calculated as $f = 1 - 1.3(V_{\mathrm{vdW}}/V_{\mathrm{sp}})$, where V_{vdW} is the volume occupied by the polymer in the simulation sample, and V_{sp} is the specific volume calculated as the reciprocal of the density ($1/\rho_{\mathrm{sim}}$). V_{vdW} was calculated by subtracting the void volume (φ) from the V_{sp}. As the molecular model is built on the basis of soft spheres, the volumes and areas occupied by the polymer are ill-defined. One can consider V_{vdW} to be defined at the point where the intermolecular potential is null, i.e. by employing a probe molecule of 0.0 nm and accounting for the regions of space where the probe experiences a repulsive interaction. Similarly, the geometric surface area ($\mathrm{SA}_{\mathrm{geo}}$) was calculated as the amount of surface area outlined by the centre of a N_2-sized probe molecule, $d_{\mathrm{N_2}} = 3.681$ Å. The pore size distribution (PSD) is the numerical derivative of the cumulative pore volume function $V(r)$ with respect to probe size, r. All porosity

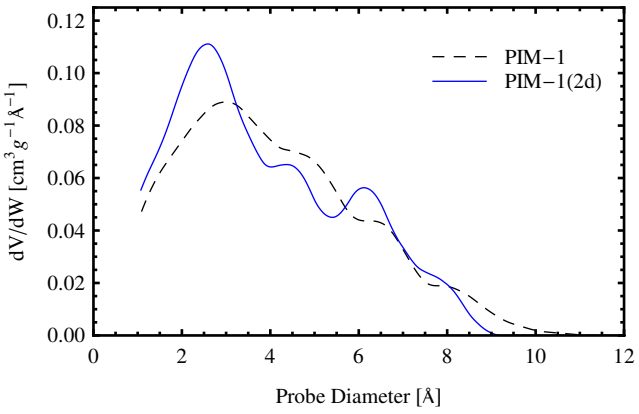

Figure 5.2: The pore size distribution (PSD) of the 2-dimensional thin film model of PIM-1, PIM-1(2D) (solid), compared with an average of five periodic simulation samples from Ref. (Hart et al., 2013c) (dashed).

characterisations were calculated using the Pore Blazer code (Sarkisov and Harrison, 2011).

Molecular simulations of PIM-1, studying the same force field model used here, have shown to resemble the physical polymer in properties such as BET surface area, adsorption isotherms, enthalpies of adsorption, gas selectivities, and wide angle X-ray scattering experimental data (Hart et al., 2013c,b; Abbott et al., 2013; Hart et al., 2013a; Hart and Colina, 2014). Moreover, the results of the structural characterisation of the PIM-1 (2D) model is in excellent agreement with the average values of the previous 3D periodic PIM-1 simulated sample density, fractional free volume, geometric surface area, and void volume, as shown in Table 5.1. In addition, the pore size distribution profile of the polymer slice model, PIM-1 (2D), and 3D simulation samples are consistent (see Fig. 5.2). As such, it is reasonable to conclude that the PIM-1 (2D) model will exhibit similar gas permeability characteristics to a similarly sized element of a bulk PIM-1 membrane, as a result of the similar pore structure characteristics.

5.1.3 NEMD simulations

The walls confining the polymer in the x direction are made permeable to gas molecules and two regions filled with gas molecules are constructed next to the polymer sample, creating an elongated simulation box in the x direction three times the size as the original polymer sample. A preliminary MD equilibration is performed to allow the gases adsorb onto the polymer. As expected, inert helium exhibits modest adsorp-

tion, while carbon dioxide adsorbed strongly. As gases saturate the polymer during equilibration, the gas uptake, which depends on the bulk pressure, was measured directly by integrating the gas density distribution:

$$c(P) = \frac{1}{V_{\mathrm{P}}} \int \rho(x) \mathrm{d}x \tag{5.1}$$

where ρ denotes the gas density and V_{P} denotes the volume of the polymer, which will specifically depend on the integration boundaries multiplied by the height and depth of the simulation box (in z and y directions respectively). The gas regions initially contained 56 and 330 molecules for helium and carbon dioxide, respectively, such that the bulk gas pressure at equilibrium was in the order of 10 bar.

An external field applied in a thin slab (0.3 nm thickness) at the boundary of the simulation box perturbs the system from its equilibrium state. The field acts like an acceleration in the z direction on the gas particles at the boundary and creates regions of higher and lower bulk density on opposite sides of the polymer slice. The resulting difference in pressure drives molecules to permeate through the polymer matrix. The steady state response of the system is observed, where gas flux and pressure difference between the two bulk regions are averaged over time. Permeability, κ_{P}, can then be determined by invoking Darcy's law:

$$J = \kappa_{\mathrm{P}} \frac{\Delta P}{\Delta x} \ . \tag{5.2}$$

The fixed walls keep the polymer in place in the direction of transport (x direction). In order to prevent perpendicular drifting of the polymer within the confining sheets, six carbon atoms of the entire polymeric sample (from central spiro-bisindane groups) were tethered to their initial positions with a spring constant of $k_s = 5$ kcal/(mol Å^2). During the extent of the simulation the polymer is allowed to move, subject to the tethering of these six sites, i.e. a flexible structure is modelled rather than a static one. Notwithstanding, due to the inherent rigidity of the PIM, the initial conformation is not seen to change significantly nor swell.

The external field performs work on the gas molecules, which must dissipate as heat to maintain isothermal conditions and hence needs to be removed from the system in order to maintain a steady state response. To this end, the Nosé-Hoover thermostat at 298 K was used for the polymer while the gas was left without a thermostat and left to release the additional energy through interactions with the polymer. This protocol is followed in order to prevent unphysical perturbations arising from thermostatting to be introduced during the transport process. It is important here to balance the

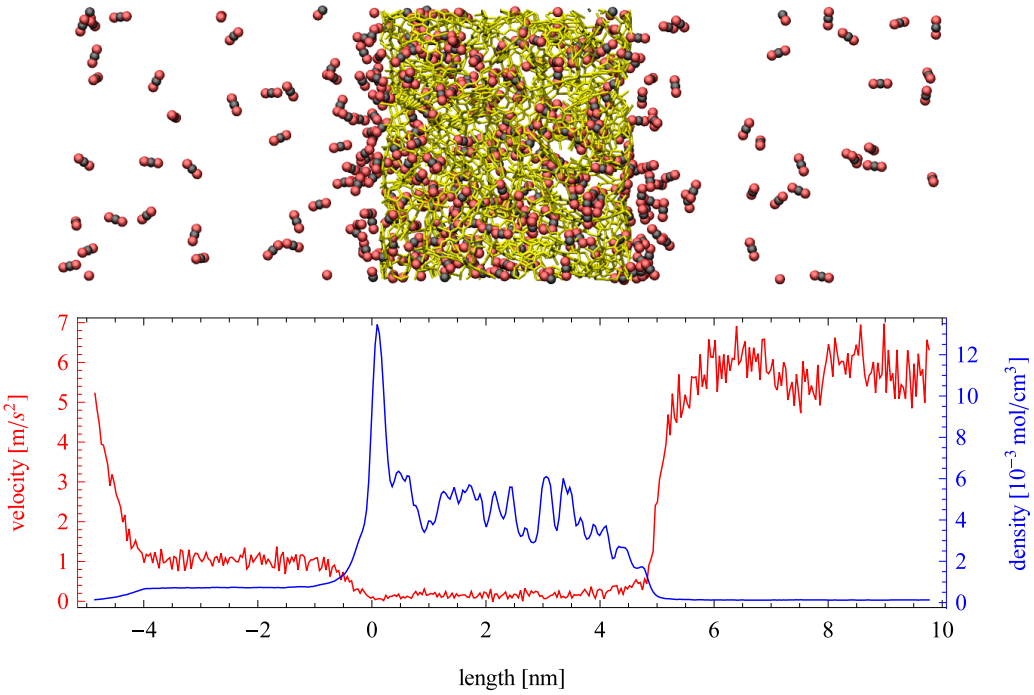

Figure 5.3: (top) Snapshot of an instantaneous configuration of the simulation cell. Periodic boundary conditions are applied in all directions and an external force applied to the fluid molecules in the left boundary. Carbon dioxide molecules are depicted by black and red while a stick representation of a slab of PIM-1 is shown in yellow. (bottom) Average velocity profile in the direction of transport (red) and fluid density profile (blue) across the simulation cell. Density within the porous region is referred to the total volume including the polymer.

magnitude of the external field with the system's ability to release heat through gas-polymer collisions. A series of simulations were performed with four increasing magnitudes for the external field strengths, ranging from 0.01179 to 0.0472 kcal/(mol Å).

After the initial MD equilibration of 3 ns which allows the polymer to saturate with gas, NEMD simulations are performed for 2 ns for the system to reach steady state and subsequently 10 ns to gather statistics. The time step was set to 1 fs. Simulations are started by allowing the gases to saturate the polymer and reach their equilibrium state in the bulk, i.e. no external field is imposed at the boundary. The bulk gas pressure at equilibrium resulted in 10.19 bar for helium and 9.12 bar for carbon dioxide. Equilibrium solubilities were determined from the gas uptake at the respective pressure, $S(P) = c(P)/P$. For helium, 0.065 mmol/cm^3 were adsorbed by the polymer and for carbon dioxide the uptake resulted in 4.73 mmol/cm^3. This corresponds to solubilities

of 0.14 and 11.77 cm^3 (STP) / cm^3 bar, for helium and CO_2 respectively. These results are in good agreement with gas solubilities determined experimentally (Li et al., 2013, 2014; Bezzu et al., 2012), which are reported below 0.25 cm^3 (STP) / cm^3 bar for helium and between 11.2 to 11.3 cm^3 (STP) / cm^3 bar for CO_2.

5.2 Results and Discussion

NEMD simulations are reported for pure helium and carbon dioxide. Helium, being a small, light and relatively inert gas at the conditions here studied, has a high diffusion coefficient in PIM-1 with little adsorption while carbon dioxide strongly adsorbs to the polymer and exhibits low diffusivity. The steady state response of the system during a typical NEMD simulation can be observed in Fig. 5.3, where the region on the left exhibits a higher density than the one on the right. Velocity profiles present the opposite behaviour due to mass continuity. The spikes in density shown in the lower part of Fig. 5.3 (blue line) showcase the strong adsorption of carbon dioxide on the polymer. The profile is shown for the largest force applied ($f_{\text{ex}} = 0.0472\,\text{kcal/molÅ}$). Directly observable from the plot are the differences in density (which relate to pressure differences) between the two bulk sections as well as the average velocity. AS pointed out in section 3.3, the effective flux can be determined from the averages of density and velocity ($J_x = \bar{v}_x\bar{\rho}$). Pressure differences can be obtained from the NEMD simulations directly via the Virial route (Allen and Tildesley, 1987) or by performing a separate simulation of bulk gas to obtain an isotherm and determine the pressure difference corresponding to the densities measured during the NEMD simulations. Upon obtaining the steady-state flux and pressure difference, equation 5.2 was employed to determine permeabilities, with Δx being equal to the thickness of the polymer slice (4.53 nm). The results in comparison to experimental data are shown in Fig. 5.4. Experimental data was reported from time-lag and gas chromatography experiments of PIM-1 membranes (Budd et al., 2008, 2005; Li et al., 2013, 2014; Bezzu et al., 2012). The spread in experimental results presumably stems from the different methods and solvents used in casting of the membrane and subsequent treatments. The permeability of carbon dioxide obtained in this work, through the thin slice model polymer, is in very good agreement with experimental data, lying at the upper end of the data range. The result obtained for helium in this work is above the spread of experimental data. The permeabilities obtained in this work might also be overpredicted since hydrogen atoms are not explicitly modelled but lumped together as a group with their bon-

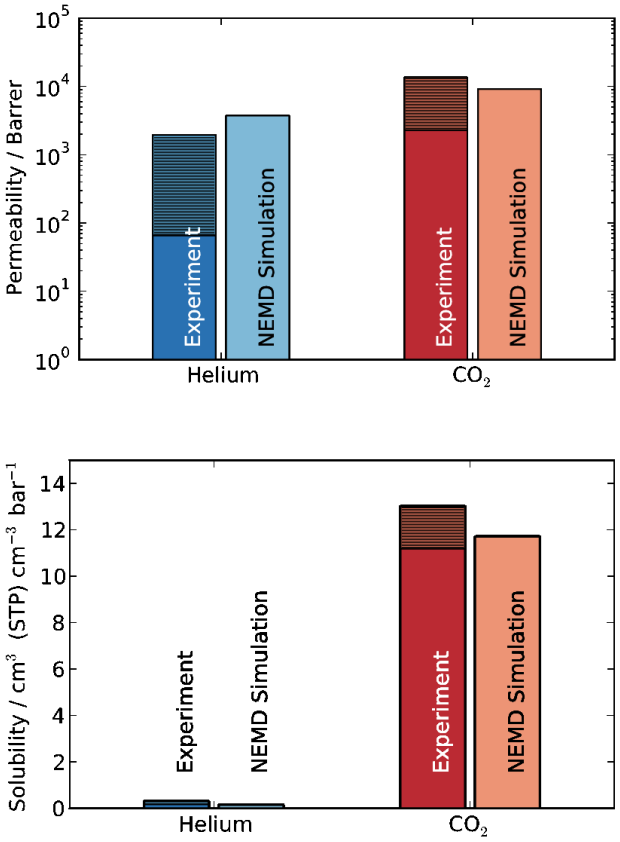

Figure 5.4: Permeability and solubility results from NEMD simulations compared to experimental results for helium in blue and carbon dioxide in red. The shaded area of the bar chart shows the spread of experimental data (Budd et al., 2005, 2008; Li et al., 2013, 2014; Bezzu et al., 2012).

ded carbon atoms, resulting in a smoother structure as opposed to the full-atomistic detailed model. In other words, a smoother force field exhibits higher diffusivity because there is less molecular friction within the system. Additionally, the interfacial regions could also contribute to higher transport by exhibiting more free volume than the bulk regions.

The NEMD approach closely mimics how experiments are conducted to characterise membrane separation performance, yielding a macroscopic view on the gas permeation through the polymer. However, it also allows further investigation of effects influencing transport on the molecular scale with an abundance of detailed information not available through physical experiments. The specific diffusion paths for each gas molecule individually can be obtained from the simulation trajectories. One of such trajectories is plotted in Fig. 5.5 where the time dimension is colour-coded. It

starts at purple and blue and progresses through the colour spectrum to yellow and red. The trajectory shown is a small excerpt from the full 10 ns trajectory to showcase a single permeation event through the polymer slice. The differences between the permeation of carbon dioxide and helium become apparent in Fig. 5.5. The diffusion of carbon dioxide is slowed down by frequent and complex interactions inside the polymer and in the event shown in Fig. 5.5, the passage takes 3400 ps compared with only 80 ps for helium. As expected, a helium atom interacts very little with the polymer and finds a path through the polymer matrix much more quickly than a CO_2 molecule. Both pathways suggest that molecules within the polymer matrix spend a considerable amount of time in "random walks" throughout the extent of the available free volume, i.e. the mechanism deviates from a simple "pore hopping" trajectory expected for a dense polymer as a result of exhibiting highly interconnected porosity. The occurrence of pore hopping is likely proportional to the amount of pore volume, and thus high free volume polymers exhibit fewer pore hopping events during permeation. As such, penetrant molecules that plasticise the polymer matrix to a greater extent may induce further deviation from the solution-diffusion model. For example, it has been suggested that alcohols and alkanes, which considerably swell the PIM-1 membrane, are well described by a convective transport model and exhibit pore flow transport (Vopička et al., 2013). The extent to which pore flow contributes to the permeation of these gases in PIM-1 has, however, yet to be quantified.

Experimentally determined diffusion coefficients are in the order of 100 and 3000 $\times 10^{-8}$cm^2/s for CO_2 and helium, respectively, although reported diffusivities can vary as much as permeabilities do. If a characteristic length to compare diffusion processes were defined as $L = 2\sqrt{D\tau}$, where D is the diffusion coefficient and τ the time span, one can then determine this diffusion length based on the duration of the passages in Fig. 5.5. With 3.4 ns for CO_2 and 80 ps for Helium, this results in diffusion lengths of 3.7 nm for CO_2 and 3.1 nm for Helium, numbers that compare well with the thickness of the polymer at 4.5 nm.

An aggregate perspective on the diffusion paths underlines this aspect further. Figure 5.6 shows three slices of the density distributions accumulated over an entire 10 ns simulation in the xz plane. The regions occupied by the polymer which are not accesible to the gas molecules are depicted in green. They are interfused by red denoting an average occupation and white areas which denote frequently explored diffusion channels for the gases. These channels are highly connected and build a percolated diffusion path through the polymer. This path is very tortuose, but it percolates from

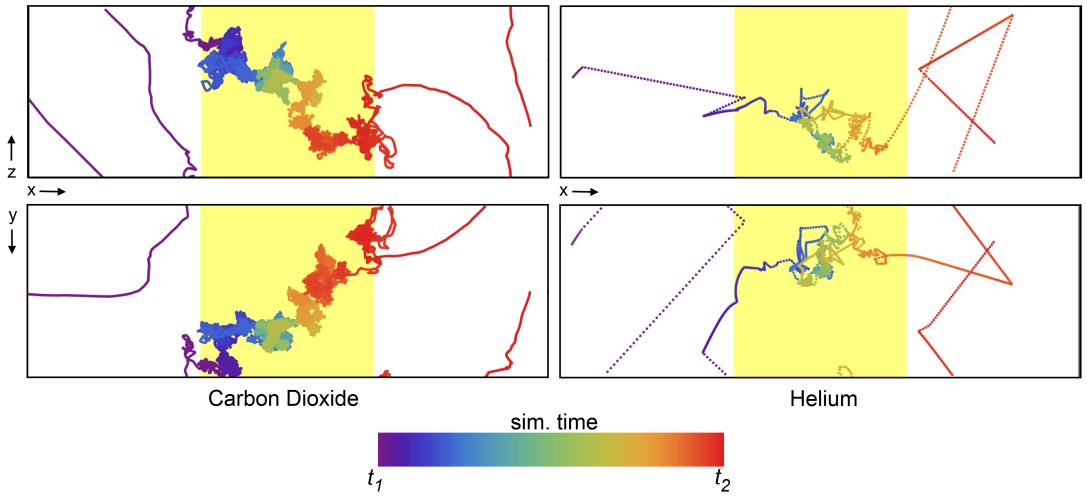

Figure 5.5: The movement of a single CO_2 molecule (left) and He atom (right) through the polymer matrix (yellow shaded region). Each point represents the location of a molecule at every 0.5 ps of simulation time, with the colour of the points scaled according to the relative time (see colour bar). The simulation time was selected such that only a single permeation event of the many occurring during the 10 ns simulation is shown. $\Delta t = t_1 - t_2$ is 3.4 ns for CO_2 and 80 ps for Helium. The top and bottom plots represent the XZ and YX projections, respectively.

one bulk region to the next. The density plots (Fig. 5.3) and density distribution maps (Fig. 5.6) show an enhanced excess adsorption of CO_2 at the solid-fluid interface. This behaviour is commensurate with the interfacial properties of CO_2 at room temperature and the high pressures employed.

The influence of free volume on permselectivity and permeability of gases in glassy polymers is the focus of a number of recent studies with the objective of pushing the trade-offs between selectivity and permeability past its current thresholds. When measuring permeability experimentally, one has the option to measure either time-lag diffusion or secant solubility and invoking the solution-diffusion model ($S = P/D$ or $D = P/S$) to obtain the other property of interest. Robeson et al. (Robeson et al., 2014) noted a discrepancy between these two alternative routes and showed that the deviation between diffusion coefficients in PIM-1 depends on pressure and can amount to more than 50% in the pressure range 8-12 bar. Similar trends were observed by Li et al. (Li et al., 2014) upon measuring the temperature and pressure dependence of permeability in PIM-1. They found a decline in carbon dioxide permeability in the pressure range from 1-10 bar of up to 25%. These observations underline the nature and limitations of the solution-diffusion model where the main assumption is that the

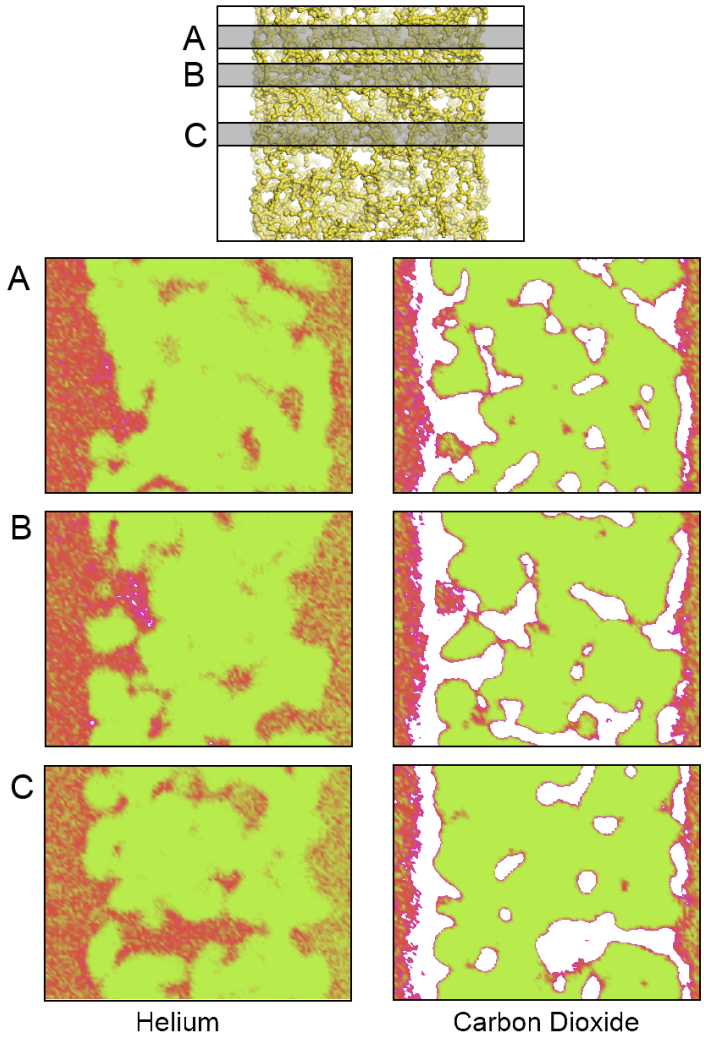

Figure 5.6: A density map showing the density of locations for the (left) He atoms and (right) CO_2 molecules on an XZ projection calculated at three different Y slices: (A) 0.675, (B) 1.275 and (C) 2.775 nm, from top to bottom respectively. The plots show areas of high (white), average (red), and low (green) gas density. The top model shows the relative location of the polymer and the corresponding plane locations. Only a small fraction of the bulk fluid sections is depicted to the left and right of each plot.

sorption process and several transport phenomena are all sequentially related and independent. NEMD simulations follow the experimental approach very closely and do not rely on the solution-diffusion model to obtain permeabilities.

Li et al. point out that as "the molecular picture of the solid-state structure is still emerging" (Li et al., 2014), the main reason for high permeability through PIM-1 and other glassy high free volume fraction are high diffusion coefficients. The simulation

data concur with this view point by highlighting the considerable diffusion path accessibility inside the polymer. While dense glassy polymers are situated at one end of the spectrum, exhibiting a common pore hopping diffusion mechanism, and structured materials with sieving and Knudsen-type separation mechanisms at the other end of the spectrum, the separation mechanism in high free volume polymers seems to simultaneously exploit the tortuosity of its diffusion path and the energetic interaction between polymer solid and permeating gases. Mixed-matrix membranes of glassy polymers and structured molecular materials, such as MOF or carbon structures, are garnering interest for improved separation performance by tapping into both regimes (Bushell et al., 2013). The method herein presented would be ideally suited to study in detail the transport dynamics of such inhomogeneous materials. It is well known that physical ageing, residues of casting solvents, humidity, plasticisation and swelling can influence significantly. *In silico* experiments are ideally clean and any of these mentioned effects can or should be controlled individually. NEMD permeation experiments could be further employed to investigate the details of how the presence of pollutants can influence transport dynamics at the smallest scale.

5.3 Conclusions

As opposed to measuring self-diffusion coefficients and invoking the solution-diffusion model to obtain permeation properties, this study obtains a picture from an atomistically detailed simulation of direct gas permeation through a slice of PIM-1 polymer. The thin polymer slice was generated by the Polymatic algorithm and compares very well with 3D-periodic simulated samples in terms of porosity and pore size distributions. By confining the generated structure between rigid walls, the polymer slice is forced to keep its structure resembling the 3D periodic image of a bulk. With gas regions placed on either side of the slice, direct permeation simulations were performed by applying a non-equilibrium scheme. In analogy to experimental measurements, permeabilities were calculated from the steady-state flux and pressure gradient. As the simulation is initiated with an equilibrium simulation to allow the gases to saturate the polymer before applying external perturbations, adsorption characteristics can also be calculated. Although there are large uncertainties in the experimental results for gas permeability in PIM-1 and the molecular interaction force fields are not fitted explicitly to transport properties, the quality of agreement is good. Furthermore, the information obtained from NEMD simulations sheds light on the diffusion mechan-

ism. In this case, a deviation from a straightforward gate-hopping mechanism was observed. Moreover, the present approach allows for a range of crucial phenomena to be investigated in silico. Most notably, the approach lends itself to the simulation of mixtures and complex organic molecular fluids as well as composite and inhomogeneous membranes. Similarly, the approach could be refined to account for swelling of the polymer (Eslami and Müller-Plathe, 2009).

CHAPTER

SIX

CONCLUDING REMARKS AND OUTLOOK

The study of mass transport properties through molecular simulation is predominantly focused on determining self-diffusion coefficients of bulk fluids. Thermodynamic effects linked to the compressibility of the fluid and other intricacies, such as the influence on collective diffusion, are often neglected. In an attempt to show the significance of these effects for confined fluids, this work has given several examples how molecular simulations that focus on effective transport properties can be carried out. Moreover, it has highlighted the effective application of molecular simulations in determining transport properties for abstract and realistic porous materials. The results are a valuable contribution towards the understanding and rationalisation of various theoretical interpretations as well as their connection to experiments.

The investigations carried out in this work were particularly concerned with application of boundary-driven NEMD simulations to determine effective mass transport coefficients in planar slit pores as well as complex polymeric structures. The approach is useful in determining effective diffusion coefficients and permeabilities and, in general, compares well with alternative simulation methodologies with respect to computational effort and ease of application. However, boundary-driven NEMD simulations cannot be considered a "magic bullet". As is the case for simulations of transport properties in general, the computational expense is considerable and, while it is possible to overcome a number of complications, the methodology suffers limitations in areas such as very dilute concentrations in explicitly modelled molecular materials or extremely dense systems in which perturbations can affect transport adversely. Notwithstanding, equilibrium simulation methods based on the Darken approach have similar limitations for these extreme cases. These shortcomings are partly

compensated by the fact that useful tractable theories exist for these extreme scenarios, especially at the low density limit.

The advantage of boundary-driven NEMD approach is that it is easily implemented in existing Molecular Dynamics simulation software. Because complex changes to the source code can often be avoided, the application of the methodology is greatly facilitated. Furthermore, for multi-component systems with complex molecules, competing approaches such as the DCV-GCMD are very inefficient or cumbersome to be widely applied, but boundary-driven NEMD is ideally suitable for such applications.

Beyond such application, it remains to be pointed out that the application of external perturbations at the boundary can be used for entirely different purposes. In what follows, two examples are given in which the boundary-driven NEMD methodology was used to determine self-diffusion via a cross-colour diffusion scenario, as well as the application of NEMD simulation in determining the rejection performance of ultra-thin membrane structures. These are slightly different problems from the single-component mass transfer studied in the preceding chapters. These two examples are merely showing the possibilities beyond the scenarios the methodology was applied to so far and barely scratch the surface of the areas they intend to inquire into and are summarised here to pave the way for further studies.

6.1 Avendaño's demon and the self-diffusion coefficient

With the external field applied in only one direction within a slit pore system as it is described in section 3.3, the fluid acquires momentum in the direction of the force and upon reaching the steady state, the system exhibits unidirectional flow. As pointed out previously, the slit pore poses a resistance to the flow and creates a build up in density on one side. The system is therefore brought out of mechanical equilibrium and the mass flux measured has a convective contribution. The measured transport coefficient is an effective diffusivity as outlined in Chapter 3 and 4. As an alternative to the Green-Kubo approach to obtain self-diffusion, a non-equilibrium method is proposed which allows the calculation of self-diffusivity D_{s} in an independent manner, considering a system which externally appears to be at or very close to equilibrium. The homogeneous fluid is artificially equipartitioned into two differently tagged species, i.e. of different "colour", that otherwise are identical. Furthermore, an external force is applied to the system on the opposite side of the simulation box and acting in the opposite direction, but only on one particular coloured species, while the original force

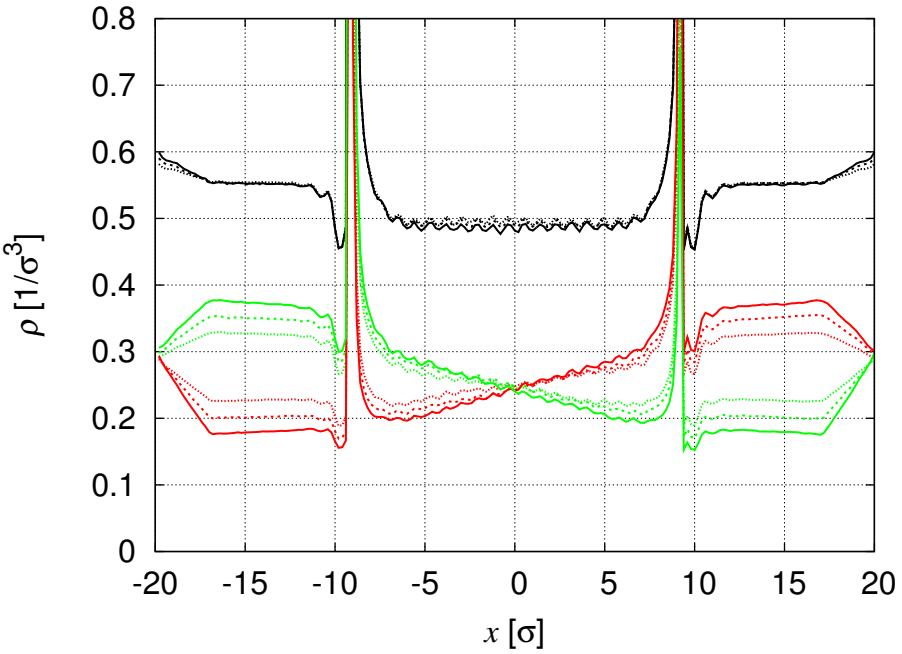

Figure 6.1: Density gradients for the narrow pore, $H = 2.5$, at $f_{\text{ex}} = 0.2, 0.3, 0.4$ represented by dotted, dashed and solid lines, respectively. The black lines correspond to the overall density, while the red and green lines are the gradients of the pseudo-species.

field acts on the second species only. The flow of one species is therefore countered by a flow of the other species. The pressure and total density in the system can thus be maintained uniform and with the heat being rapidly removed from the system, it is also at a constant temperature. In other words, a "colour-blind" observer would only see a bulk fluid in equilibrium. The only gradient in this system is a colour concentration gradient of the two pseudo-species. The opposing force field distinguishes between the two species and separates them at the boundary. The mechanism, which has been named "Avendaño's demon", can be compared to a Maxwell demon that is able to reduce the entropy of the system (Thomson, 1879). Similar approaches to separate the colour-distinguished species involve the insertion and deletion of particles, such as the DCV-GCMD method (Heffelfinger and van Swol, 1994), or a stochastic enhancement of the periodic boundary conditions under which some molecules are reflected from the boundary according to a certain probability (Whitman et al., 2011). This approach was published alongside the boundary-driven NEMD approach as it is closely related (Frentrup et al., 2012).

Counter-flux simulations of the planar slit pore were carried out, in which the pore

is located at the centre of the pore, surrounded by two bulk regions on either side, similar to the system described in Chapter 3 and 4. Likewise, two variations for the pore width were simulated, a narrow and wide pore of pore width 2.5 and 5.0, respectively. The system setup was identical to the systems in Section 3.3 (small realisations for both pores) and the average density of the fluid, $\hat{\rho}$, was estimated in the same way (by dividing the number of particles by the volume accessible to the fluid, estimated from the total volume minus the box shaped volume of the solid; see Table 3.1 for details). Fig. 6.1 depicts the density distribution along the x axis in a narrow slit pore. It shows that the total density in the system is uniform except for the section where the opposing forces have been applied. A slight increase in density is recorded in this region. It stems from the opposing external fields that push the molecules into each other and provoke a slight increase in pressure, and therefore also a rise in density. In the central part of the simulation, the density is uniform and it can be concluded that the simulation is very close to a state of mechanical equilibrium. The distribution of the two colour-distinguished species of the fluid can also be taken from Fig. 6.1. The density gradients exhibit a linear behaviour and the slope can be calculated from the profiles by fitting a linear function to the density distribution. By obtaining the molar flux for each species as well as the density gradients from the profiles in Fig. 6.1, the same pseudo-Fickian approach can be inkoved to determine "colour" diffusion coefficients:

$$J_i = -D_{\mathrm{x,i}} \frac{\mathrm{d}\rho_i}{\mathrm{d}x} \tag{6.1}$$

The two species have opposing gradients of the same magnitude, which can be taken from Table 6.1. The approach gives a similar picture to the density gradient in the DCV-GCMD approach (Heffelfinger and van Swol, 1994), with a similar counter-flux of colour-distinguished species of an otherwise homogeneous LJ fluid. Along with the density gradients, the flux for each species is given in the same table for three different external field strengths. Based on this information, the diffusivity of each "colour" can be calculated similar to the way it was calculated for the pressure-induced diffusion. For the systems discussed in the previous section, the molecular flux happens predominantly in one direction only, due to the presence of a pressure difference, and the diffusion coefficient has a certain convective contribution to it. With the mechanical equilibrium restored by opposing forces acting each on the colour-distinguished species, the flux for each species is opposed to the other species' flux and these counter-fluxes hinder mutually the diffusion of each species. The magnitude of the external force has an effect on the magnitude of the flux and the slope of the density gradient.

f_{ex}	J_1	J_2	$\frac{\mathrm{d}\rho_1}{\mathrm{d}x}$	$\frac{\mathrm{d}\rho_2}{\mathrm{d}x}$	$D_{\mathrm{x},1}$	$D_{\mathrm{x},2}$
$H = 2.5,$ Average density $\hat{\rho} = 0.553$						
0.2	-0.0018(6)	0.0021(6)	0.00411	-0.00428	0.5(2)	0.5(1)
0.3	-0.0030(3)	0.0031(5)	0.00580	-0.00586	0.53(6)	0.52(8)
0.4	-0.0041(5)	0.0041(6)	0.00781	-0.00775	0.52(6)	0.53(7)
$H = 5.0,$ Average density $\hat{\rho} = 0.545$						
0.2	-0.0012(3)	0.0013(3)	0.00336	-0.00344	0.37(9)	0.37(9)
0.3	-0.0020(2)	0.0018(2)	0.00489	-0.00494	0.40(3)	0.35(3)
0.4	-0.0025(3)	0.0023(3)	0.00657	-0.00669	0.39(4)	0.39(4)

Table 6.1: Avendaño's demon results for the small realisations of the narrow and wide pore. The number in the parentheses denotes the uncertainty in the last digit.

It has no effect on the diffusion coefficients as in this case there is no convective contribution. A large external force is beneficial in this case, as the uncertainties for the calculation of the diffusion coefficient decrease with a stronger force field.

The resulting "colour" diffusion coefficients $D_{\mathrm{x,i}}$, 0.52 for the narrow pore and 0.38 for the wide pore, are an order of magnitude lower than in the case of unidirectional mass transport, which is in the order of 3.1 for the narrow and 24.0 for the wide pore (see $D_{\mathrm{eff}}^{\mathrm{NEMD}}$ in Table A.3 and A.5). The transport diffusion coefficient corresponds exclusively to D_{t}. In the absence of convective forces and only one type of fluid-fluid interaction present, a comparison to the self-diffusion coefficient is in order. The results for the self-diffusion coefficient of the confined fluid were independently calculated from the MSD in the xy plane using the trajectories of EMD simulations. For the narrow pore, the two-dimensional ($d = 2$) self-diffusivity $D_{\mathrm{s},xy} = 0.508$ at $\rho = 0.57$, and for the wide pore, $D_{\mathrm{s},xy} = 0.402$ at $\rho = 0.54$. The results are of the same order of magnitude and agree very well. It is worth noting that both methods indicate a higher diffusivity of the narrow pore, presumably because of confinement which favours a ballistic transport (Cruz and Müller, 2009; Barati Farimani and Aluru, 2011).

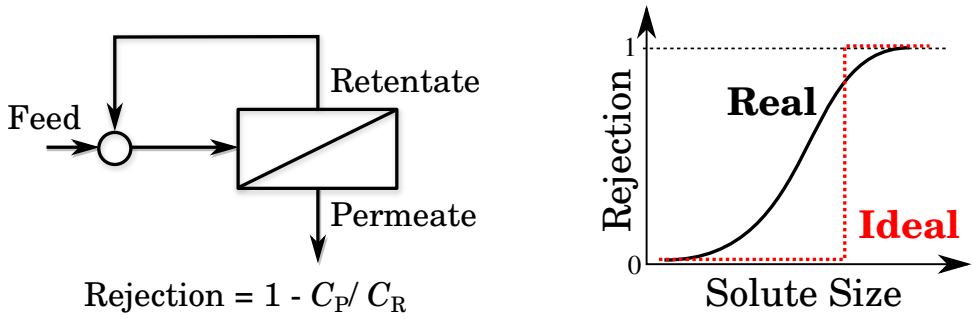

Figure 6.2: Schematic drawing of a membrane separation process (left) and the corresponding rejection curve of a common membrane.

6.2 Rejection Modelling

Since molecular simulations model transport dynamics by incorporating the system's full molecular character, they can support existing theories where their assumptions are brought in question because of finite-size effects. Especially in the case of ultra-thin membranes that are merely a few molecular diameters in thickness, they can help answer question such as whether an infinitely thin membrane would constitute the ideal membrane or whether it is possible to achieve ideal separation characteristics at all.

The ideal characteristics of a membrane are maximum flux and ideal separation, while it is obvious that there is a trade-off between them. It is a long-standing goal of membrane science to control the molecular-weight cut-off (MWCO) of a membrane, which means that the membrane is very permeable to species of small molecular weight (which correlates to molecular size) but perfectly retains molecules of a specific site. In reality the rejection curve is not ideal and a sharp cut-off is impossible to achieve. A typical rejection curve in comparison to the ideal scenario is shown in Fig. 6.2, which indicates that the actual separation performance is "smeared".

This smearing effect can be explained through a hindered diffusion process (Deen, 1987). If we consider solutes of a specific size in an implicit solvent, meaning the solvent will behave according to classical hydrodynamics, steric exclusion and other effects such as electrostatic or other membrane-solute interactions can be incorporated into the the transport equations. It is important to note that the length of the pore, i.e. the membrane thickness, is assumed to be much bigger than the pore size. Unrelated of whether diffusive or convective flow dominate the separation process, solutes that are smaller than the size of the pore are still hindered in their passing because of in-

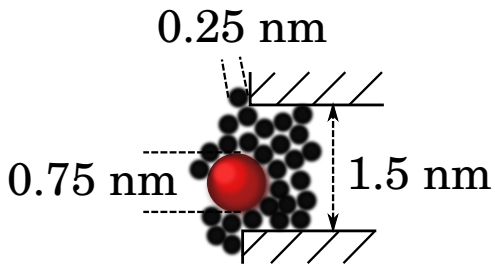

Figure 6.3: This schematic drawings shows the geometry of the solute and solvent fluid particles in relation to the pore size of the membrane.

pore resistance against flow.

A series of systems with pores of different lengths (between 2.5 nm and 118 nm) was set up. The pore width was fixed at 1.5 nm and solutes were half the size of the pore, i.e. 0.75 nm. The solvent was modelled explicitly as LJ spheres with 0.25 nm diameter (shown in Fig. 6.3). The wall was modelled as a slit-shaped structure of varying length comprised of repulsive spheres (WCA potential), which resembles the structures in Section 3.3 and Chapter 4. The external field was applied at the left boundary, solvent particles felt a moderate force of $0.1\epsilon/\sigma$ in the positive x direction, while solute particles felt a very strong force into the negative x direction upon entering the thin slab ($10\epsilon/\sigma$). This generates a steady state flux of solvent particles in the x direction but prevents solute particles from passing the boundary. The only way for solute particles to pass from the left bulk region to the right is a passage through the pore. The rejection is then measured in the simulations in a similar fashion as in experiments, by comparing the solute concentrations of permeate and retentate. The results of the simulations is given in Fig. 6.4.

It can be seen that the pore's rejection of solute particles half the size of the pore decreases as the "membrane" gets thinner. Since the pore is double the size of the solute, there are no steric exclusion effects present and a thinner membrane enables particles to permeate through the membrane more easily while particles bigger than the pore size would be retained completely. It is also possible to deduce from Fig. 6.4 that in order for thin membranes to have a sharper rejection profile, the pore length needs to be in the order of the pore width ($L \sim H$). A dramatic decrease in rejection can be seen for a pore length of less than 10 nm. This is an interesting finding because it shows that in these cases entrance effects perform the separation rather than the transport dynamics inside the pore.

This point of view is in line with the established perspective following the hindered

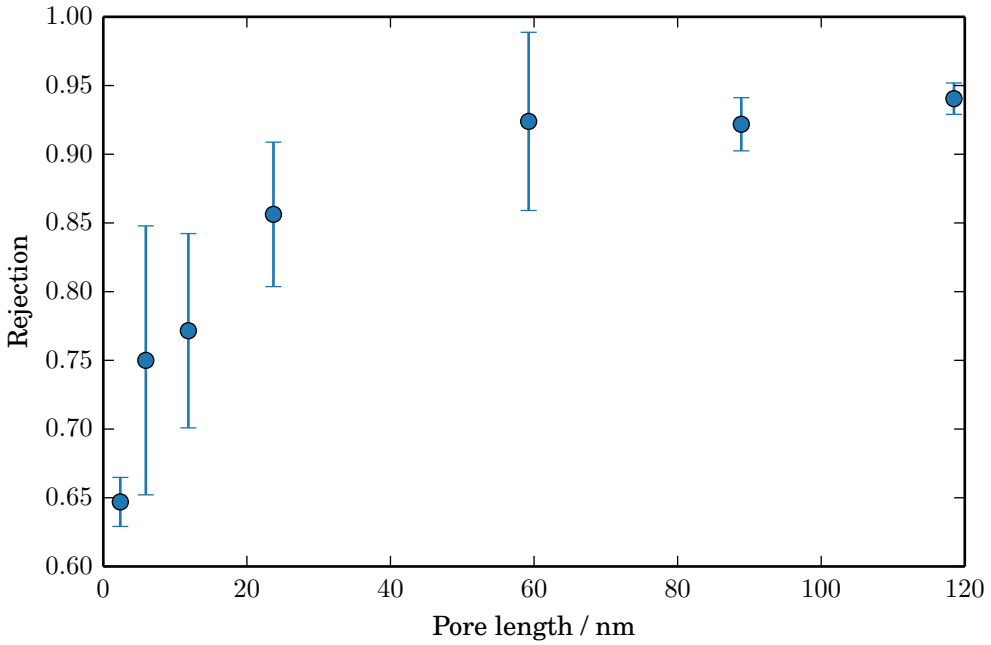

Figure 6.4: Simulation results for rejection as a function of the pore length. Rejection is calculated as follows: $R = 1 - c_{\mathrm{P}}/c_{\mathrm{R}}$. The error bars are estimates from 5 independent simulations.

diffusion model of Deen (1987). Hindered diffusion relies on hydrodynamic flow being fully developed inside the pore and it is assumed that the length of the pore is much larger than the pore diameter ($L_\mathrm{p} >> H$). As the pore gets shorter, the full development of hydrodynamic flow is impeded by the entrance effects. For an infinitely short pore, it can be envisioned that the flow conditions inside the pore are equivalent to those in the bulk and therefore purely steric effects generate selectivity. This in turn would result in an ideal membrane. Creating infinitely short pores is, of course, physically not possible and even making membranes as thin as two times the pore size (see Fig. 6.5) is extremely challenging for most purposes. However, membranes comprised of a single graphene layer perforated by electron beams, which punches geometrically well-defined nanoholes into the material, have been created in the laboratory (Zan et al., 2012) and the race to bring such technology into real-world applications is already well under way.

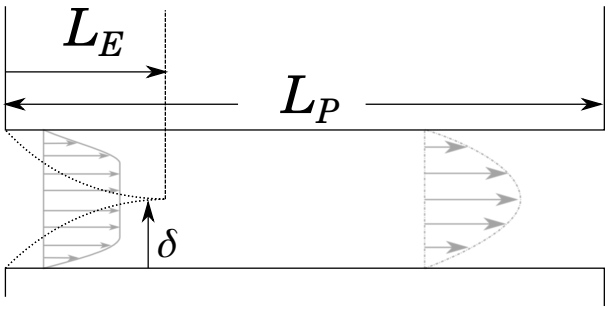

(a) Under the assumption that the pore is considerably longer than the pore diameter, it can be assumed that hydrodynamic flow is fully developed inside the pore.

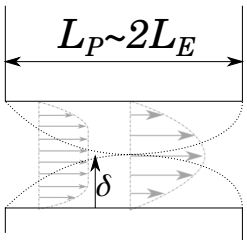

(b) For membranes that are almost as thick as their pores are wide, the development of hydrodynamic flow is impeded.

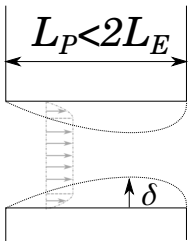

(c) As the pores get very short, hydrodynamic flow cannot develop inside the pores and the conditions of the fluid are equivalent to those of the bulk fluid.

Figure 6.5: The schmematic drawings highlight the influence of pore length on the ability of pores to allow the full development of hydrodynamic flow.

BIBLIOGRAPHY

L. J. Abbott (2013). 'Polymatic: A simulated polymerization algorithm, v. 1.0.'

L. J. Abbott, K. E. Hart, and C. M. Colina (2013). 'Polymatic: A generalized simulated polymerization algorithm for amorphous polymers.' *Theoretical Chemistry Accounts*, **132**, 1334.

M. K. F. Abouelnasr and B. Smit (2012). 'Diffusion in confinement: Kinetic simulations of self- and collective diffusion behavior of adsorbed gases.' *Physical Chemistry Chemical Physics*, **14**, 11600.

D. J. Adams (1974). 'Chemical potential of hard-sphere fluids by Monte Carlo methods.' *Molecular Physics*, **28**, 1241.

S. E. Albo, L. J. Broadbelt, and R. Q. Snurr (2006). 'Multiscale modeling of transport and residence times in nanostructured membranes.' *AIChE Journal*, **52**, 3679.

B. J. Alder and T. E. Wainwright (1957). 'Phase transition for a hard sphere system.' *Journal of Chemical Physics*, **27**, 1208.

M. P. Allen and D. J. Tildesley (1987). *Compter Simulation of Liquids*. Oxford University Press, Oxford, UK.

H. Amrouche, B. Creton, F. Siperstein, and C. Nieto-Draghi (2012). 'Prediction of thermodynamic properties of adsorbed gases in zeolitic imidazolate frameworks.' *RSC Advances*, **2**, 6028.

M. A. Aroon, A. F. Ismail, T. Matsuura, and M. M. Montazer-Rahmati (2010). 'Performance studies of mixed matrix membranes for gas separation: A review.' *Separation and Purification Technology*, **75**, 229.

G. Arya, H.-C. Chang, and E. J. Maginn (2001). 'A critical comparison of equilibrium, non-equilibrium and boundary-driven Molecular Dynamics techniques for studying transport in microporous materials.' *Journal of Chemical Physics*, **115**, 8112.

G. Arya, H.-C. Chang, and E. J. Maginn (2003). 'Knudsen diffusivity of a hard sphere in a rough slit pore.' *Physical Review Letters*, **91**.

C. Avendaño, T. Lafitte, A. Galindo, C. S. Adjiman, G. Jackson, and E. A. Müller (2011). 'SAFT-γ force field for the simulation of molecular fluids. 1. A single-site coarse grained model of carbon dioxide.' *Journal of Physical Chemistry B*, **115**, 11154.

R. W. Baker (2002). 'Future directions of membrane gas separation technology.' *Industrial & Engineering Chemistry Research*, **41**, 1393.

A. Barati Farimani and N. R. Aluru (2011). 'Spatial diffusion of water in carbon nanotubes: From Fickian to ballistic motion.' *Journal of Physical Chemistry B*, **115**, 12145.

P. Bernardo, E. Drioli, and G. Golemme (2009). 'Membrane gas separation: A review/state of the art.' *Industrial & Engineering Chemistry Research*, **48**, 4638.

C. G. Bezzu, M. Carta, A. Tonkins, J. C. Jansen, P. Bernardo, F. Bazzarelli, and N. B. McKeown (2012). 'A spirobifluorene-based polymer of intrinsic microporosity with improved performance for gas separation.' *Advanced Materials*, **24**, 5930.

S. K. Bhatia (2010). 'Modeling pure gas permeation in nanoporous materials and membranes.' *Langmuir*, **26**, 8373.

S. K. Bhatia, M. R. Bonilla, and D. Nicholson (2011). 'Molecular transport in nanopores: A theoretical perspective.' *Physical Chemistry Chemical Physics*, **13**, 15350.

S. K. Bhatia, H. Chen, and D. S. Sholl (2005). 'Comparisons of diffusive and viscous contributions to transport coefficients of light gases in single-walled carbon nanotubes.' *Molecular Simulation*, **31**, 643.

S. K. Bhatia, O. G. Jepps, and D. Nicholson (2004). 'Tractable molecular theory of transport of Lennard-Jones fluids in nanopores.' *Journal of Chemical Physics*, **120**, 4472.

S. K. Bhatia and D. Nicholson (2003). 'Hydrodynamic origin of diffusion in nanopores.' *Physical Review Letters*, **90**, 16105.

M. J. Biggs and A. Buts (2006). 'Virtual porous carbons: What they are and what they can be used for.' *Molecular Simulation*, **32**, 579.

R. B. Bird, W. E. Stewart, and E. N. Lightfoot (2002). *Transport Phenomena*. Jon Wiley & Sons Inc., New York, USA, 2nd edition.

I. A. Bitsanis, J. J. Magda, M. Tirrell, and H. T. Davis (1987). 'Molecular Dynamics of flow in micropores.' *Journal of Chemical Physics*, **87**, 1733.

I. A. Bitsanis, T. K. Vanderlick, M. Tirrell, and H. T. Davis (1988). 'A tractable molecular theory of flow in strongly inhomogeneous fluids.' *Journal of Chemical Physics*, **89**, 3152.

J. Borak and W. F. Diller (2001). 'Phosgene exposure: Mechanisms of injury and treatment strategies.' *Journal of Occupational and Environmental Medicine*, **43**, 110.

W. R. Bowen and J. S. Welfoot (2002). 'Predictive modelling of nanofiltration: Membrane specification and process optimisation.' *Desalination*, **147**, 197.

R. Brown (1828). 'A brief account of microscopical observations made in the months of June, July and August, 1827, on the particles contained in the pollen of plants; and on the general existence of active molecules in organic and inorganic bodies.' *Philosophical Magazine*, **4**, 358.

D. Brown and J. H. R. Clarke (1984). 'A comparison of constant energy, constant temperature and constant pressure ensembles in molecular dynamics simulations of atomic liquids.' *Molecular Physics*, **51**, 1243.

A. Brunetti, F. Scura, G. Barbieri, and E. Drioli (2010). 'Membrane technologies for CO2 separation.' *Journal of Membrane Science*, **359**, 115.

P. M. Budd and N. B. McKeown (2010). 'Highly permeable polymers for gas separation membranes.' *Polymer Chemistry*, **1**, 63.

P. M. Budd, N. B. McKeown, B. S. Ghanem, K. J. Msayib, D. Fritsch, L. Starannikova, N. Belov, O. Sanfirova, Y. Yampolskii, and V. Shantarovich (2008). 'Gas permeation parameters and other physicochemical properties of a polymer of intrinsic microporosity: Polybenzodioxane PIM-1.' *Journal of Membrane Science*, **325**, 851.

P. M. Budd, K. J. Msayib, C. E. Tattershall, B. S. Ghanem, K. J. Reynolds, N. B. McKeown, and D. Fritsch (2005). 'Gas separation membranes from polymers of intrinsic microporosity.' *Journal of Membrane Science*, **251**, 263.

A. F. Bushell, M. P. Attfield, C. R. Mason, P. M. Budd, Y. Yampolskii, L. Starannikova, A. Rebrov, F. Bazzarelli, P. Bernardo, J. Carolus Jansen, M. Lanč, K. Friess, V. Shantarovich, V. Gustov, and V. Isaeva (2013). 'Gas permeation parameters of mixed matrix membranes based on the polymer of intrinsic microporosity PIM-1 and the zeolitic imidazolate framework ZIF-8.' *Journal of Membrane Science*, **427**, 48.

Q. Cai, M. J. Biggs, and N. A. Seaton (2008). 'Effect of pore wall model on prediction of diffusion coefficients for graphitic slit pores.' *Physical Chemistry Chemical Physics*, **10**, 2519.

J. Castillo-Tejas, A. Rojas-Morales, F. López-Medina, J. F. J. Alvarado, G. Luna-Bárcenas, F. Bautista, and O. Manero (2009). 'Flow of linear molecules through a 4:1:4 contraction-expansion using non-equilibrium molecular dynamics: Extensional rheology and pressure drop.' *Journal of Non-Newtonian Fluid Mechanics*, **161**, 48.

P. M. Chaikin and T. C. Lubensky (1995). *Principles of Condensed Matter Physics*. Cambridge University Press, Cambridge, UK.

K.-S. Chang, K.-L. Tung, Y.-F. Lin, and H.-Y. Lin (2013). 'Molecular modelling of polyimides with intrinsic microporosity: From structural characteristics to transport behaviour.' *RSC Advances*, **3**, 10403.

S. Chapman and T. G. Cowling (1939). *Mathematical Theory of Non-Uniform Gases*. Cambridge University Press, Cambridge, UK.

S. Chempath, R. Krishna, and R. Q. Snurr (2004). 'Non-equilibrium Molecular Dynamics simulations of diffusion of binary mixtures containing short n-alkanes in faujasite.' *Journal of Physical Chemistry B*, **108**, 13481.

S.-S. Chong, H. Jobic, M. Plazanet, and D. S. Sholl (2005). 'Concentration dependence of transport diffusion of ethane in silicalite: A comparison between neutron scattering experiments and atomically detailed simulations.' *Chemical Physics Letters*, **408**, 157.

X.-Q. Chu, G. Ehlers, E. Mamontov, A. Podlesnyak, W. Wang, and D. J. Wesolowski (2011). 'Diffusion processes in water on oxide surfaces: Quasielastic neutron scattering study of hydration water in rutile nanopowder.' *Physical Review E*, **84**, 031505.

R. F. Cracknell, D. Nicholson, and K. E. Gubbins (1995a). 'Molecular Dynamics study of the self-diffusion of supercritical methane in slit-shaped graphitic micropores.' *Journal of the Chemical Society, Faraday Transactions*, **91**, 1377.

R. F. Cracknell, D. Nicholson, and N. Quirke (1995b). 'Direct molecular dynamics simulation of flow down a chemical potential gradient in a slit-shaped micropore.' *Physical Review Letters*, **74**, 2463.

F. J. A. L. Cruz and E. A. Müller (2009). 'Behavior of ethylene and ethane within single-walled carbon nanotubes, 2: Dynamical properties.' *Adsorption*, **15**, 13.

E. L. Cussler (2009). *Diffusion: Mass Transfer in Fluid Systems*. Cambridge University Press, Cambridge, UK, 3rd edition.

S. R. de Groot and P. Mazur (1962). *Non-equilibrium Thermodynamics*. North-Holland Publishing Company, Amsterdam, Netherlands.

W. M. Deen (1987). 'Hindered transport of large molecules in liquid-filled pores.' *AIChE Journal*, **33**, 1409.

W. Eckhardt, A. Heinecke, R. Bader, M. Brehm, N. Hammer, H. Huber, H.-G. Kleinhenz, J. Vrabec, H. Hasse, M. Horsch, M. Bernreuther, C. W. Glass, C. Niethammer, A. Bode, and H.-J. Bungartz (2013). '591 TFLOPS multi-trillion particles simulation on SuperMUC.' In *Supercomputing - XXVIII. International Supercomputing Conference (ISC 2013)*. Leipzig, Germany.

A. Einstein (1905). 'Über die von der molekularkinetischen Theorie der Wärme geforderte Bewegung von in ruhenden Flüssigkeiten suspendierten Teilchen.' *Annalen der Physik*, **322**, 549.

H. Eslami and F. Müller-Plathe (2009). 'Structure and mobility of nanoconfined polyamide-6,6 oligomers: Application of a Molecular Dynamics technique with constant temperature, surface area, and parallel pressure.' *Journal of Physical Chemistry B*, **113**, 5568.

D. J. Evans and O. Morriss (1984). 'Non-Newtonian Molecular Dynamics.' *Computer Physics Reports*, **1**, 297.

H. Everett and J. C. Powl (1976). 'Adsorption in slit-like and cylindrical micropores in the Henry's law region: A model for the microporosity of carbons.' *Journal of the Chemical Society, Faraday Transactions 1*, **72**, 619.

W. Fang, L. Zhang, and J. Jiang (2010). 'Polymers of intrinsic microporosity for gas permeation: A molecular simulation study.' *Molecular Simulation*, **36**, 992.

W. Fang, L. Zhang, and J. Jiang (2011). 'Gas permeation and separation in functionalized polymers of intrinsic microporosity: A combination of molecular simulations and ab initio calculations.' *Journal of Physical Chemistry C*, **115**, 14123.

A. Fick (1855a). 'On liquid diffusion.' *Philosophical Magazine*, **10**, 30.

A. Fick (1855b). 'Über Diffusion.' *Annalen der Physik*, **94**, 59.

A. Fick (1995). 'On liquid diffusion (Reprint of the original 1855 article).' *Journal of Membrane Science*, **100**, 33.

E. Forte, A. J. Haslam, G. Jackson, and E. A. Müller (2014). 'Effective coarse-grained solid-fluid potentials and their application to model adsorption of fluids on heterogeneous surfaces.' *Physical Chemistry Chemical Physics*, **16**, 19165.

D. Frenkel and B. Smit (2001). *Understanding Molecular Simulation*. Academic Press, London, UK.

H. Frentrup, C. Avendaño, M. Horsch, A. Salih, and E. A. Müller (2012). 'Transport diffusivities of fluids in nanopores by non-equilibrium Molecular Dynamics simulation.' *Molecular Simulation*, **38**, 540.

S.-I. Furukawa, K. Hayashi, and T. Nitta (1997). 'Effects of surface heterogeneity on gas permeation through slit-like carbon membranes by non-equilibrium Molecular Dynamics simulations.' *Journal of Chemical Engineering of Japan*, **30**, 1107.

G. Galliéro, C. Boned, and A. Baylaucq (2005). 'Molecular Dynamics study of the Lennard-Jones fluid viscosity: Application to real fluids.' *Industrial & Engineering Chemistry Research*, **44**, 6963.

L. D. Gelb and K. E. Gubbins (1998). 'Characterization of porous glasses: Simulation models, adsorption isotherms, and the Brunauer-Emmett-Teller analysis method.' *Langmuir*, **14**, 2097.

L. D. Gelb and K. E. Gubbins (1999). 'Pore size distributions in porous glasses : A computer simulation study.' *Langmuir*, **15**, 305.

R. B. Getman, Y.-S. Bae, C. E. Wilmer, and R. Q. Snurr (2012). 'Review and analysis of molecular simulations of methane, hydrogen, and acetylene storage in metal-organic frameworks.' *Chemical Reviews*, **112**, 703.

J. W. Gibbs (1875). 'On the equilibrium of heterogenous substances.' *Transactions of the Connecticut Academy of Arts and Sciences*, **3**, 108.

T. Graham (1829). 'A short account of the experimental researches on the diffusion of gases through each other, and their separation by mechanical means.' *The Quarterly Journal of Science, Literature and Art*, **27**, 74.

C. G. Gray and K. E. Gubbins (1984). *Theory of Molecular Fluids, Vol. 1: Fundamentals*. Oxford University Press, Oxford, UK.

M. Groombridge, M. Schneemilch, and N. Quirke (2011). 'Slip boundaries in nanopores.' *Molecular Simulation*, **37**, 1023.

K. E. Gubbins, Y.-C. Liu, J. D. Moore, and J. C. Palmer (2011). 'The role of molecular modeling in confined systems: Impact and prospects.' *Physical Chemistry Chemical Physics*, **13**, 58.

K. E. Gubbins and J. D. Moore (2010). 'Molecular modeling of matter: Impact and prospects in engineering.' *Industrial & Engineering Chemistry Research*, **49**, 3026.

K. E. Hart, L. J. Abbott, and C. M. Colina (2013a). 'Analysis of force fields and BET theory for polymers of intrinsic microporosity.' *Molecular Simulation*, **39**, 397.

K. E. Hart, L. J. Abbott, N. B. McKeown, and C. M. Colina (2013b). 'Toward effective CO2/CH4 separations by sulfur-containing PIMs via predictive molecular simulations.' *Macromolecules*, **46**, 5371.

K. E. Hart and C. M. Colina (2014). 'Estimating gas permeability and permselectivity of microporous polymers.' *Journal of Membrane Science*, **468**, 259.

K. E. Hart, J. M. Springmeier, N. B. McKeown, and C. M. Colina (2013c). 'Simulated swelling during low-temperature N2 adsorption in polymers of intrinsic microporosity.' *Physical Chemistry Chemical Physics*, **15**, 20161.

G. S. S. Heffelfinger and F. van Swol (1994). 'Diffusion in Lennard-Jones fluids using dual control volume grand canonical molecular dynamics simulation (DCV-GCMD).' *Journal of Chemical Physics*, **100**, 7548.

M. Heuchel, D. Fritsch, P. M. Budd, N. B. McKeown, and D. Hofmann (2008). 'Atomistic packing model and free volume distribution of a polymer with intrinsic microporosity (PIM-1).' *Journal of Membrane Science*, **318**, 84.

J. O. Hirschfelder, C. F. Curtiss, and R. B. Bird (1954). *Molecular Theory of Gases and Liquids*. John Wiley & Sons Inc., New York, USA.

D. Hofmann, L. Fritz, J. Ulbrich, C. Schepers, and M. Böhning (2000). 'Detailed-Atomistic molecular modeling of small molecule diffusion and solution processes in polymeric membrane materials.' *Macromolecular Theory and Simulations*, **9**, 293.

J. K. Holt, H. G. Park, Y. Wang, M. Stadermann, A. B. Artyukhin, C. P. Grigoropoulos, A. Noy, and O. Bakajin (2006). 'Fast mass transport through sub-2-nanometer carbon nanotubes.' *Science*, **312**, 1034.

C. Huang, P. Y. K. Choi, and L. W. Kostiuk (2011). 'A method for creating a non-equilibrium NT(P1-P2) ensemble in Molecular Dynamics simulation.' *Physical Chemistry Chemical Physics*, **13**, 20750.

G. Hummer, J. C. Rasaiah, and J. P. Noworyta (2001). 'Water conduction through the hydrophobic channel of a carbon nanotube.' *Nature*, **414**, 188.

J. N. Israelachvili (2011). *Intermolecular and Surface Forces*. Elsevier B.V., Amsterdam, Netherlands, 3rd edition.

A. F. Izmailov and A. S. Myerson (2005). 'Introduction to molecular modeling.' In A. S. Myerson (Editor), *Molecular Modeling Applications in Crystallization*. Cambridge University Press, Cambridge, UK.

L. Jasperson, G. M. Wilson, and L. C. Wilson (1996). 'Vapor pressures, critical properties, and high pressure pVT measurements on phosgene.' In *AIChE Spring Proceedings*. New Orleans, USA.

O. G. Jepps, S. K. Bhatia, and D. Searles (2003). 'Wall mediated transport in confined spaces: Exact theory for low density.' *Physical Review Letters*, **91**, 126102.

O. G. Jepps, S. K. Bhatia, and D. J. Searles (2004). 'Modeling molecular transport in slit pores.' *Journal of Chemical Physics*, **120**, 5396.

J. K. Johnson, J. Zollweg, and K. E. Gubbins (1993). 'The Lennard-Jones equation of state revisited.' *Molecular Physics*, **78**, 591.

J. E. Jones (1924). 'On the determination of molecular fields. I. From the variation of the viscosity of a gas with temperature.' *Proceedings of the Royal Society A: Mathematical, Physical and Engineering Sciences*, **106**, 441.

W. L. Jorgensen, D. S. Maxwell, and J. Tirado-Rives (1996). 'Development and testing of the OPLS all-atom force field on conformational energetics and properties of organic liquids.' *Journal of American Chemical Society*, **7863**, 11225.

S. Karan, S. Samitsu, X. Peng, K. Kurashima, and I. Ichinose (2012). 'Ultrafast viscous permeation of organic solvents through diamond-like carbon nanosheets.' *Science*, **335**, 444.

J. Kärger, D. M. Ruthven, and D. N. Theodorou (2012). *Diffusion in Nanoporous Materials*. Wiley-VCH, Weinheim, Germany.

D. J. Keffer, C. Y. Gao, and B. J. Edwards (2005). 'On the relationship between Fickian diffusivities at the continuum and molecular levels.' *Journal of Physical Chemistry B*, **109**, 5279.

P. J. Kerkhof, M. A. Geboers, and K. J. Ptasinski (2001). 'On the isothermal binary mass transport in a single pore.' *Chemical Engineering Journal*, **83**, 107.

S. Keskin and D. S. Sholl (2009). 'Assessment of a metal-organic framework membrane for gas separations using atomically detailed calculations : CO2, CH4, N2, H2 mixtures in MOF-5.' *Industrial & Engineering Chemistry Research*, **48**, 914.

S. Kjelstrup, D. Bedeaux, E. Johannessen, and J. Gross (2010). *Non-equilibrium Thermodynamics for Engineers*. World Scientific Publishing Company, Singapore.

M. Knudsen (1909). 'Die Gesetze der Molekularstömung und der inneren Reibungsströmung der Gase durch Röhren.' *Annalen der Physik*, **333**, 75.

W. J. Koros and R. Mahajan (2000). 'Pushing the limits on possibilities for large scale gas separation: Which strategies?' *Journal of Membrane Science*, **175**, 181.

R. Krishna (2009). 'Describing the diffusion of guest molecules inside porous structures.' *Journal of Physical Chemistry C*, **113**, 19756.

R. Krishna and J. A. Wesselingh (1997). 'The Maxwell-Stefan approach to mass transfer.' *Chemical Engineering Science*, **52**, 861.

R. Kubo (1957). 'Statistical-Mechanical theory of irreversible processes. I. General theory and simple applications to magnetic and conduction problems.' *Journal of the Physical Society of Japan*, **12**, 570.

C. Kunert and J. Harting (2007). 'Roughness induced boundary slip in microchannel flows.' *Physical Review Letters*, **99**, 3.

T. Lafitte, A. Apostolakou, C. Avendaño, A. Galindo, C. S. Adjiman, E. A. Müller, and G. Jackson (2013). 'Accurate statistical associating fluid theory for chain molecules formed from Mie segments.' *Journal of Chemical Physics*, **139**, 154504.

G. S. Larsen, P. Lin, K. E. Hart, and C. M. Colina (2011). 'Molecular simulations of PIM-1-like polymers of intrinsic microporosity.' *Macromolecules*, **44**, 6944.

J.-S. Lee, C. D. Wick, J. M. Stubbs, and J. I. Siepmann (2005). 'Simulating the vapour-liquid equilibria of large cyclic alkanes.' *Molecular Physics*, **103**, 99.

J. E. Lennard-Jones (1931). 'Cohesion.' *Proceedings of the Physical Society*, **43**, 461.

P. Li, T. S. Chung, and D. R. Paul (2013). 'Gas sorption and permeation in PIM-1.' *Journal of Membrane Science*, **432**, 50.

P. Li, T. S. Chung, and D. R. Paul (2014). 'Temperature dependence of gas sorption and permeation in PIM-1.' *Journal of Membrane Science*, **450**, 380.

J.-R. Li, R. J. Kuppler, and H.-C. Zhou (2009). 'Selective gas adsorption and separation in metal-organic frameworks.' *Chemical Society Reviews*, **38**, 1477.

Y.-I. Lim, S. K. Bhatia, T. X. Nguyen, and D. Nicholson (2010). 'Prediction of carbon dioxide permeability in carbon slit pores.' *Journal of Membrane Science*, **355**, 186.

X. Liu, S. Schnell, J.-m. Simon, D. Bedeaux, S. Kjelstrup, A. Bardow, and T. J. H. Vlugt (2011). 'Fick diffusion coefficients of liquid mixtures directly obtained from equilibrium Molecular Dynamics.' *Journal of Physical Chemistry B*, p. 110928161803009.

E. J. Maginn, A. T. Bell, and D. N. Theodorou (1993). 'Transport diffusivity of methane in silicalite from equilibrium and non-equilibrium simulations.' *Journal of Physical Chemistry*, **97**, 4173.

E. J. Maginn and J. R. Elliott (2010). 'Historical perspective and current outlook for Molecular Dynamics as a chemical engineering tool.' *Industrial & Engineering Chemistry Research*, **49**, 3059.

M. Majumder, N. Chopra, R. Andrews, and B. J. Hinds (2005). 'Nanoscale hydrodynamics: Enhanced flow in carbon nanotubes.' *Nature*, **438**, 44.

H. Marsh and F. Rodriguez-Reinoso (2006). *Activated Carbon*. Elsevier B.V., Amsterdam, Netherlands.

M. G. Martin and J. I. Siepmann (1997). 'Predicting multicomponent phase equilibria and free energies of transfer for alkanes by molecular simulation.' *Journal of American Chemical Society*, **119**, 8921.

M. G. Martin and J. I. Siepmann (1998). 'Transferable potentials for phase equilibria. 1. United-Atom description of n-alkanes.' *Journal of Physical Chemistry B*, **102**, 2569.

J. C. Maxwell (1867). 'On the dynamical theory of gases.' *Proceedings of the Royal Society*, **157**, 49.

A. D. McNaught and A. Wilkinson (1997). *IUPAC Compendium of Chemical Terminology (The "Gold Book")*. Blackwell Scientific Publications, Oxford, UK, 2nd edition.

D. A. McQuarrie (2000). *Statistical Mechanics*. University Science Books, Sausalito, USA, 2nd edition.

M. Melillo, F. Zhu, M. A. Snyder, and J. Mittal (2011). 'Water transport through nanotubes with varying interaction strength between tube wall and water.' *Journal of Physical Chemistry Letters*, **2**, 2978.

N. Metropolis, A. W. Rosenbluth, M. N. Rosenbluth, A. H. Teller, and E. Teller (1953). 'Equation of state calculations by fast computing machines.' *Journal of Chemical Physics*, **21**, 1087.

R. Mueller, R. Kanungo, M. Kiyono-Shimobe, W. J. Koros, and S. Vasenkov (2012). 'Diffusion of methane and carbon dioxide in carbon molecular sieve membranes by multinuclear pulsed field gradient NMR.' *Langmuir*, **28**, 10296.

I. Müller (2007). *A History of Thermodynamics*. Springer, Berlin, Germany.

F. Müller-Plathe (1994). 'Permeation of polymers - A computational approach.' *Acta Polymerica*, **45**, 259.

F. Müller-Plathe, S. C. Rogers, and W. F. van Gunsteren (1992). 'Computational evidence for anomalous diffusion of small molecules in amorphous polymers.' *Chemical Physics Letters*, **199**, 237.

R. R. Nair, H. A. Wu, P. N. Jayaram, I. V. Grigorieva, and A. K. Geim (2012). 'Unimpeded permeation of water through helium-leak-tight graphene-based membranes.' *Science*, **335**, 442.

S. Neyertz and D. Brown (2009). 'Oxygen sorption in glassy polymers studied at the molecular level.' *Macromolecules*, **42**, 8521.

S. Neyertz and D. Brown (2013). 'Molecular Dynamics study of carbon dioxide sorption and plasticization at the interface of a glassy polymer membrane.' *Macromolecules*, **46**, 2433.

D. Nicholson (1997). 'The transport of adsorbate mixtures in porous materials: Basic equations for pores with simple geometry.' *Journal of Membrane Science*, **129**, 209.

D. Nicholson (1998). 'Simulation studies of methane transport in model graphite micropores.' *Carbon*, **36**, 1511.

D. Nicholson (1999). 'A Simulation study of energetic and structural heterogeneity in slit-shaped pores.' *Langmuir*, **15**, 2508.

D. Nicholson and N. G. Parsonage (1982). *Computer simulation and the statistical mechanics of adsorption*. Academic Press, London, UK.

J. A. L. Nollet (1748). 'Recherches sur les causes du bouillonnement des liquides (Investigations on the causes for the ebullition of liquids).'

J. A. L. Nollet (1995). 'Investigations on the causes for the ebullition of liquids (Reprint of the original 1748 article).' *Journal of Membrane Science*, **100**, 1.

A. Z. Panagiotopoulos (1987). 'Direct determination of phase coexistence properties of fluids by Monte Carlo simulation in a new ensemble.' *Molecular Physics*, **61**, 813.

S. Plimpton (1995). 'Fast parallel algorithms for short-range Molecular Dynamics.' *Journal of Computational Physics*, **117**, 1.

J. J. Potoff and J. I. Siepmann (2001). 'Vapor-Liquid equilibria of mixtures containing alkanes, carbon dioxide, and nitrogen.' *AIChE Journal*, **47**, 1676.

R. Radhakrishnan, K. E. Gubbins, and M. Sliwinska-Bartkowiak (2002). 'Global phase diagrams for freezing in porous media.' *Journal of Chemical Physics*, **116**, 1147.

N. Rai and J. I. Siepmann (2007). 'Transferable potentials for phase equilibria. 9. Explicit hydrogen description of benzene and five-membered and six-membered heterocyclic aromatic compounds.' *Journal of Physical Chemistry B*, **111**, 10790.

D. C. Rapaport (2004). *The Art of Molecular Dynamics Simulation*. Cambridge University Press, Cambridge, UK, 2nd edition.

J. C. Rasaiah, S. Garde, and G. Hummer (2008). 'Water in nonpolar confinement: from nanotubes to proteins and beyond.' *Annual Review of Physical Chemistry*, **59**, 713.

R. C. Reid, J. M. Prausnitz, and B. E. Poling (1987). *The Properties of Gases and Liquids*. McGraw Hill Book Co., New York.

L. M. Robeson, Z. P. Smith, B. D. Freeman, and D. R. Paul (2014). 'Contributions of diffusion and solubility selectivity to the upper bound analysis for glassy gas separation membranes.' *Journal of Membrane Science*, **453**, 71.

S. W. Rutherford and D. D. Do (1997). 'Review of time lag permeation technique as a method for characterisation of porous media and membranes.' *Adsorption*, **3**, 283.

R. J. Sadus and J. M. Prausnitz (1996). 'Three-body interactions in fluids from molecular simulation: Vapor-liquid phase coexistence of argon.' *J. Chem. Phys.*, **104**, 4784.

A. Salih (2010). *Molecular simulation of the adsorption and transport properties of carbon dioxide, methane, water and their mixtures in coal-like structures*. Doctoral thesis, Imperial College London, London, UK.

L. Sarkisov and A. Harrison (2011). 'Computational structure characterisation tools in application to ordered and disordered porous materials.' *Molecular Simulation*, **37**, 1248.

P. Schneider (1978). 'Multicomponent isothermal diffusion and forced flow of gases in capillaries.' *Chemical Engineering Science*, **33**, 1311.

F. Schuth, K. S. W. Sing, and J. Weitkamp (2002). *Handbook of Porous Solids*. Wiley-VCH, Berlin, Germany.

D. S. Sholl (2006). 'Understanding macroscopic diffusion of adsorbed molecules in crystalline nanoporous materials via atomistic simulations.' *Accounts of Chemical Research*, **39**, 403.

P. Silva, S. Han, and A. Livingston (2005). 'Solvent transport in organic solvent nanofiltration membranes.' *Journal of Membrane Science*, **262**, 49.

C. M. Silva and H. Liu (2008). 'Modelling of transport properties of hard sphere fluids and related systems, and its applications.' In A. Mulero (Editor), *Theory and Simulation of Hard-Sphere Fluid and Related Systems*. Springer, Berlin, Germany.

A. I. Skoulidas and D. S. Sholl (2002). 'Transport diffusivities of CH4, CF4, He, Ne, Ar, Xe, and SF6 in silicalite from atomistic simulations.' *Journal of Physical Chemistry B*, **106**, 5058.

B. Smit and T. L. M. Maesen (2008). 'Molecular simulations of zeolites: Adsorption, diffusion, and shape selectivity.' *Chemical Reviews*, **108**, 4125.

M. Smoluchowski (1906). 'Zur kinetischen Theorie der Brownschen Molekularbewegung und der Suspensionen.' *Annalen der Physik*, **21**, 756.

R. Q. Snurr and J. Kärger (1997). 'Molecular simulations and NMR measurements of binary diffusion in zeolites.' *Journal of Physical Chemistry B*, **101**, 6469.

V. P. Sokhan, D. Nicholson, and N. Quirke (2001). 'Fluid flow in nanopores: An examination of hydrodynamic boundary conditions.' *Journal of Chemical Physics*, **115**, 3878.

X. Song and J. Chen (2008). 'A comparative study on poiseuille flow of simple fluids through cylindrical and slit-like nanochannels.' *International Journal of Heat and Mass Transfer*, **51**, 1770.

S. Sourirajan and J. P. Agrawal (1969). 'Reverse osmosis.' *Industrial & Engineering Chemistry*, **61**, 62.

W. A. Steele (1978). 'The interaction of rare gas atoms with graphitized carbon black.' *Journal of Physical Chemistry*, **82**, 817.

F. H. Stillinger and A. Rahman (1974). 'Improved simulation of liquid water by Molecular Dynamics.' *Journal of Chemical Physics*, **60**, 1545.

A. J. Stone (2013). *The Theory of Intermolecular Forces*. Oxford University Press, Oxford, UK.

H. Sun, S. J. Mumby, J. R. Maple, and A. T. Hagler (1994). 'An ab initio CFF93 all-atom force field for polycarbonates.' *Journal of the American Chemical Society*, **116**, 2978.

R. Taylor and R. Krishna (1993). *Multicomponent Mass Transfer*. John Wiley & Sons Inc., New York, USA.

D. N. Theodorou (2010). 'Progress and outlook in Monte Carlo simulations.' *Industrial & Engineering Chemistry Research*, **49**, 3047.

P. A. Thompson and S. M. Troian (1997). 'A general boundary condition for liquid flow at solid surfaces.' *Nature*, **389**, 360.

W. Thomson (1879). 'The sorting demon of Maxwell.' *Proceedings of the Royal Institution*, **9**, 113.

W. Thomson (1901). 'Nineteenth-century clouds over the dynamical theory of heat and light.' *Philosophical Magazine*, **2**, 1.

J. Tóth (1962). 'Gas-(Dampf-)Adsorption an festen Oberflächen inhomogener Aktivität.' *Acta Chimica Academiae Scientarium Hungaricae*, **30**, 415.

K. P. Travis and K. E. Gubbins (2000a). 'Combined diffusive and viscous transport of methane in a carbon slit pore.' *Molecular Simulation*, **25**, 209.

K. P. Travis and K. E. Gubbins (2000b). 'Poiseuille flow of Lennard-Jones fluids in narrow slit pores.' *Journal of Chemical Physics*, **112**, 1984.

K. P. Travis and K. E. Gubbins (2001). 'Computer simulation of isothermal mass transport in graphite slit pores.' *Molecular Simulation*, **27**, 405.

I. M. J. J. Van De Ven-Lucassen, T. J. H. Vlugt, A. J. J. Van der Zanden, and P. J. A. M. Kerkhof (1998). 'Using Molecular Dynamics to obtain Maxwell-Stefan diffusion coefficients in liquid systems.' *Molecular Physics*, **94**, 495.

J. D. van der Waals (1873). *Over de Continuiteit van den Gas- en Vloeistoftoestand (On the continuity of the gas and liquid state)*. Doctoral thesis, Universiteit Leiden, Netherlands.

L. Verlet (1967). 'Computer "experiments" on classical fluids. I. Thermodynamical properties of Lennard-Jones molecules.' *Physical Review*, **159**, 98.

A. M. Vieira-Linhares and N. A. Seaton (2003). 'Non-equilibrium molecular dynamics simulation of gas separation in a microporous carbon membrane.' *Chemical Engineering Science*, **58**, 4129.

O. Vopička, K. Friess, V. Hynek, P. Sysel, M. Zgažar, M. Šípek, K. Pilnáček, M. Lanč, J. C. Jansen, C. R. Mason, and P. M. Budd (2013). 'Equilibrium and transient sorption of vapours and gases in the polymer of intrinsic microporosity PIM-1.' *Journal of Membrane Science*, **434**, 148.

J. Vrabec, G. K. Kedia, G. Fuchs, and H. Hasse (2006). 'Comprehensive study of the vapour-liquid coexistence of the truncated and shifted Lennard-Jones fluid including planar and spherical interface properties.' *Molecular Physics*, **104**, 1509.

Y. Wang and M. D. LeVan (2008). 'Mixture diffusion in nanoporous adsorbents: Equivalence of Fickian and Maxwell-Stefan approaches.' *Journal of Physical Chemistry B*, **112**, 8600.

J. Wang, R. M. Wolf, J. W. Caldwell, P. A. Kollman, and D. A. Case (2004). 'Development and testing of a general Amber force field.' *Journal of Computational Chemistry*, **25**, 1157.

J. D. Weeks (1971). 'Role of repulsive forces in determining the equilibrium structure of simple liquids.' *Journal of Chemical Physics*, **54**, 5237.

J. R. Whitman, G. L. Aranovich, and M. D. Donohue (2011). 'Thermodynamic driving force for diffusion: Comparison between theory and simulation.' *Journal of Chemical Physics*, **134**, 94303.

C. D. Wick, J. M. Stubbs, N. Rai, and J. I. Siepmann (2005). 'Transferable potentials for phase equilibria. 7. Primary, secondary, and tertiary amines, nitroalkanes and nitrobenzene, nitriles, amides, pyridine, and pyrimidine.' *Journal of Physical Chemistry B*, **109**, 18974.

J. Wijmans and R. Baker (1995). 'The solution-diffusion model: a review.' *Journal of Membrane Science*, **107**, 1.

C. E. Wilmer, M. Leaf, C. Y. Lee, O. K. Farha, B. G. Hauser, J. T. Hupp, and R. Q. Snurr (2012). 'Large-scale screening of hypothetical metal-organic frameworks.' *Nature Chemistry*, **4**, 83.

Y. Yampolskii (2012). 'Polymeric gas separation membranes.' *Macromolecules*, **45**, 3298.

R. Zan, Q. M. Ramasse, U. Bangert, and K. S. Novoselov (2012). 'Graphene reknits its holes.' *Nano Letters*, **12**, 3936.

V. M. Zhdanov and V. I. Roldughin (2002). 'Kinetic phenomena in the diffusion of gases in capillaries and porous bodies.' *Colloid Journal*, **64**, 1.

Y.-G. Zheng, H.-F. Ye, Z.-Q. Zhang, and H.-W. Zhang (2012). 'Water diffusion inside carbon nanotubes: Mutual effects of surface and confinement.' *Physical Chemistry Chemical Physics*, **14**, 964.

F. Zhu, E. Tajkhorshid, and K. Schulten (2004). 'Theory and simulation of water permeation in Aquaporin-1.' *Biophysical Journal*, **86**, 50.

APPENDIX

A

APPENDIX

A.1 Translation of epigraphs

Chapter 2 - Fick

Adolf Fick in "Über Diffusion, Annalen der Physik" (1855)

"Perhaps the reason for such scarce treatment is the great difficulty in conducting exact quantitative experiments in this field. And, in deed, it is so great that, despite my ongoing effort, I did not succeed in ultimately consolidating the conflict between the theories."

Chapter 3 - Laplace

Pierre Simon Laplace in "A Philosophical Essay on Probabilities" (1814)

"We may regard the present state of the universe as the effect of its past and the cause of its future. An intellect which at a certain moment would know all forces that set nature in motion, and all positions of all items of which nature is composed, if this intellect were also vast enough to submit these data to analysis, it would embrace in a single formula the movements of the greatest bodies of the universe and those of the tiniest atom; for such an intellect nothing would be uncertain and the future just like the past would be present before its eyes."

Chapter 5

Pablo Ruiz Picasso (1881-1973)

"Anything you can imagine is real"

A.2 Additional data on the slit pore system

Thermodynamic observables of the bulk LJ fluid

In addition to the data presented in Chapter 4, simulation results in comparison to equation of state data for the bulk LJ fluid is shown in Fig. A.1 ($P - \rho$-relationship), Fig. A.2 ($\mu - \rho$-relationship), and Fig. A.3 ($\mu - P$-relationship). The data is shown to provide clarity and additional information about the dependence of thermodynamic variables.

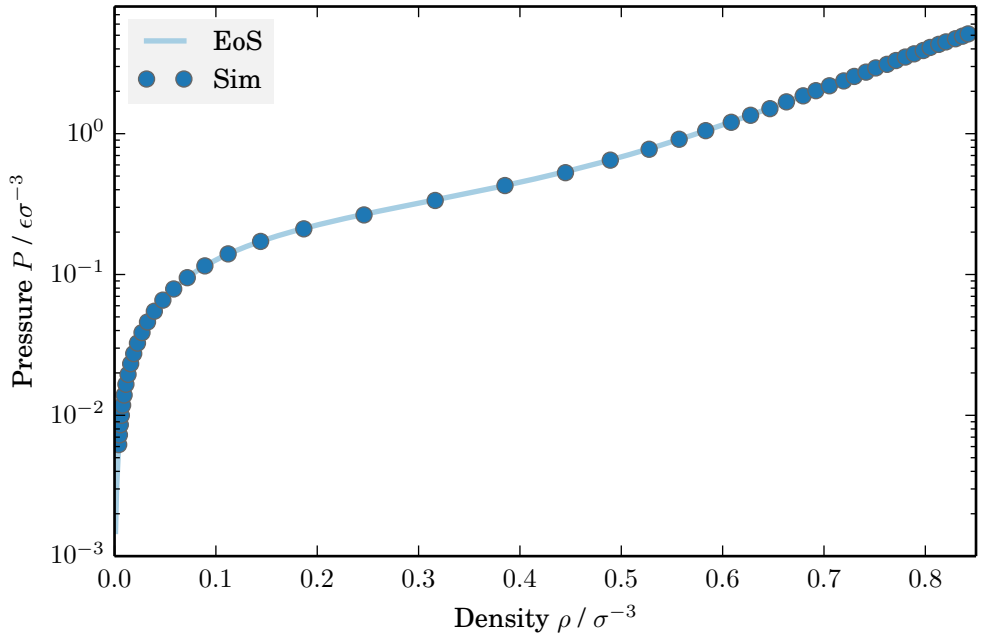

Figure A.1: Pressure isotherm at $T = 1.5$ as a function of density for the bulk Lennard-Jones fluid. The error bars are smaller than the symbols.

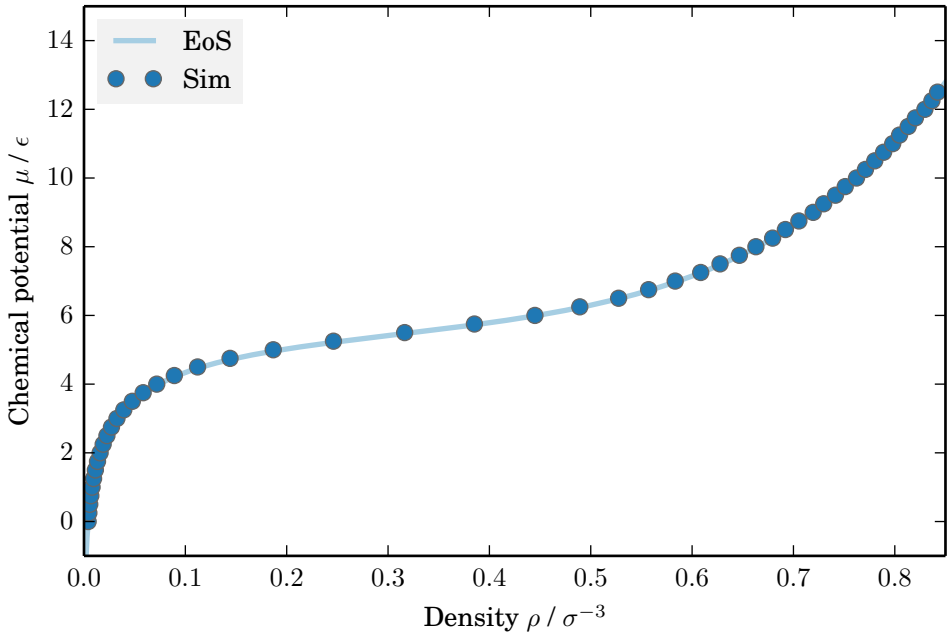

Figure A.2: Chemical potential as a function of density for the bulk Lennard-Jones fluid. The error bars are smaller than the symbols.

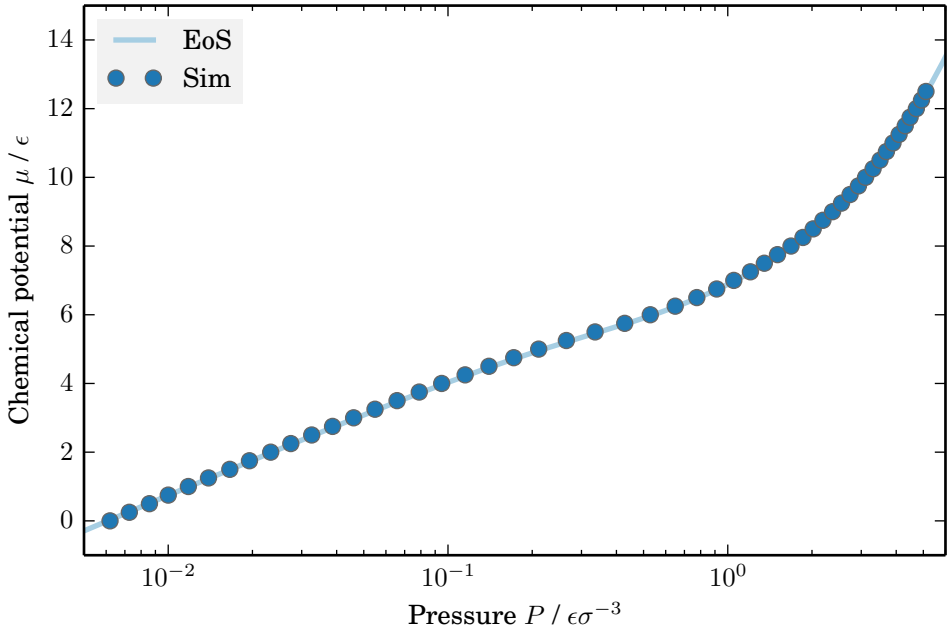

Figure A.3: Chemical potential as a function of pressure for the bulk Lennard-Jones fluid. The error bars are smaller than the symbols.

Thermodynamic factors of the confined LJ fluid

The results show in Fig. A.4 and A.5 are the same as the thermodynamic factor data for the confined fluid given in Chapter 4, the pressure range is extended though and shows considerable deviation at high pressures due to the problem highlighted in connection to molecular simulation of dense fluids.

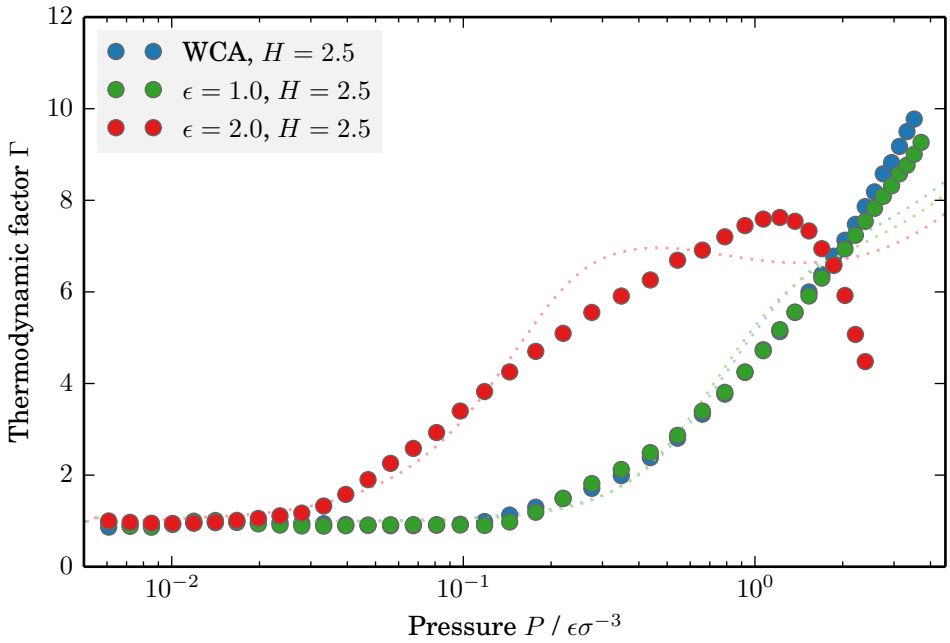

Figure A.4: Thermodynamic factor of the confined Lennard-Jones fluid, inside the narrow pore with $H = 2.5$. The entire simulated range is shown here, but results at higher pressure (dense fluids) are not considered reliable results.

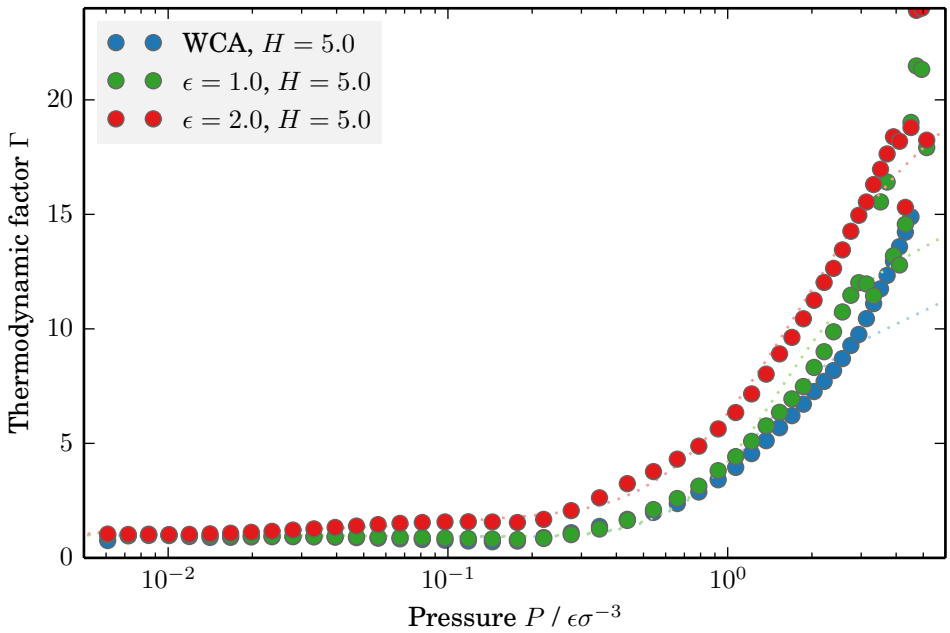

Figure A.5: Thermodynamic factor of the confined Lennard-Jones fluid, inside the wide pore with $H = 5.0$. The entire simulated range is shown here, but results at higher pressure (dense fluids) are not considered reliable results.

Diffusion coefficients from EMD simulations as a function of pore loading

The results for diffusion coefficients are tabulated here and plotted in Fig. A.6 and A.7 as a function of pore loading. The tabulated results are given with six relevant as they were computed, but it is important to note that this does not imply that the results are computed to this accuracy. Given the range of results, they are tabulated for reference and error bars are usually not straight-forward to calculate for transport properties such as the diffusion coefficients.

Step-by-step guide to obtaining transport diffusion coefficients from EMD simulations

In order to reproduce the results for transport diffusivities based on the Darken model given in Fig. 4.19 and 4.20, there are a number of steps which need to be performed:

- The equation of state of the bulk fluid must be obtained either from simulation or literature (if available). This yields the relationship between chemical potential

and pressure ($\rightarrow P(\mu)$).

- The adsorption isotherm of a given slit pore must be obtained by performing Grand Canonical insertions. The μVT results ($N(\mu)$) can be converted into loading curves via the bulk data ($\rightarrow N(P)$).
- At the same time, the μVT data can be used to obtain the thermodynamic factor at the given external bulk pressure ($\partial\mu/\partial\ln\langle N\rangle(P)$).
- Subsequently, EMD simulations at a specified loading must be performed in order to obtain self- and collective diffusion coefficients. It is important that the unit cell is exactly the same as the one used during the Grand Canonical simulations.
- The results for collective diffusivity at a specified loading can be converted into diffusivity as a function of external pressure via the adsorption isotherm ($D_{\mathrm{c}}(N) \rightarrow D_{\mathrm{c}}(P)$).
- According to the Darken model, the collective diffusivity multiplied by the thermodynamic factor yields the transport diffusivity ($D_{\mathrm{t}} = D_{\mathrm{c}}(P) \times \Gamma(P)$).

N	P	Γ	D_s	D_c	$D_\mathrm{eff}^\mathrm{EMD}$
Repulsive wall (WCA)					
30	0.276947	1.47898	2.00355	13.6357	20.167
60	0.63774	3.3694	1.03406	14.2744	48.0962
90	0.999392	5.12762	0.589335	9.47697	48.5943
120	1.47568	6.35043	0.402417	6.73517	42.7712
150	2.1552	7.11901	0.302768	5.55514	39.5471
180	3.2024	7.76432	0.194288	3.88304	30.1492
215	4.91016	8.62267	0.122759	1.82246	15.7144
Wetting wall ($\varepsilon = 1.0$)					
30	0.0517276	0.985202	1.46269	2.9974	2.95305
60	0.104218	1.03441	0.777956	3.16892	3.27795
90	0.164802	1.14044	0.530999	2.74488	3.13037
120	0.284604	1.48442	0.3377	2.14472	3.18367
150	0.582529	3.15536	0.247243	1.35704	4.28195
180	1.15224	5.70343	0.180804	1.10176	6.28381
215	2.2442	6.99434	0.117272	0.914323	6.39508
245	3.43095	7.61549	0.0784741	0.63561	4.84048
Strongly wetting wall ($\varepsilon = 2.0$)					
30	0.00954771	1.03576	0.834009	1.04393	1.08127
60	0.0191797	1.15258	0.535395	1.3089	1.50861
90	0.0302947	1.33142	0.361342	1.16669	1.55335
120	0.0477568	1.71292	0.249646	0.735202	1.25934
150	0.0873454	2.83048	0.206836	0.771132	2.18268
180	0.21037	5.94241	0.130169	0.610926	3.63038
215	0.835889	6.7762	0.0985354	0.57139	3.87186
245	1.73359	6.65663	0.0663508	0.350502	2.33316

Table A.1: Simulation results of EMD simulations for the narrow pore.

N	P	Γ	D_s	D_c	$D_\mathrm{eff}^\mathrm{EMD}$
Repulsive wall (WCA)					
60	0.167727	0.920637	2.26471	34.758	31.9995
120	0.34115	1.08698	1.21251	33.2064	36.0948
180	0.538793	1.69361	0.748863	20.7464	35.1362
245	0.84696	3.1701	0.444246	27.7289	87.9033
305	1.33407	5.67024	0.319592	25.0743	142.177
365	2.13403	8.21547	0.223951	11.8838	97.6307
425	3.41387	9.80329	0.161764	7.40272	72.571
Wetting wall ($\varepsilon = 1.0$)					
60	0.0779872	0.948975	1.65692	5.06337	4.80502
120	0.154017	0.93969	0.835819	5.72151	5.37645
180	0.239561	0.974906	0.60463	5.36373	5.22913
245	0.373954	1.19577	0.3765	5.90721	7.06366
305	0.629414	2.14345	0.290416	4.12935	8.85105
365	1.1412	5.07697	0.227898	4.98006	25.2836
425	2.09104	9.69285	0.145289	2.2173	21.492
490	3.95518	12.8441	0.0913086	1.86669	23.976
Strongly wetting wall ($\varepsilon = 2.0$)					
60	0.020749	1.16156	0.737531	1.751	2.0339
120	0.0509012	1.33791	0.518686	1.17841	1.57661
180	0.100251	1.55759	0.418343	1.42931	2.22628
245	0.177069	1.79395	0.332969	1.51541	2.71856
305	0.304527	2.14319	0.252498	1.90162	4.07555
365	0.624114	3.82687	0.184165	1.69913	6.50236
425	1.37746	8.65643	0.132056	1.72962	14.9724
490	3.08437	15.0863	0.0798054	1.01451	15.3052

Table A.2: Simulation results of EMD simulations for the wide pore.

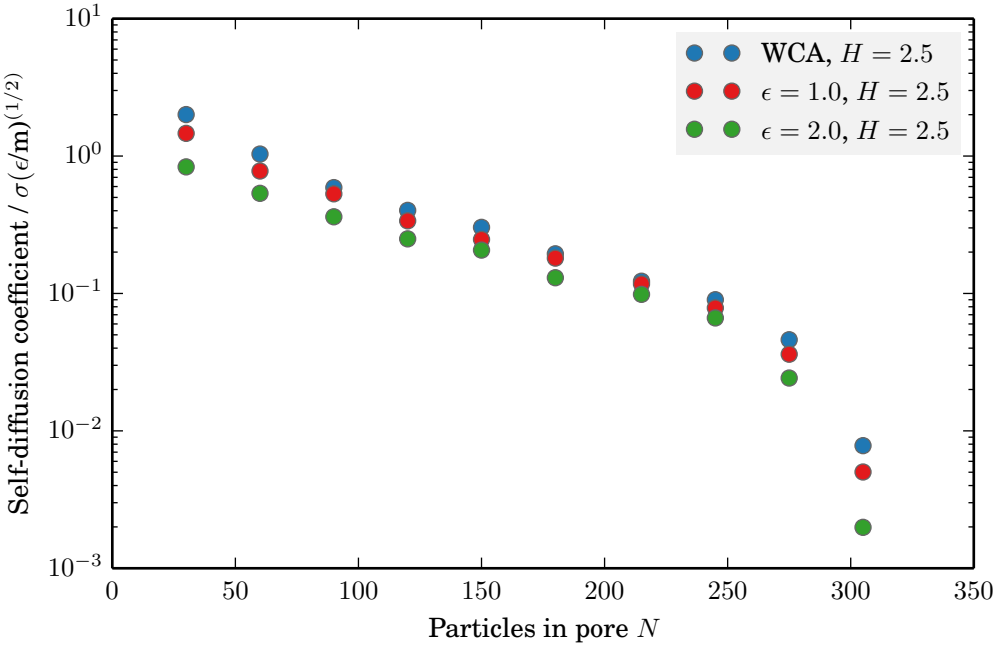

Figure A.6: Self-diffusion coefficients of the confined Lennard-Jones fluid, inside the narrow pore with $H = 2.5$.

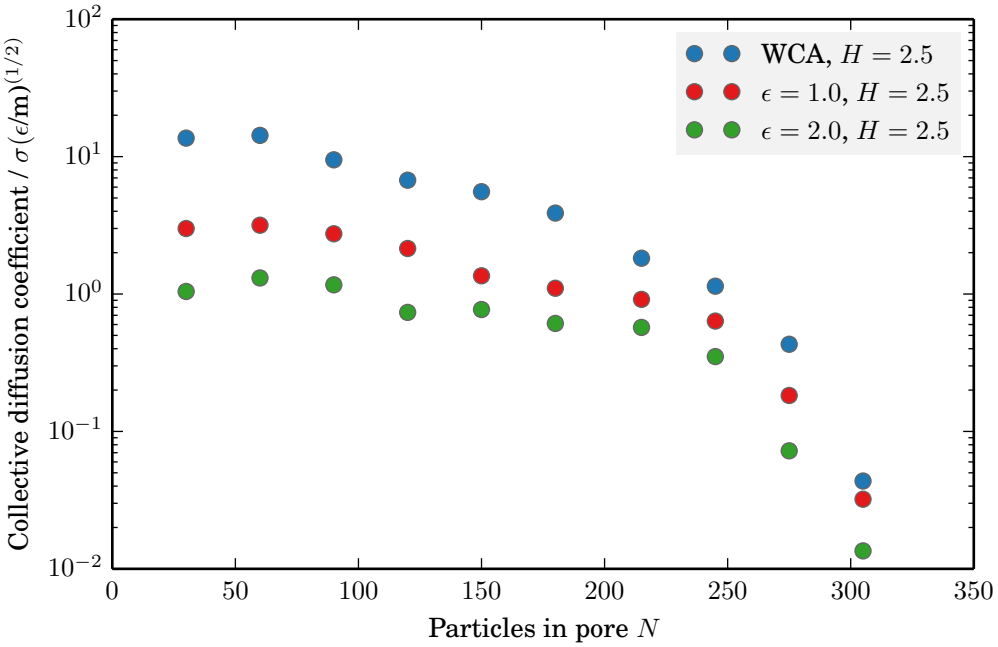

Figure A.7: Collective diffusion coefficients of the confined Lennard-Jones fluid, inside the narrow pore with $H = 2.5$.

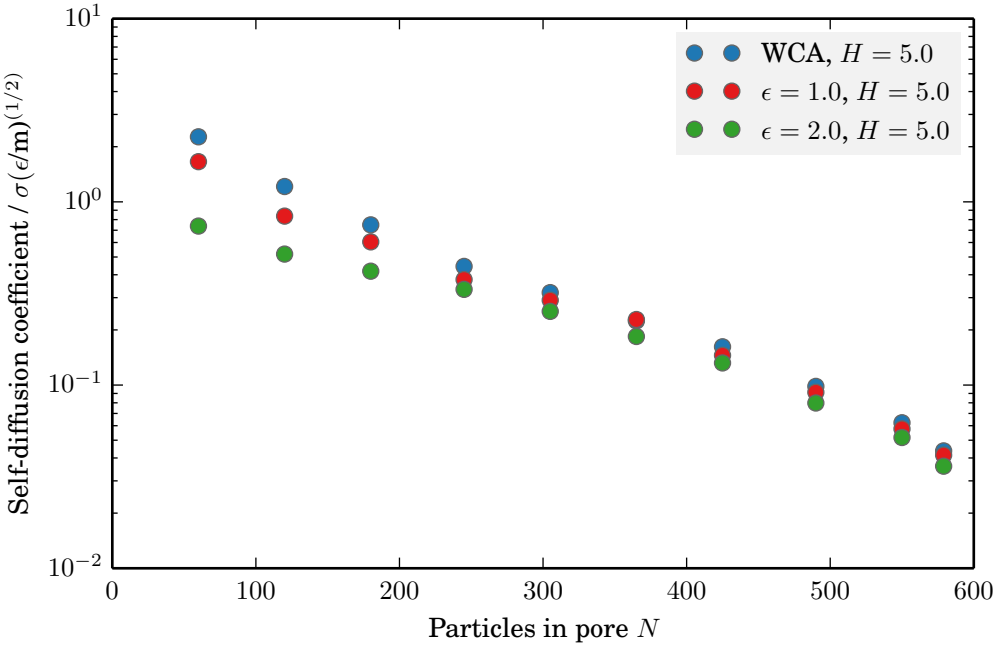

Figure A.8: Self-diffusion coefficients of the confined Lennard-Jones fluid, inside the wide pore with $H = 5.0$.

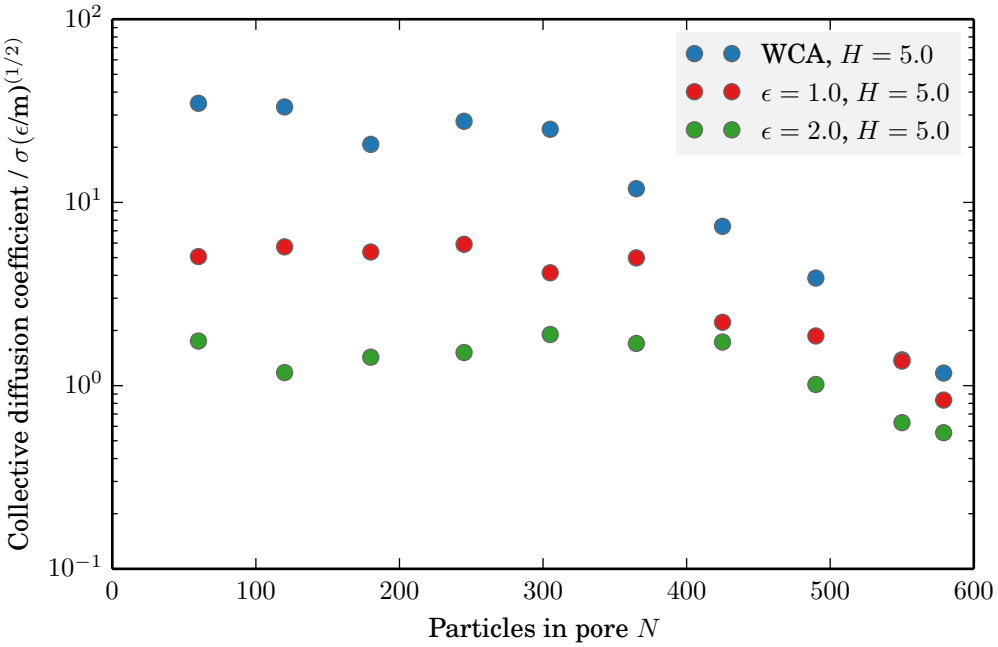

Figure A.9: Collective diffusion coefficients of the confined Lennard-Jones fluid, inside the wide pore with $H = 5.0$.

Effective diffusion coefficients from NEMD simulations as a function of density

Simulation results for boundary-driven NEMD simulations are tabulated in Table A.5 and shown as a function of pore loading in Fig. A.11. The given densities $\bar{\rho}$ were obtained from the bulk section on either side of the pore at equilibrium and bulk pressures were determined from the equation of state data.

Step-by-step guide to obtaining transport diffusion coefficients from NEMD simulations

- As in the case of diffusivities from EMD, it is necessary to have access to thermodynamic data for the bulk fluid (see above).
- Subsequently an inhomogeneous slit pore system is set up, that is the slit pore is surrounded by to sufficiently large bulk compartments on either side (they are usually at least as big as the pore itself). The system must be populated with a specified number of atoms, so that an equilibration in the NVT ensemble can be performed.
- From the density gradients along the pore axis, the equilibrium bulk density of the fluid can be calculated $\bar{\rho}$. This bulk density can be converted into an external bulk pressure via the equation of state data obtained previously $\rightarrow P(\bar{\rho})$.
- The system is then perturbed with a range of external forces acting on the boundary. They yield effective diffusion coefficients as a function of external force ($D_{\text{eff}}(f_{\text{ext}})$).
- Taking the external force to the limit of zero yields the transport diffusion coefficient ($D_{\text{eff}}|_{f_{ext}\rightarrow 0}$) at the given loading (as outlines in section 3.3 and depicted in Fig. 3.8), which has already been connected to the appropriate external bulk pressure previously.

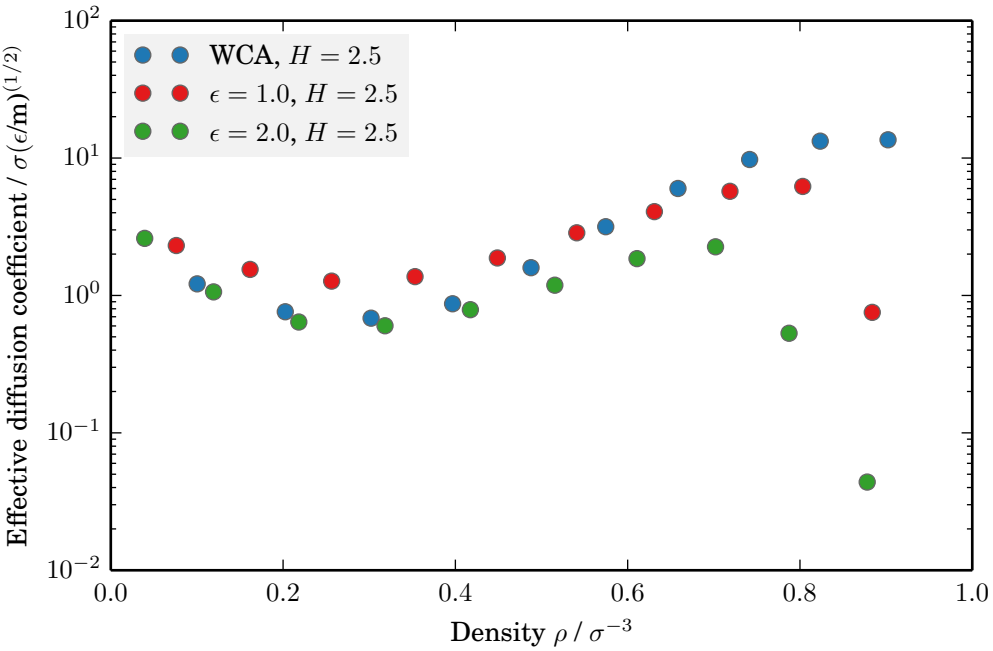

Figure A.10: Effective diffusion coefficients of the confined Lennard-Jones fluid from NEMD simulations as a function of density, inside the narrow pore with $H = 2.5$.

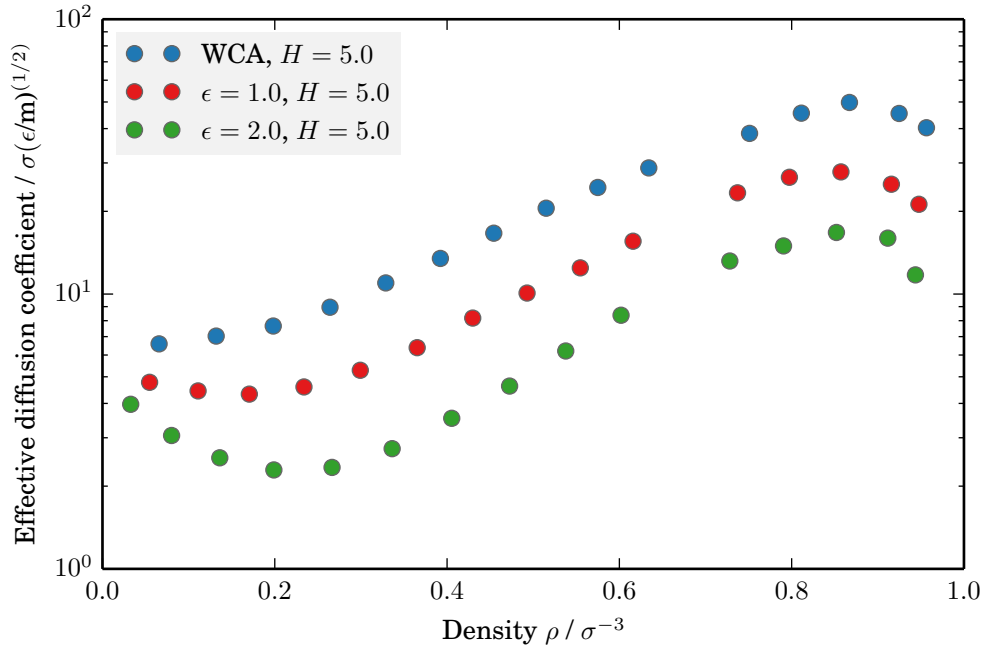

Figure A.11: Effective diffusion coefficients of the confined Lennard-Jones fluid from NEMD simulations as a function of density, inside the wide pore with $H = 5.0$.

$\bar{\rho}$	$P(\bar{\rho})$	$D_{\text{eff}}^{\text{NEMD}}$
Repulsive wall (WCA)		
0.100264	0.127147	1.21429
0.202557	0.227098	0.76098
0.302153	0.323416	0.683341
0.396757	0.446573	0.869903
0.487813	0.646689	1.59252
0.574531	1.00049	3.16438
0.65839	1.63326	6.00491
0.741566	2.74623	9.75976
0.823522	4.58307	13.274
0.902228	7.34551	13.5766
Wetting wall ($\varepsilon = 1.0$)		
0.0760373	0.100102	2.30858
0.161713	0.188988	1.54707
0.256365	0.277327	1.27151
0.353169	0.383236	1.37094
0.448747	0.546118	1.87427
0.540903	0.836446	2.85735
0.631015	1.3841	4.07432
0.718736	2.37818	5.72764
0.803206	4.04224	6.21424
0.883931	6.59835	0.753354
Strongly wetting wall ($\varepsilon = 2.0$)		
0.0393695	0.0550859	2.60272
0.119298	0.147183	1.06157
0.218243	0.241574	0.640715
0.318306	0.341122	0.601739
0.417411	0.482345	0.787748
0.51544	0.736387	1.18756
0.610824	1.22881	1.85337
0.701982	2.14054	2.25947
0.787324	3.66136	0.530742
0.878037	6.37213	0.0438451

Table A.3: Simulation results of boundary-driven NEMD simulations for the narrow pore.

$\bar{\rho}$	$P(\bar{\rho})$	$D_{\mathrm{eff}}^{\mathrm{NEMD}}$
Repulsive wall (WCA)		
0.0656994	0.0879489	6.58763
0.131982	0.160043	7.03176
0.198221	0.223095	7.65021
0.264109	0.284801	8.95533
0.328845	0.353232	10.9772
0.392251	0.439323	13.4779
0.454218	0.558645	16.6527
0.515034	0.734933	20.5317
0.574961	1.00285	24.427
0.634147	1.41024	28.7742
0.751112	2.91656	38.4288
0.811227	4.24834	45.5222
0.867087	5.96981	49.7928
0.924725	8.36282	45.4103
0.956471	10.0001	40.2912
Wetting wall ($\varepsilon = 1.0$)		
0.0546871	0.0745538	4.77416
0.110972	0.138536	4.44181
0.170466	0.197268	4.32399
0.233879	0.256086	4.59201
0.299273	0.320355	5.28075
0.365309	0.399485	6.38139
0.429778	0.506004	8.17757
0.492848	0.661751	10.0847
0.554664	0.898757	12.4536
0.615888	1.26568	15.5713
0.737151	2.67082	23.3544
0.797388	3.89861	26.604
0.857194	5.62571	27.8277
0.915761	7.94394	25.099
0.94772	9.52394	21.2168

Table A.4: Simulation results of boundary-driven NEMD simulations for the wide pore.

$\bar{\rho}$	$P(\bar{\rho})$	$D_{\text{eff}}^{\text{NEMD}}$
Strongly wetting wall ($\varepsilon = 2.0$)		
0.0327589	0.0463636	3.9708
0.0802181	0.104907	3.05738
0.136169	0.164212	2.53615
0.198934	0.223754	2.29098
0.266483	0.287114	2.33994
0.336253	0.362045	2.73776
0.405415	0.46104	3.53155
0.472581	0.604239	4.62569
0.537754	0.823046	6.20615
0.601963	1.16742	8.37406
0.728218	2.52456	13.1907
0.790547	3.73582	14.967
0.851976	5.45139	16.7534
0.911578	7.75467	15.977
0.943683	9.31081	11.7426

Table A.5: Simulation results of boundary-driven NEMD simulations for the wide pore (continued).